Analysis of the H-mode density limit in the ASDEX Upgrade tokamak using bolometry

Matthias Bernert

München 2013

Analysis of the H-mode density limit in the ASDEX Upgrade tokamak using bolometry

Dissertation zur Erlangung des akademischen Grades eines
Doktors der Naturwissenschaften (Dr. rer. nat.)
an der Fakultät für Physik der Ludwig-Maximilians-Universität München

durchgeführt am
Max-Planck-Institut für Plasmaphysik, Garching bei München

vorgelegt von
Matthias Bernert
geboren am 22.05.1984 in Sindelfingen

München, den 31.07.2013

Erstgutachter: Prof. Dr. Hartmut Zohm
Zweitgutachter: Prof. Dr. Gregor Morfill
Tag der mündlichen Prüfung: 23. Oktober 2013

Zusammenfassung

Für den Betrieb von zukünftigen Fusionsexperimenten, wie ITER und DEMO, ist das H-Mode-Operationsregime vorgesehen, das sich gegenüber dem L-Mode-Regime durch einen verbesserten Energieeinschluss auszeichnet. Dabei werden hohe Dichten angestrebt um die Fusionsleistung zu maximieren. Bei zu hohen Dichten findet jedoch ein Übergang in das L-Mode-Regime statt. Dieses H-Mode-Dichtelimit (HDL) tritt in der Nähe des Greenwald Limits (GWL) auf, welches eine obere Dichtegrenze für den Betrieb von Tokamaks darstellt.

Im Rahmen dieser Doktorarbeit wurde das H-Mode-Dichtelimit am Tokamak ASDEX Upgrade (AUG) im Betrieb mit einer Wolframwand experimentell untersucht. Verschiedene existierende Erklärungsansätze für das Auftreten des HDL, wie zum Beispiel der Einfluss von Strahlungsverlusten, wurden für die durchgeführten Experimente ausgeschlossen.

Eine systematische Untersuchung zeigt, dass das HDL durch vier verschiedene, reproduzierbare und quasi-stabile Plasmazustände, die mit ansteigender Plasmadichte aufeinander folgen, charakterisiert wird. Die erste Phase ist eine stabile H-Mode, bei der die Dichte bei konstantem Druck ansteigt. Darauf folgt ein degradierendes H-Mode-Regime, bei dem die zentrale Dichte konstant ist und der Energieeinschluss verschlechtert wird. Die dritten Phase ist der Zusammenbruch des H-Mode-Regimes und somit das eigentliche HDL. Dabei wird der erhöhte H-Mode-Temperaturgradient am Rand abgebaut. In dieser Phase bleibt das gesamte Dichteprofil jedoch konstant. Mit der vierten Phase hat das Plasma das L-Mode-Regime erreicht, bei dem die Dichte bei einem konstanten, niedrigen Energieeinschluss wieder ansteigt.

Grenzwerte des radialen elektrischen Feldes und die Leistungsschwelle der H-Mode erklären potentiell den Übergang in die L-Mode, können aber für das Einsetzen des HDL ausgeschlossen werden.

Die vier Phasen werden durch eine Kombination von zwei Effekten erklärt: ein Absinken der Ionisationsrate im eingeschlossenen Plasma und ein zusätzlicher, bei hohen Dichten auftretender Energieverlustkanal. Diverse Beobachtungen deuten darauf hin, dass der Verlustkanal durch einen erhöhten konvektiven Transport am Rand des Plasmas entsteht.

In dieser Arbeit wurden die vier Phasen auch in AUG Plasmen mit Kohlenstoffwand nachgewiesen. Die Unterschiede zwischen den Beobachtungen bei beiden Wandmaterialien werden auf eine Änderung des Energieverlustkanals zurückgeführt. Dieser Verlustkanal wurde bei Kohlenstoff durch das Ablösen des Plasmas von der Wand erklärt. Dieser Effekt konnte für Wolfram jedoch ausgeschlossen werden.

Im Gegensatz zum GWL hängt die Dichte des HDLs im Betrieb mit Wolframwand nur schwach vom Plasmastrom ab. In dieser Arbeit wurde allerdings eine deutliche Abhängigkeit von der Heizleistung nachgewiesen. Die Triangularität des Plasmas hat keine Auswirkung auf die Dichte des HDL, kann aber die Einschlussgüte des Plasmas bei hohen Dichten deutlich erhöhen, da die degradierende Phase später einsetzt.

Es wird gezeigt, dass man das HDL und das GWL mit zentral erhöhten Dichteprofilen überschreiten kann. Das beweist, dass beide Limits durch Parameter am Rand bestimmt werden. Hochtemperaturplasmen, wie in ITER und DEMO, werden voraussichtlich intrinsisch zentral erhöhte Dichteprofile haben und sollten entsprechend der vorgestellten Ergebnisse bei Dichten oberhalb des GWL in H-Mode betrieben werden können.

Abstract

The high confinement mode (H-mode) is the operational scenario foreseen for ITER, DEMO and future fusion power plants. At high densities, which are favourable in order to maximize the fusion power, a back transition from the H-mode to the low confinement mode (L-mode) is observed. This H-mode density limit (HDL) occurs at densities on the order of, but below, the Greenwald density.

In this thesis, the HDL is revisited in the fully tungsten walled ASDEX Upgrade tokamak (AUG). In AUG discharges, four distinct operational phases were identified in the approach towards the HDL. First, there is a stable H-mode, where the plasma density increases at steady confinement, followed by a degrading H-mode, where the core electron density is fixed and the confinement, expressed as the energy confinement time, reduces. In the third phase, the breakdown of the H-mode and transition to the L-mode, the overall electron density is fixed and the confinement decreases further, leading, finally, to an L-mode, where the density increases again at a steady confinement at typical L-mode values until the disruptive Greenwald limit is reached. These four phases are reproducible, quasi-stable plasma regimes and provide a framework in which the HDL can be further analysed.

Radiation losses and several other mechanisms, that were proposed as explanations for the HDL, are ruled out for the current set of AUG experiments with tungsten walls. In addition, a threshold of the radial electric field or of the power flux into the divertor appears to be responsible for the final transition back to L-mode, however, it does not determine the onset of the HDL.

The observation of the four phases is explained by the combination of two mechanisms: a fueling limit due to an outward shift of the ionization profile and an additional energy loss channel, which decreases the confinement. The latter is most likely created by an increased radial convective transport at the edge of the plasma. It is shown that the four phases occur due to a coupling of these two mechanisms. These observations are in line with studies made at AUG with carbon walls, although in those discharges the energy loss was most likely caused by the full detachment of the divertor.

The density of the HDL depends only weakly on the plasma current, unlike the Greenwald limit, and can be increased by high heating power, again unlike the Greenwald limit. The triangularity of the plasma has no influence on the density of the HDL, though improves the performance of the plasma, since the onset of the degrading H-mode phase occurs at higher densities.

It is explicitly shown that the HDL and also the L-mode density limit are determined by edge parameters. Using pellet fueling, centrally elevated density profiles above the Greenwald limit can be achieved in stable H-modes at a moderate confinement. Future tokamaks will have intrinsic density peaking. Consequently, they will most likely operate in H-modes above the Greenwald limit.

"Every one quoted it, it was full of so many words
that they could not understand."
- Oscar Wilde, 1888

Contents

1. Introduction

1.1. Fusion energy

Power generation by fusion reactions is a promising future energy source. In the sun, energy is produced by the fusion of protons. For energy production on earth, the fusion of two heavy nuclei of hydrogen, i.e. deuterium and tritium, is more feasible:

$$\mathrm{D} + \mathrm{T} \rightarrow {}^{4}_{2}\mathrm{He} + \mathrm{n} + 17.6\,\mathrm{MeV}. \tag{1.1}$$

For an efficient power generation by fusion, sufficiently high densities and temperatures are necessary. The ideal temperature for this reaction is around 15 keV, which corresponds to about 175 million °C. At these temperatures deuterium and tritium are ionized and form a plasma.

The advantages of fusion as an energy source are an abundance of fuel that is available world wide, helium as an unproblematic exhaust gas and the intrinsic safety of the fusion power plants using magnetic confinement.

However, a self-sufficient, steady power production by a burning fusion plasma has not yet been achieved. The task of present day fusion research is to provide the physics and technology basis for the reliable and economical use of fusion as an energy source.

1.2. Magnetic confinement

The temperature of a burning fusion plasma cannot be withstood by any material. Therefore, the plasma is contained in a magnetic field. The charged particles, of which the plasma consists, are bound by the magnetic field lines.

There are several different magnetic field geometry concepts for the confinement of fusion plasmas. The most advanced concept is the tokamak. ITER, which is designed to demonstrate net energy production by a fusion plasma, will be a tokamak.

A tokamak has a toroidal geometry with helically wound magnetic field lines. This magnetic field creates nested surfaces of constant flux, as indicated in figure 1.2. The helical geometry of the magnetic field lines is created by the combination of a toroidal magnetic field, which is created by external coils, and a poloidal magnetic field, which is mainly created by the toroidal current of the plasma. This current is driven by the transformer principle, where a central solenoid acts as the primary winding and the plasma itself as the secondary winding. The plasma current is induced by a current ramp

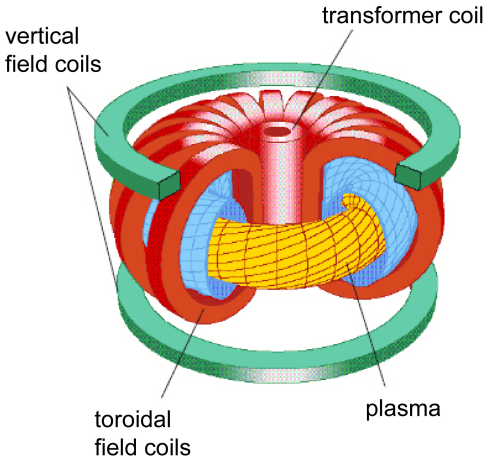

Figure 1.1.: Basic design of a tokamak

in the solenoid which also results in Ohmic heating of the plasma due to its resistivity. However, this current ramp limits the operation time of a standard tokamak. Therefore, tokamaks are by design pulsed devices.

ASDEX Upgrade and JET are two of the largest tokamaks which are currently in operation. In these and other devices the actual fusion relevant topics, such as plasma wall interactions, power exhaust, turbulence physics, plasma heating and improved tokamak operations, are experimentally investigated.

1.3. The ASDEX Upgrade tokamak

ASDEX Upgrade (AUG) is a medium sized tokamak experiment designed to study the physics needed to operate the next generation of fusion reactors such as ITER, which is currently being built in Caderache, France. The major radius of ASDEX Upgrade is 1.65 m and the minor radius is around 0.5 m, which is about half the size of JET and a quarter of the size of ITER. Nonetheless, ASDEX Upgrade is particularly suited to studying the physics phenomena expected for ITER due to the similarities in magnetic configuration, divertor geometry and plasma facing components. AUG is typically operated with a toroidal magnetic field of 2-3 Tesla, core plasma temperatures of up to 10 keV and a core electron density of up to $4.5 \cdot 10^{20}\,\mathrm{m}^{-3}$. These plasma parameters are not sufficient to produce a burning plasma scenario without additional heating (sufficient fusion reactions to heat and maintain the plasma).

AUG is equipped with several external heating systems in addition the intrinsic Ohmic heating by the plasma current. With the neutral beam injection (NBI), high energetic neutral particles are injected into the plasma and ionized there. The NBI system is the main heating system of AUG and provides up to 20 MW of heating power. Additionally, the plasma can be heated by radio waves both at resonant frequencies of the electron gyro

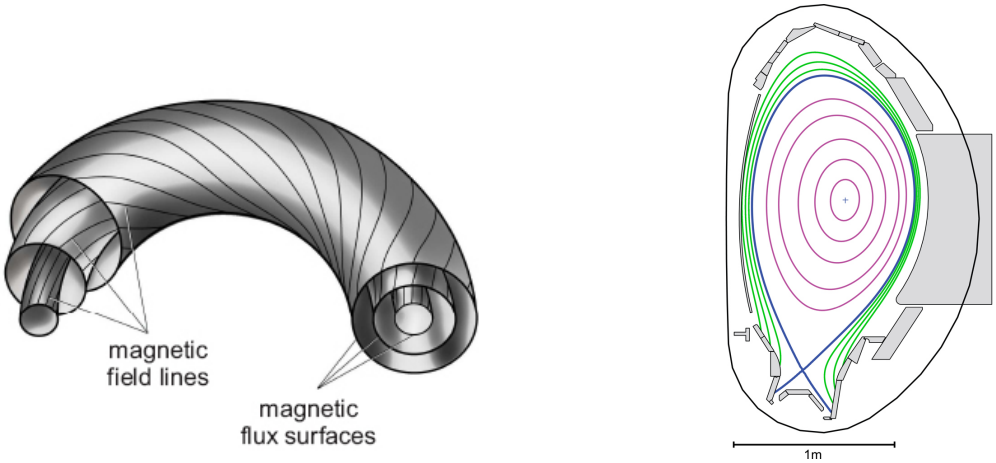

(a) Magnetic flux surfaces spanned by helical magnetic field lines in a torus

(b) Poloidal cross-section of the ASDEX Upgrade experiment with a poloidally diverted magnetic configuration. Closed magnetic field lines are shown in red, the separatrix in blue and the open field lines in green

Figure 1.2.: Magnetic flux surfaces in a tokamak

motion (electron cyclotron resonance heating, ECRH, providing up to 6 MW), and at resonant frequencies for the ion gyro motion (ion cyclotron resonance frequency, ICRF, providing up to 6 MW). With these systems, fusion relevant physics problems, such as the plasma surface interactions, can be addressed and plasma scenarios for subsequent fusion devices developed.

Though future reactors, which aim to produce net fusion energy, will use a deuterium-tritium fuel mixture, AUG runs deuterium plasmas and to minor extent hydrogen or helium plasmas. This is purely to avoid radioactive contamination of the experiment and for easier handling and safety considerations.

ASDEX Upgrade has a divertor configuration. An additional poloidal magnetic field coil alters the magnetic surfaces such that a null-point or an "X-point" in the poloidal magnetic field is created. An example of a poloidally diverted magnetic configuration is shown in figure 1.2b. In divertor operation, the plasma is in direct contact with the walls only at the divertor region. The plasma is separated into two different regions: closed flux surfaces and open flux surfaces, which ultimately intersect the tokamak walls or divertor target plates. The last closed flux surface, also referred to as the separatrix, is the surface which forms an X-point and separates these two plasma regions. The particles outside the separatrix are lost or "scraped off" when they intersect plasma facing components giving this region the name scrape-off layer (SOL).

The divertor can be operated in a detached regime in order to reduce the heat flux on the target plates. The divertor detachment is characterized by a strong reduction

of the ion flux to the target plates. If the temperature is reduced, e.g. by increasing the main plasma density, volumetric processes such as charge exchange collisions and recombination become dominant. This leads to the strong reduction of the ion flux and the plasma pressure in front of the target plates. At full detachment, the plasma is no longer in direct contact with the wall.

In order to achieve a burning fusion plasma, only a limited amount of impurities can be tolerated in the core plasma. High-Z impurities are particularly important to control, because they are not fully ionized in the plasma core, which means they are capable of radiating the plasma energy. Next generation fusion devices require high-Z plasma facing components in order to avoid retention of tritium in the machine as it is observed for carbon due to the formation of hydrocarbon molecules. It is still necessary to study the effect of such wall materials in terms of impurity content and material stability for a stable operation of ITER and future power plants. AUG is the first fusion experiment where the carbon wall (full-C AUG) was replaced by a tungsten coated wall (full-W AUG). After the successful demonstration of a tokamak operation with a tungsten wall at AUG, the largest tokamak in operation, JET, was equipped with the so-called ITER-like wall (JET-ILW), which consists of tungsten in the divertor and mainly beryllium in the main chamber.

ASDEX Upgrade plasmas can be run in different regimes, depending on the operational parameters (heating scenario, fueling, magnetic configuration, etc...). If little or no additional heating power is applied to the plasma then the plasma exists in a low confinement mode or L-mode. In this regime the plasma density and temperature remain low and particle and energy transport across the separatrix is fairly high. However, if sufficient heating power is applied to a plasma in divertor configuration then it can transition to a plasma regime known as high confinement mode or H-mode [2]. In this regime particle and energy transport barriers form at the edge of the plasma, just inside of the separatrix, and the plasma temperature, density, and confinement time are increased by a factor of about 2 above L-mode levels (Fig. 1.3).

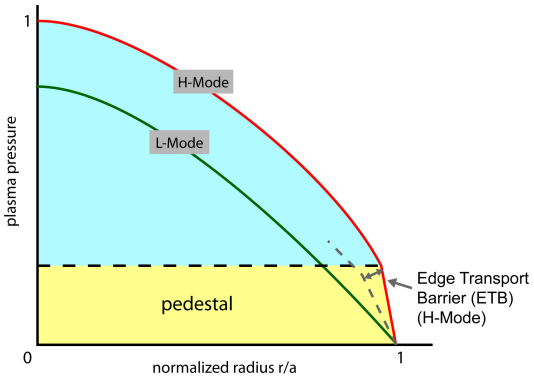

Figure 1.3.: Pressure profiles in L- and H-mode. The pedestal at the edge creates the edge transport barrier and increases the central pressure. [1]

1.4. Motivation and outline

The fusion triple product of density, temperature and energy confinement time

$$n \cdot T \cdot \tau_E \tag{1.2}$$

is a good measure for the performance of a future fusion power plant. The Lawson criterion states that the triple product has to exceed a value of $3 \cdot 10^{21} \frac{\text{keV s}}{\text{m}^3}$ in order to achieve a self-sustained burning deuterium-tritium plasma.

The temperature of a fusion plasma is set by the maximum of the fusion reaction cross-section at around $T \approx$ 10-20 keV. The energy confinement time τ_E is mainly set by the size of the experiment and can only be changed marginally for a given device. The high confinement mode (H-mode) increased τ_E by roughly a factor of 2.

The remaining parameter to increase the performance of the plasma is the density. For the optimum temperature, the power produced by a future fusion power plant can be estimated by

$$P_{fus} \propto n^2, \tag{1.3}$$

thus, an increased density leads to a significant increase of the fusion power.

However, tokamaks experience a disruptive limit for high densities, as described by M. Greenwald in 1988 [3]. This Greenwald limit sets the achievable line averaged density in tokamaks relative to the plasma current and minor radius (see Sec. 2.2).

Furthermore, the H-mode cannot be sustained up to the densities of the Greenwald limit, thus, the confinement is significantly reduced at high densities.

If it were possible to increase the plasma density at high confinement, it would represent an important step towards a feasible, economical utilization of fusion as an energy source. The aim of this work is to investigate this density limit of the H-mode operation, to determine the parameters of this limit, to identify its underlying physics principles and, if possible, to find ways to avoid or to exceed the limit.

The following chapter will give a further introduction to the H-mode, the Greenwald limit and summarizes the current knowledge about the H-mode density limit. The third chapter describes the diagnostics used for the analysis in this thesis, giving special emphasis to the bolometry diagnostics. The fourth chapter discusses the experimental approach to study the H-mode density limit and describes experimental restrictions of the high density operation at ASDEX Upgrade. In the fifth chapter, the empirical observation of four distinct phases on the approach towards the H-mode density limit is reported. The variation of the achieved density by external parameters is discussed in chapter six and several mechanisms, which were proposed to cause the H-mode density limit, are ruled out for the actual dataset at ASDEX Upgrade in chapter seven. In chapter eight the observation of the four phases is discussed and a possible mechanism, which could lead to the H-mode density limit, is proposed. In chapter nine it is shown that the density limits can be exceeded by centrally elevated density profiles. Finally, chapter ten gives a short summary of the main results of this thesis, a short outlook for future devices

and a guideline for further studies of the H-mode density limit in currently operating tokamaks.

2. Introduction to the H-mode density limit

The high confinement mode (H-mode) is the foreseen operational regime for ITER and other future fusion devices. It is characterized by a particle and energy barrier at the edge of the confined plasma which increases the global plasma temperature and density and the energy confinement time. In comparison to the low confinement mode (L-mode), the energy confinement is improved by about a factor of 2. Despite its importance the physics of the H-mode, for example the transition from L- to H-mode, is not yet fully understood. The following section will give an introduction to the present understanding.

It is desired to run future experiments and power plants at the highest plasma densities possible to increase their performance. However, when exceeding a density threshold, the plasma experiences a back-transition into the L-mode regime [4]. The reason for this back-transition is not known and its exploration is the main topic of this thesis. For typical ASDEX Upgrade (AUG) discharges, the H-mode density limit (HDL) is observed to be close to the Greenwald limit. The latter is an empirically found, ubiquitous density limit of the operation of tokamaks.

2.1. The H-mode

The H-mode was discovered at ASDEX, the predecessor of ASDEX Upgrade, in 1982 [2]. It was achieved when applying sufficient heating power by neutral beam injection in a discharge in a poloidally diverted geometry. This regime was reproduced by all other tokamak experiments with poloidal field divertors and also by machines with pure limiter geometry [5].

The H-mode exhibits strong gradients of the electron & ion density and temperature inside the separatrix (see Fig. 2.1), the so-called pedestal (see Fig. 1.3). These strong gradients at the edge form an edge transport barrier (ETB), which suppresses the turbulence in this region. The central density and temperature are determined largely by the edge values and, thus, such increased edge values lead to a higher confinement.

The widely accepted picture of the turbulence suppression, which stabilizes the H-mode and causes the strong gradients at the edge, is based on sheared plasma flows at the edge. The force balance of species α

$$\nabla p_\alpha = n_\alpha q_\alpha (\mathbf{E} + \mathbf{v}_\alpha \times \mathbf{B}) \tag{2.1}$$

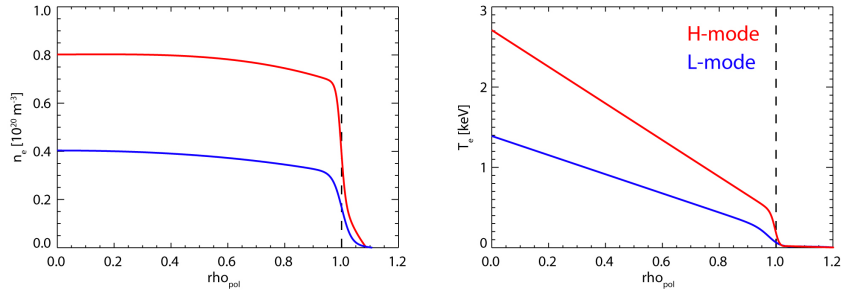

Figure 2.1.: Electron density (left) and temperature (right) profiles over the normalized radius ρ_{pol} of (red) the H-mode and (blue) the L-mode phase of AUG # 28730. The increased gradients close to the separatrix (dashed line) can be seen.

determines its velocity perpendicular to the magnetic field

$$v_{\perp,\alpha} = -\frac{\nabla p_\alpha}{n_\alpha q_\alpha B^2} + \frac{E \times B}{B^2} = v_{dia} + v_{E\times B}, \tag{2.2}$$

where v_{dia} is the diamagnetic drift and $v_{E\times B}$ the $E \times B$ drift. It is assumed, that the radial electric field develops to balance the two above mentioned drifts for the main ions [6], for which they point into opposite directions. In this way the main ions do not exhibit a perpendicular velocity in the laboratory frame and the ion pressure gradient determines the radial electric field [7].

The $E \times B$ drift velocity experiences radial changes in the pedestal region. This gradient leads to strongly sheared plasma flows at the edge, which tears apart radial structures in that region. In this way the turbulent structures, which predominantly cause the transport, are torn apart and the strong pressure gradient can be sustained (see Fig. 2.2).

In [8] it is shown that the radial electric field well has a depth of 15 kV/m at the L- to H-mode transition in AUG. However, the initiation of the L-H transition is not fully

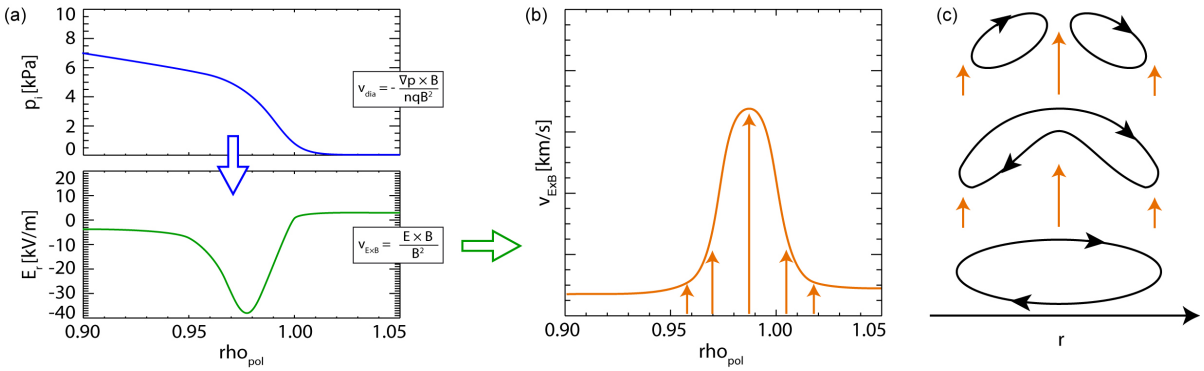

Figure 2.2.: Sketch of the turbulence suppression mechanism of the H-mode: The radial gradient of the ion pressure profile leads to the radial electric field (a), which creates a peaked $E \times B$ drift velocity (b). This non-uniform drift velocity leads to sheared plasma flows, which tear apart radial turbulent structures (c), so-called eddies.

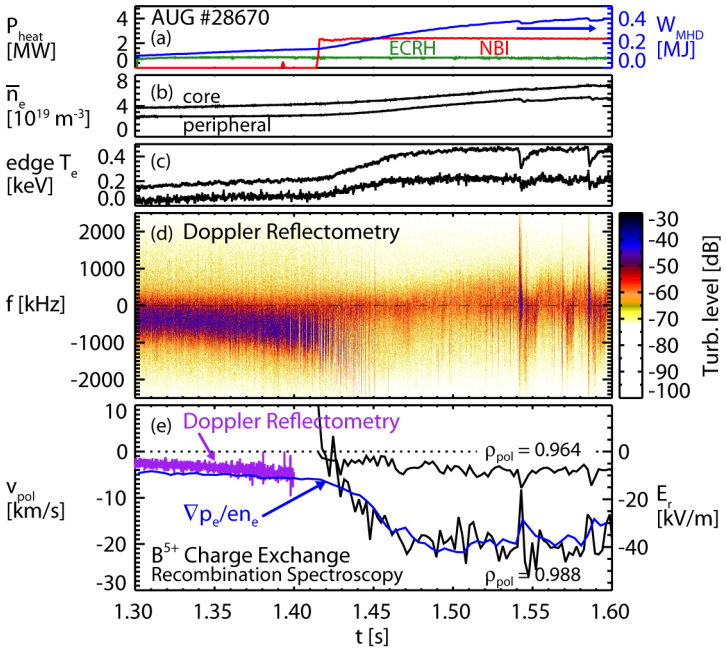

Figure 2.3.: Measurements during an L-H transition. With the additional heating power (a) the plasma transitions into H-mode and the electron density (b) and temperature (c) and plasma stored energy (a) increase. The Doppler reflectometry measures a strong reduction of the turbulence level (d) and the radial electric field is increasing (e). Picture adapted from [9].

understood, though its required auxiliary heating power is of major practical importance, due to the necessity for the design of future tokamaks.

In figure 2.3 several measurements during an L-H transition are shown. With the increase of heating power (a), the L-H power threshold is reached and the H-mode develops. This is seen in the increase of density (b) and temperature (c) and plasma stored energy (a). The measurements of the Doppler reflectometry (d, see Sec. 3.4.5) show, that the turbulence level is significantly reduced when the H-mode develops and the E_r well steepens (e).

The H-mode is accompanied by a quasi-cyclic instability in the pedestal region, known as edge localized modes (ELMs). These instabilities erode the strong gradients at the edge on timescales in the millisecond range. They eject typically between 1-10% of the particles and energy from the confined plasma and will possibly lead to unacceptable thermal loads and erosion on the first wall and divertor plasma facing components in future large devices [10, 11], if not succesfully mitigated. However, they have the beneficial effect of removing impurities out of the pedestal and from the confined plasma [12].

2.2. The Greenwald limit: an empirical L-mode density limit

The Greenwald limit is an empirical limit for the achievable line averaged density of L-mode discharges in tokamaks [3]:

$$n_{GW} = \frac{I_p}{\pi a^2} \ , \tag{2.3}$$

where n_{GW} is the line averaged density in units of $10^{20}\,\mathrm{m}^{-3}$, I_p the plasma current in MA and a the minor radius in m.

When the Greenwald density is reached, the discharge is observed to end by a disruption. Therefore, it represents an operational limit for tokamaks. A detailed description of the Greenwald limit can be found in [13].

Even though this limit is well known and validated by all tokamak experiments, the precise mechanism is not understood. Several different effects are observed to trigger the disruption, such as moving MARFEs (see Sec. 7.3) or MHD instabilities in the core.

The scaling of the Greenwald density combines global plasma parameters which are not directly linked by a physical principle. Deviations from the scaling (Eq. 2.3) are possible. The limit usually takes place at Greenwald fractions, which measures the central line averaged density relative to the Greenwald density, of $f_{GW} = \frac{\overline{n}_e}{n_{GW}} = 0.8 - 1.2$. This is the case for flat electron density profiles, which are typically of high density plasmas in actual tokamaks. To first order, the Greenwald density gives also a rough estimate of the H-mode density limit.

For the currently operated tokamaks, like JET and AUG, the high density plasmas have a high collisionality. In [14] it is shown that the latter leads to inherently flat density profiles, i.e. the pedestal top density is similar to the core density. In this way the Greenwald scaling is found to correlate the line averaged density of the plasma with the (edge determined) density limit.

In section 9 it is shown that the H-mode and Greenwald limit can be considerably exceeded by pellet fueled discharges, which feature centrally elevated density profiles. This shows that the density limits are determined by edge parameters and can be overcome by centrally elevated density profiles.

2.3. The H-mode density limit (HDL)

H-mode discharges, which approach the Greenwald limit, turn into L-mode before reaching the limit. This is observed at several machines at Greenwald fractions between 0.8 and 1 [13].

This H-mode density limit (HDL) is a soft limit, as it is a back transition to L-mode and the plasma operation can be continued with a lower confinement. At this point, a second

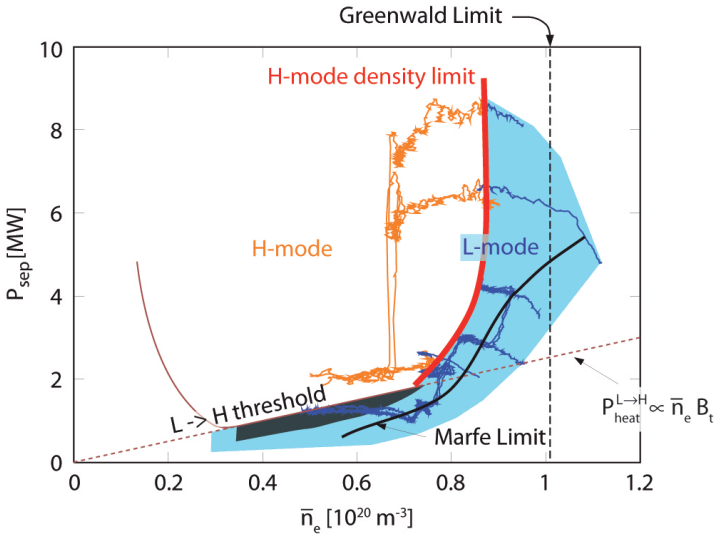

Figure 2.4.: Operational space of the H-mode for high densities in AUG with carbon PFCs. The H-mode density limit is indicated by the solid red line, the Greenwald limit by the dashed line. The orange and blue lines represent the evolution of typical high-density discharges in H-mode with back transitions to L-mode and pure L-mode discharges. Picture adapted from [15].

transition into H-mode is in principle possible by lowering the density or increasing the heating power, as it is shown for one discharge (AUG #29810, see Sec. 6.6).

Figure 2.4 shows the operational space of the H-mode. One can see that an H-mode discharge, which reaches the density of the HDL, turns into L-mode, at which point its density can increase further up to the Greenwald limit. In accordance with this, an H-mode plasma with a flat density profile has not yet been observed to reach the Greenwald limit. However, the exceedance of the Greenwald density limit for H-modes with largely elevated core density profiles but featuring typical edge densities is presented in chapter 9.

The HDL has also to be distinguished from the H- to L-mode back transition, which occurs due to a reduction of the heating power instead of an increase of the electron density (downward movement in Fig. 2.4 instead of a movement to the right). If the heating power is below the L-H threshold, a back transition takes place. Figure 2.4 includes the linear scaling of this L-H power threshold

$$P_{L-H} = 1.67 \frac{\mathrm{MW}}{10^{20}\mathrm{m}^{-3}\mathrm{T}} \overline{n}_e B_t \quad [16], \tag{2.4}$$

where $\overline{n}_e$ denotes the line averaged electron density and B_t the toroidal magnetic field at the geometric plasma center. Note, that the H-L threshold might be lower than the L-H threshold, forming a hysteresis [17].

At high densities, the L-H threshold power diverges from the linear scaling. According to the observations, it is not possible to access the H-mode out of an L-mode with densities

close to the Greenwald limit. The maximum achievable edge density in H-mode appears to be independent from the heating power. [15]

Studies, performed at ASDEX Upgrade and JET with carbon facing components, derived the following empirical scaling for the HDL density.

$$n_{HDL} = 48.2 \frac{q_{\perp}^{0.049\pm0.041} B_t^{0.57\pm0.08} \delta_{av}^{0.11\pm0.11}}{q_{95}^{0.86\pm0.08} R^{1.07\pm0.20}} \quad [18]. \tag{2.5}$$

Here, n_{HDL} is the line averaged density at the limit in $10^{19}\,\mathrm{m}^{-3}$, $q_{\perp}$ the mean power flux density across the separatrix surface in $\frac{\mathrm{MW}}{\mathrm{m}^2}$, δ_{av} the average of upper and lower triangularity q_{95} the safety factor at the 95% flux surface and R the major radius of the plasma in m.

In this thesis the HDL and its proposed mechanisms are revised for the operation of ASDEX Upgrade with purely tungsten coated PFCs. Most mechanisms, which are proposed to cause the HDL in carbon devices, are based on radiative power losses. The radiation distribution and the composition of the edge plasma are drastically modified with the change of the first wall material. The wall material has also an influence on the L-H power threshold. In full-W AUG, the threshold is reduced by roughly 25% with respect to the carbon operation [19]. Thus, it is worthwhile to study the HDL under this vastly changed operational regime and radiation characteristics.

Previous work attributes the cause of the HDL for example to the complete detachment of the outer divertor [18] or additional radiation losses. Mechanisms, that cause increased radiation, are easily identified by bolometry measurements. Therefore, bolometry is the key diagnostic for the study of the HDL. Additionally, crucial information is gained out of the AXUV diode diagnostic, which provides fast radiation measurements in the range of 200 kHz, hence exceeding the time scales provided by the standard foil bolometry by three orders of magnitude (~ 1000).

3. Bolometry and further diagnostics

This chapter describes various diagnostics for analysis of plasma discharges. Overall, about 70 different diagnostics are installed in ASDEX Upgrade. Special emphasis is given to the bolometric measurements, i.e. foil and diode based bolometry, which were extended and optimized during this thesis work. Some other diagnostics, which are also relevant for the studies of the H-mode density limit, are briefly discussed.

3.1. Bolometry

Bolometry is a standard diagnostic for most fusion experiments worldwide. It measures the radiated power along a line of sight (LOS). Typical bolometers are sensitive to a wide range of photon energies, from visible light ($\sim$1 eV) to soft X-ray radiation (several keV). To measure absolutely calibrated values of radiation losses, no optics are allowed between the detector and the light source (the plasma). Therefore, the cameras are installed directly in the vacuum vessel using a pinhole geometry.

Standard bolometry, which is based on metallic absorber foils, is absolutely calibrated due to its diagnostics principles. However, it offers only a time resolution down to 1-2 ms (500-1000 Hz). Therefore, AXUV diode bolometry was installed as a complementary diagnostic, having a high time resolution of 200 kHz, but no intrinsic calibration.

The combination of the two diagnostics are a well suited tool for detecting and localizing slow and fast events of the plasma, especially in the edge region. Due to the full coverage of the poloidal cross section, their high time resolution and the reported radiation losses at the plasma edge during the H-mode density limit [20, 21], they are key diagnostics for the studies of the H-mode density limit.

3.2. Foil bolometry

Foil bolometry is based on radiation absorbing metallic foils. The energy of the incident photons is absorbed by a front layer and converted into heat. Foil bolometers are made out of a thin foil of chemically inert metal (e.g. gold and platinum) placed over a substrate such as Kapton, mica or silicon nitride [22, 23, 24]. A meander like structure on its backside acts as a resistor ($\sim$1200 Ω). By measuring the resistance change using a Wheatstone bridge, the temperature increase is estimated. The corresponding power

deposition on the front of the foil is calculated as [25]:

$$P_{rad} = C_1 \frac{dU}{dt} + C_2 \frac{U}{\tau_c}, \tag{3.1}$$

where P_{rad} denotes the power deposited on the foil, U the voltage across the Wheatstone bridge, τ_c the cooling time constant of the foil and C_1 and C_2 calibration factors taking into account the heat capacity, the resistance and the electronic circuit.

Since the foils absorb practically the full energy of the photons out of the hot plasma, the measurement has a linear response to the photon energy and is easily absolutely calibrated by its temperature characteristics. The sensitive photon energy region is limited on one side by the reflection of low energy photons ($\leq$10 eV) on the metal surface and on the other side by the passing of high energetic photons ($\geq$8 keV) through the absorber.

The theoretical maximum achievable time resolution of the diagnostic is set by the heat transport time from the absorbing foil to the meander, typically on the order of 1-2 ms. This number can be estimated by calculating the heat transport time solely through the substrate. Furthermore, the measurement is affected by electromagnetic noise in the kHz range, effectively reducing the time resolution to about 5-10 ms.

The foils used at ASDEX Upgrade have an absorptive layer that is 4.5 µm thick and a surface area of 5 mm^2. The substrate thickness is between 1.5-20 µm. [23, 22]

The setup of the LOS of the foil bolometry in ASDEX Upgrade can be seen in figure 3.1. The LOS of the 6 pinhole cameras cover the full poloidal cross-section of the experiment. From these measurements the total radiated power of the plasma is derived and two-dimensional distribution of the radiation is calculated using tomographic algorithms [26].

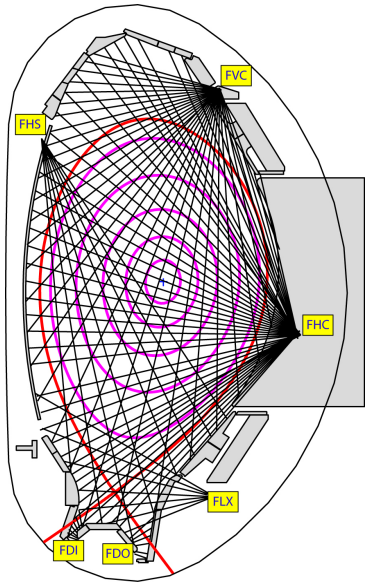

Figure 3.1.: Lines of sight of the foil bolometry of AUG

3.2.1. Improvements to the foil bolometry system

Even though the foil bolometry is a standard diagnostic, which is operated since the start of ASDEX Upgrade, some shortcomings of the diagnostic were detected and resolved during the work of this thesis. The measurements were affected by reflections on the inside walls of the cameras and by ECRH radiation. Both effects have been overcome by counteractive measures, as explained in the following sections. Additionally, the tomographic algorithm was refined (Sec. 3.2.1) and a new camera was installed on the high field side (Sec. 3.3.2).

Reflections inside bolometer cameras

It was found that the measurements of the foil bolometry are severely affected by reflections of visible and VUV light on the stainless steel surfaces inside the cameras.

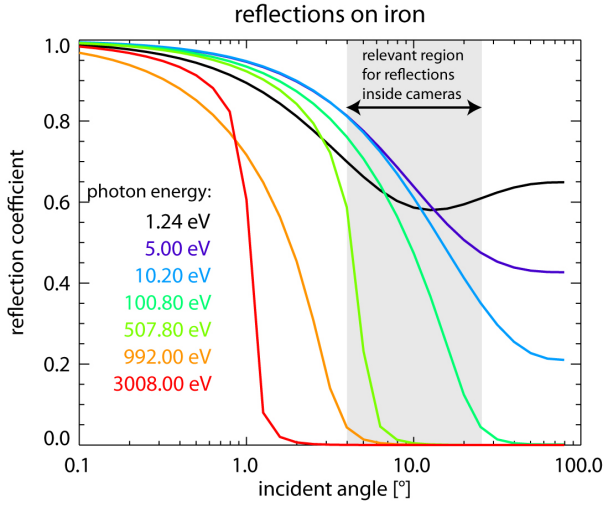

Figure 3.2.: Angular dependence of the reflection coefficient of iron (instead of stainless steel) for different photon energies. The shaded area indicates the range of reflection angles inside the bolometer cameras. The reflection of photons of up to 500 eV significantly perturb the measurements.

So far the reflection coefficients were expected to be very small. However, reflections play a significant role for the actual camera design. In figure 3.2 the reflection coefficients are calculated for an ideal iron surface. The reflection coefficient at the incident angles relevant for the actual cameras (grey box) are on the order of 20-80%. Reflected VUV light between 10-100 eV, where the most power is radiated, can generate significant spurious signals, especially for low incident angles.

Two counteractive measures to avoid the reflections were implemented and tested in the cameras. In one camera the inner walls are equipped with a grooved surface (Fig. 3.3a), which reflects incident light into the direction of the pinhole and not towards the detectors. Secondary reflections are assumed to be negligible. In another camera the inner surfaces were coated with TiO_2 and Al_2O_3 (Fig. 3.3b), which absorbs visible and UV light as well as ECRH stray radiation.

Figure 3.4 shows the measured profiles of the horizontal camera (FHC) before (left figure) and after (middle figure) the implementation of the grooved surfaces. It is compared with the profiles measured by the AXUV diodes (red), to which no changes were made. The diode measurements have to be scaled to compensate degradation effects (see Sec. 3.3.1). Before the correction, the signals of the outer camera parts (indicated in blue) were about a factor of 2 higher than the signals from the central part (green), even though the neighboring channels out of two different camera parts are partially overlapping. These higher signals originate from reflections, which occur under smaller angles and hence are

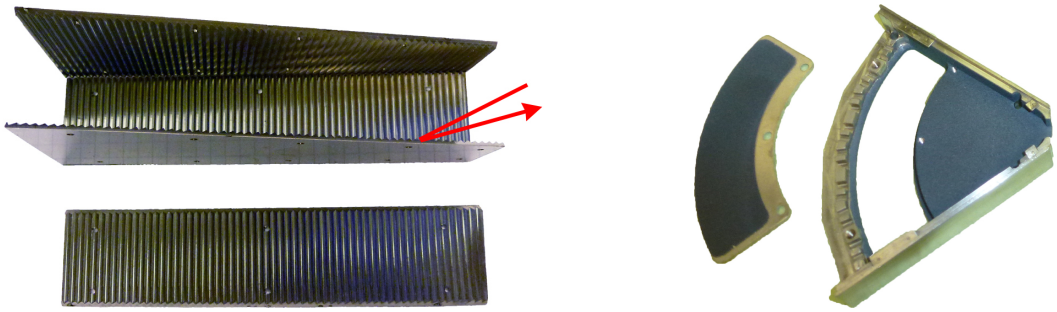

(a) Grooved surfaces with a reflected ray of light (indicated)

(b) Foil camera with TiO_2/Al_2O_3 coating on the inside

Figure 3.3.: Two anti-reflection measures installed inside the cameras.

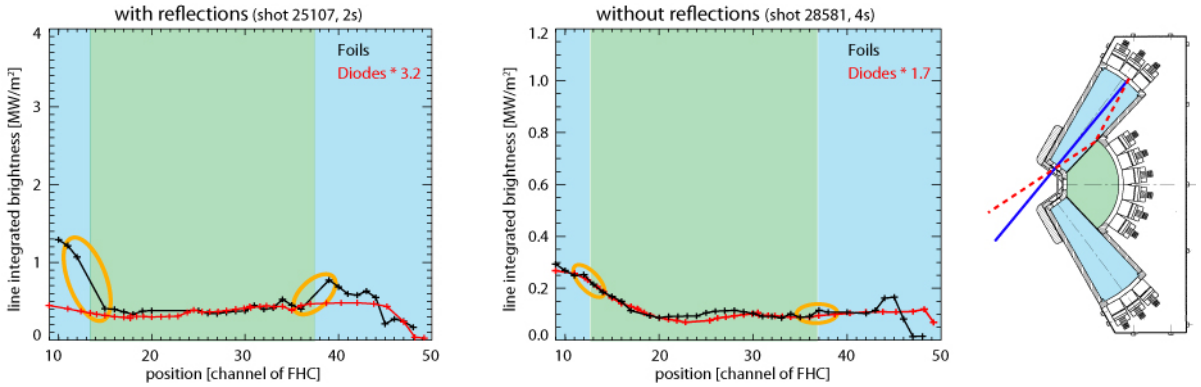

Figure 3.4.: Profiles of the horizontal camera before (left figure) and after (middle figure) the installation of anti-reflection measures and a drawing of the camera (right). The scaled profiles measured by the AXUV diodes are overlaid in red. Steps in the profile appeared when going from the lateral (blue) to the central (green) part of the camera, indicated by the orange circles. These steps were caused by stronger reflections in the lateral camera parts, where the reflection angles are smaller. The overall measured radiation also decreased, as seen by the reduction of the scaling factor for the unchanged diode measurements.

more severe in the outer camera parts. After the installation of the grooved surfaces, the step in the profile is not present any more and the overall measured radiation decreased significantly.

The effects of different anti-reflection measures for visible light are compared in figure 3.5. The combination of both, the grooved surface and the TiO_2/Al_2O_3 coating, is ideal for the suppression of reflections. Therefore, all bolometer cameras are going to be equipped with these wall surfaces in 2013.

The reflections inside the cameras will be avoided with this measure, however, reflections may still occur on the tungsten coated surfaces of the plasma facing components (PFCs).

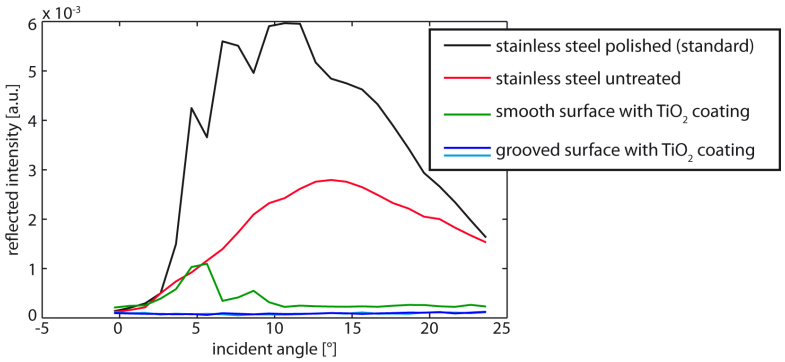

Figure 3.5.: Comparison of different anti-reflection measures for visible light relative to the standard stainless steel surface, which is polished for vacuum compliance. The measurements were made with a 10 mW laser at 630 nm with the setup for the in-situ calibration of the ITER bolometer at the IPP. The reflections on a grooved and uncoated surface could not be measured with the used setup. The combination of grooved surface and TiO_2/Al_2O_3 coating proves to be the best anti-reflection measure, the reflections were below the detection limit of the setup.

These reflections cannot be avoided and may still affect the measurements.

Protection from ECRH radiation

Foil bolometers are additionally affected by ECRH radiation inside the vessel. This effect is known and has been observed for many years [27], but became more severe when the ECRH 2 system [28] was installed at the same toroidal position as the bolometer cameras.

The foils act as an absorber for the microwave radiation, what can lead to an increase of the measured signal by several orders of magnitude. If the polarization of the ECRH

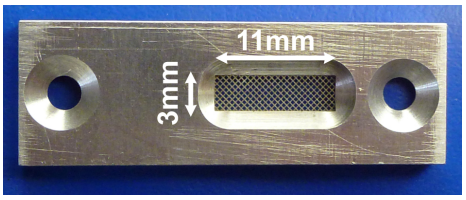

(a) Dimensions of the grid

(b) Grids installed at FVC

Figure 3.6.: ECRH protection grid with an attenuation of 20 dB

radiation is misaligned by only a few percent, the incorrectly polarized radiation can be refracted by the plasma in the direction of the vertical foil camera (FVC). Therefore, protective measures against the ECRH radiation were developed and installed.

The FVC camera, which consists of two individual cameras, was equipped with a protection grid in each pinhole (see Fig. 3.6b). For an efficient attenuation of the ECRH microwaves, with a wavelength of 2 mm, the lattice parameter of the protection grid needs to be smaller by an order of magnitude and as thick as possible. A custom built grid was produced in the size of 3 mm × 11 mm, with a lattice parameter of 0.4 mm and thickness of 0.1 mm (see Fig. 3.6). This grid attenuates the ECRH radiation by 20 dB.

The inside of the cameras act as cavities for the microwaves. Hence the residual ECRH radiation, which still penetrates the protection grid, propagates until it is absorbed by a bolometer foil or a dedicated damping. In order to test this strategy, one part of the FVC camera was coated on the inside with TiO_2/Al_2O_3 (see Fig. 3.3b), which is a good absorber for microwave radiation.

In figure 3.7, the effect of the ECRH protection measures can be seen. Both camera parts are equipped with the protection grid, but only one part was covered on the inside

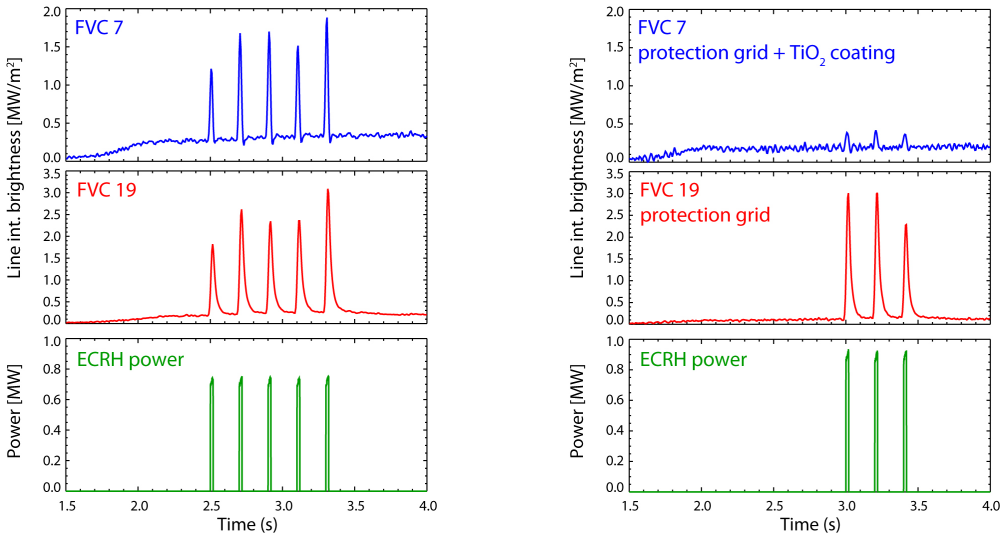

(a) without ECRH protection

(b) with grid and partial TiO_2/Al_2O_3 coating

Figure 3.7.: Test blips of the ECRH heating during two AUG discharges, without (left, AUG #28389) and with (right, AUG #28730) ECRH protection. Channel FVC 7 is equipped with the protection grid and the TiO_2/Al_2O_3 coating and channel FVC 19 only with the grid. Channel FVC 7 shows a significant reduction of the spurious signal. In channel FVC 19, the disturbance has a similar level. Only the combination of both counteractive measures leads to an effective reduction of the spurious ECRH signal.

with TiO_2/Al_2O_3. Even though the grid attenuates the ECRH radiation by 20 dB, the spurious ECRH signal of the camera without coating (channel FVC 19, middle figures) is similar with and without the grid. This indicates that the balance of in- and outgoing radiation through the pinhole is leading to the same level of cavity radiation inside the camera irrespective of the grid. Thus, not only the direct incident of the ECRH radiation but also the cavity radiation inside the camera have a strong effect on the bolometers. For the camera with inner housing coated by TiO_2/Al_2O_3, this ECRH radiation is immediately absorbed and the cavity radiation cannot develop. The top figures of 3.7 show, that the combination of grid and coating does effectively reduce the spurious signal of the ECRH radiation.

High field side cameras

The divertor is the region were most of the power is radiated by the plasma under normal operation. One of the main challenges of the bolometry is to diagnose the radiation distribution in this region for optimization of the power exhaust.

The LOS of the vertical cameras of foil and diode bolometry (FVC/DVC), which observe the divertor, also observe the core of the plasma (grey LOS in 3.8). Thus, core and divertor radiation cannot be disentangled well enough by these vertical LOS. This also induces artifacts in the tomographic reconstruction of the poloidal radiation distribution.

Additional vertical LOS needed to be introduced that only observe the divertor and not the core radiation. Therefore, one camera with 8 LOS observing the divertor from the upper high field side (see Fig. 3.8) was installed in 2012. In addition one diode bolometry camera (see Sec. 3.3) with 16 LOS and a similar viewing geometry was installed. Both cameras allow a more detailed observation of the divertor region and improve the tomographic reconstruction.

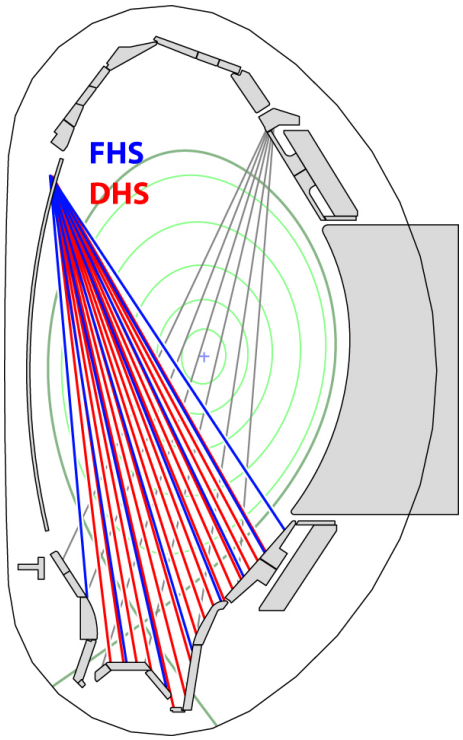

Figure 3.8.: LOS of the high field side cameras of foil (blue) and diode bolometry (red), and the LOS of the vertical foil camera (FVC), which observe the divertor (grey)

Improvements for the tomographic reconstruction algorithm

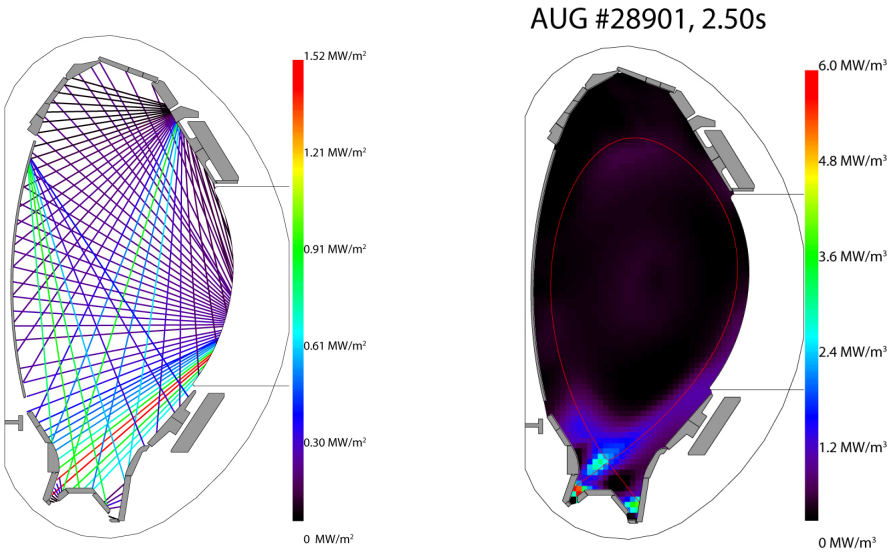

(a) Input: position and brightness of LOS

(b) Result: 2D poloidal emissivity distribution

Figure 3.9.: Example of the tomographic reconstruction of the two dimensional poloidal radiation distribution.

Figure 3.9 shows an example of the tomographic reconstruction of the two-dimensional poloidal radiation distribution. The reconstruction of the 2D profile with a limited set of LOS is an ill-posed set of equations. To solve this, additional information, e.g. based on physical assumptions, is needed. Therefore, it is assumed that due to parallel transport, the gradients in the radiation are higher perpendicular to the flux surfaces than parallel to them.

The inputs of the tomographic algorithm [26] are the line integrated measurements of the bolometry, the geometry of the magnetic equilibrium (see Sec. 3.4.1) and a set of relative gradients in the parallel and perpendicular direction to the flux surfaces. The code minimizes the χ^2 error of the line integrated measurements with an regularization integral which describes the curvature of the 2D profile.

So far the input parameters for parallel and perpendicular radiation gradients were different for the divertor and the main chamber. A new method was implemented which defines the parameters locally for various regions: the confined plasma, the SOL inner and outer divertor and the X-point. The values are optimized so that typical artifacts, which are arising from the ill-posed problem of deconvolution, are minimized. The user's input is still required to adjust and validate each deconvolution. Figure 3.10 illustrates the old and the new method to define input parameters. The new method is able to

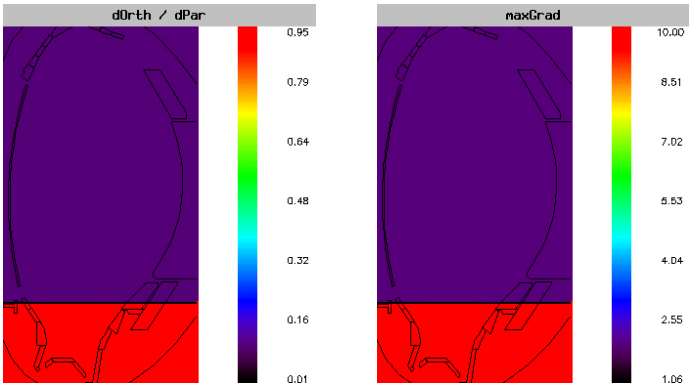

(a) Old method: $\nabla_\perp/\nabla_\parallel$ **(b)** Old method: ∇_{max}

(c) New method: $\nabla_\perp/\nabla_\parallel$ **(d)** New method: ∇_{max}

Figure 3.10.: Local input parameters of $\nabla_\perp/\nabla_\parallel$ (left) and ∇_{max} (right), which define the relative allowed emissivity gradients perpendicular and parallel to the flux surfaces for the tomography.

reconstruct more localized radiation in the divertor and more poloidally symmetric in the confined region, as it is expected from basic plasma physics.

Figure 3.11 compares the results of reconstructions with the old and the new method using the same input data. As indicated with the orange lines, artifacts in the deconvolution are significantly reduced by the new method. The increased radiation in the core on the left picture falsely points out an impurity accumulation, which did not exist in this discharge. A more localized radiation in the divertor, which is observed by a single LOS, can now also be resolved. However, there is always a trade-off between the reconstruction of localized radiation, the appearance of artifacts and the poloidal smoothing of the radiation.

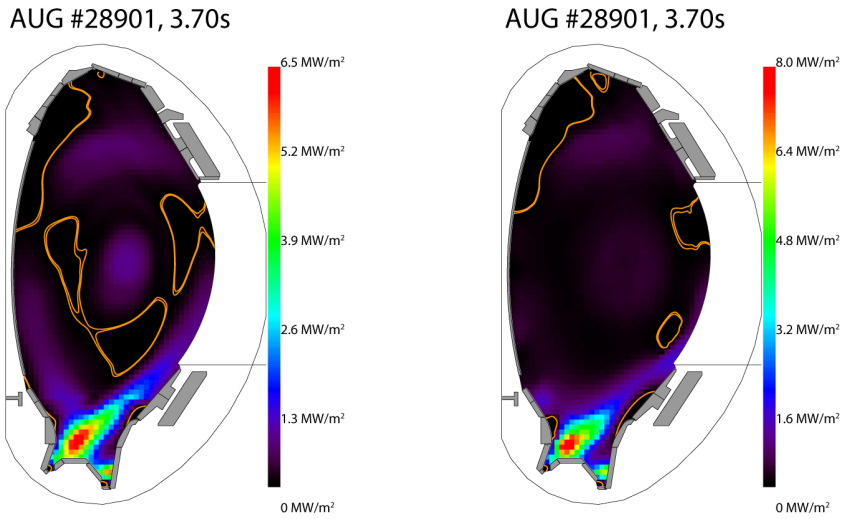

(a) Old method **(b)** New method

Figure 3.11.: Comparison of the results of the old (left) and new (right) methods to determine the input parameters for the tomographic reconstruction. The orange lines indicate regions with negative emissivity. The new method generates fewer artifacts (such as negative emissivities or spurious signals of an impurity accumulation) and a more localized radiation pattern.

Within this thesis, the new method is also applied to measurements from the JET tokamak. The new method improves the deconvolution significantly (see Fig. 3.12). Although the regions of negative emissivities becomes bigger with the new method in comparison to the standard method of JET, the number of artifacts is reduced. Figure 3.12 compares a standard discharge of JET (top) with a nitrogen seeded discharge (bottom). The nitrogen in injected in order to reduce the power flux onto the divertor plates by radiating the energy in the divertor volume. The new method reveals that the main radiation originates in case of the nitrogen seeding from the X-point and in standard operation from the volume in front of the inner divertor target plates. With the standard method, the radiation was always reconstructed in the X-point region, leading to false conclusions about the effect of nitrogen.

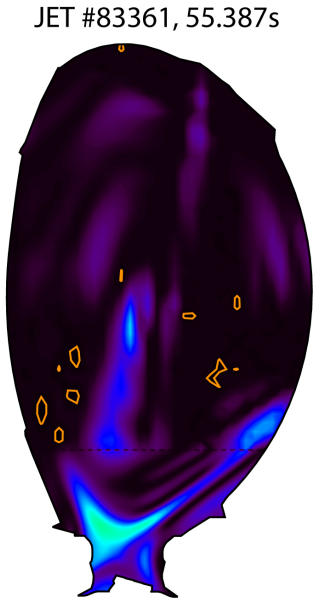

(a) Standard method at JET, without N seeding

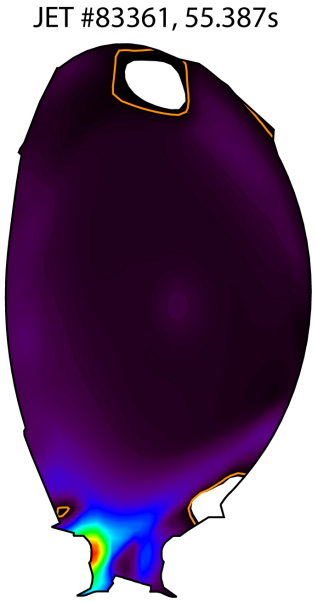

(b) New method, without N seeding

(c) Standard method at JET, with N seeding

(d) New method, with N seeding

Figure 3.12.: Results of the radiation reconstruction by the standard method of JET (left) and the new method (right) applied to JET discharges without (top) and with nitrogen seeding (bottom). The number of artifacts is significantly reduced. With the standard method, the divertor radiation was always reconstructed in the X-point region, the new method localizes the radiation either at the X-point or in front of the inner divertor target.

3.3. AXUV diode bolometry

The diode bolometry system is a fairly new diagnostic which was installed in 2010 [29] and further improved and extended as a part of a master thesis [30] and this thesis. The diagnostic is based on AXUV (Absolute eXtreme UltraViolet) photodiodes. Their generated photocurrent is supposed to be proportional to the incident radiation power [31, 32].

The diodes offer a time resolution of better than 500 ns [33]. However, they lack sensitivity in the VUV range (see Fig. B.1) and, therefore, cannot be calibrated absolutely for the required wavelength range from 1 eV to 10 keV. Furthermore, the sensitivity of the diodes undergoes a degradation when exposed to plasma radiation, changing the calibration drastically.

The actual layout of the AXUV diagnostic at AUG consists of 256 LOS distributed among eight cameras. Each camera is equipped with one or more 16-channel AXUV arrays of the type AXUV16ELG by International Radiation Detectors Incorporated (IRD,Inc.) [34]. Five pinhole cameras are installed in one sector and observe the full poloidal cross-section of the experiment from different positions (Fig. 3.13). One pinhole camera is installed toroidally 180° apart from the others for toroidal asymmetry studies (e.g. [35]). Two additional tangential cameras are also installed and are described in section 3.3.2.

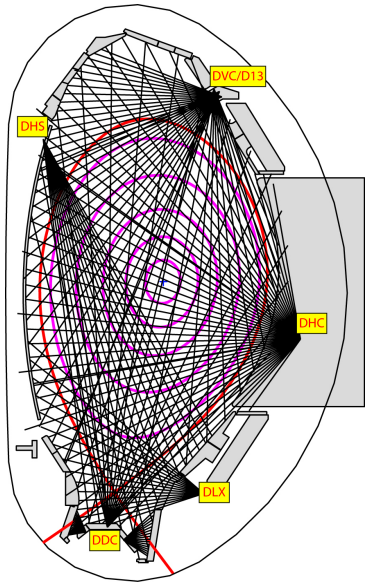

Figure 3.13.: Lines of sight of diode bolometry in sector 5 of AUG

As one of the first diagnostics the data acquisition is based on the new SIO (serial input/output) system introduced by the electronics and computer group at AUG [36]. The SIO system offers a maximum sampling rate of 2 MHz. However, the actual sampling rate of the AXUV data acquisition is reduced to 500 kHz (in line with the 200 kHz filter on the boards) to allow data from more LOS to be recorded. Nevertheless, it is already one of the fastest diagnostics on the experiment. About 2 GB of data are recorded for every discharge.

A detailed description of the diagnostics can be found in the appendix B.

3.3.1. Degradation of the diode sensitivity

Previous work [30] showed that the AXUV diodes undergo a strong degradation (of the sensitivity) in the environment of a tokamak experiment.

For a detailed observation of the degradation, all of the cameras were equipped with

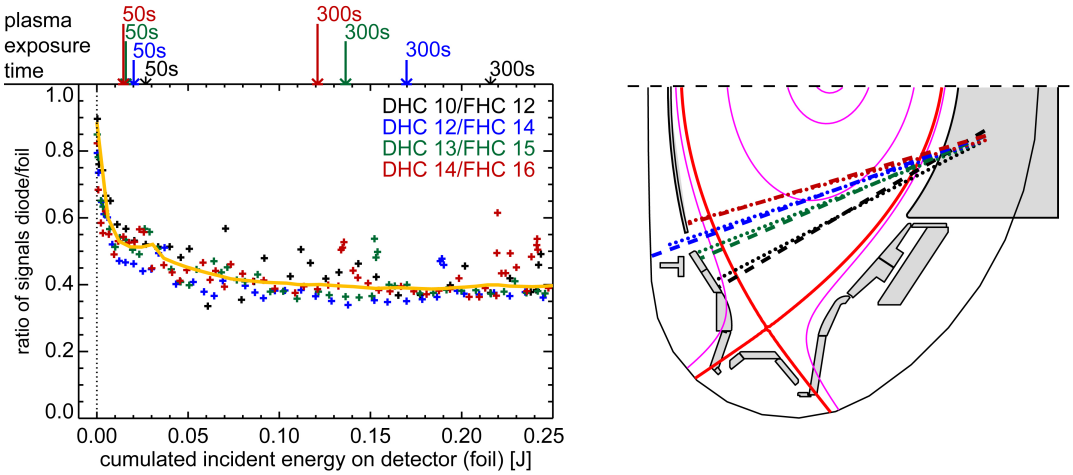

Figure 3.14.: Left: Discharge-averaged ratio of diode measured signal to foil measured signal from 4 LOS doublets plotted over the time history of the cumulated incident radiation energy. The time the diodes were exposed to the plasma radiation is shown on top. Right: Poloidal cross-section of ASDEX Upgrade indicating the positions of the observed LOS of foil (dashed) and diode bolometers (dotted)

new diodes for the ASDEX Upgrade experimental campaign, which started in November 2010.

In figure 3.14 the ratios of LOS doublets of diode and foil bolometry are plotted against the total incident radiation energy for the beginning of the experimental campaign. At the beginning the diode signal is almost as high as the foil signal. However, the diode sensitivity decreases strongly within 50 seconds of plasma operation, according to the first 9 successful discharges of the experimental campaign. After roughly 300 seconds of plasma operation the sensitivity remains constant and the selected diode signals are a factor of 2.5 lower than the foil measurements. The diode sensitivity does not change significantly for the next 1000 discharges (∼3000 s of plasma operation) after this initial degradation. This kind of saturating degradation is also reported for other diode types [37]. A more detailed picture of the degradation and its mechanisms is given in appendix C.

To retrieve useful data out of the measurements, the sensitivity after this initial degradation needs to be known. Therefore, the diodes were post calibrated by the Physikalisch-Technische Bundesanstalt (PTB) at the synchrotron BESSY in Berlin.

Figure 3.15 shows a measurement of the degraded sensitivity. In summary, there is a strong decrease of sensitivity for VUV radiation (∼3-50 eV) and for photons between ∼100-400 eV. The sensitivity for visible light (∼1-3 eV), between 50-100 eV and above 400 eV is only marginally affected. The diodes remain sensitive for these three radiation bands.

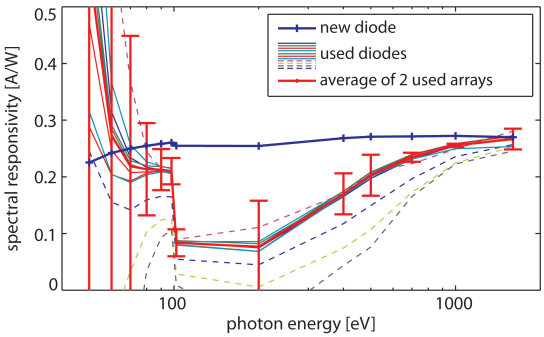

Figure 3.15.: Measurements from the PTB: Degenerated responsivity of several diodes from different arrays, averaged responsivity (red) and initial responsivity (blue).

3.3.2. Extensions to the AXUV diagnostic

The diode bolometry diagnostic was extended by three new cameras. One new camera on the high field side was already introduced in section 3.2.1.

Two cameras with a tangential viewing geometry (see Fig. 3.16) were installed in 2010. Both observe the edge of the plasma with 16 parallel LOS in a radial spacing of 2 mm.

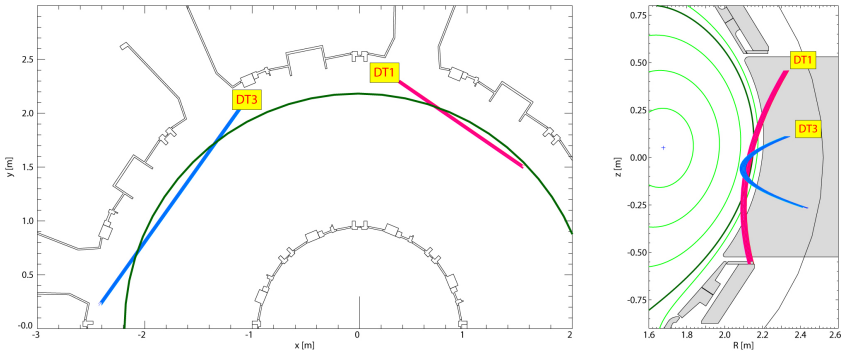

Figure 3.16.: Tangential cameras of the diode bolometry in AUG. Toroidal (left) and poloidal (right) cross-section with indicated separatrix (dark green) and flux surfaces (light green).

This high spatial resolution was designed to allow for detailed studies of the radiation at the pedestal of the plasma. Unavoidably, the viewing volumes of the single LOS strongly overlap due to the design of the cameras and the angle of aperture. By using a forward model, the radial emissivity profile was reconstructed and various profile shapes were checked for consistency [38]. For this reconstruction, the viewing volume of the camera is simulated and the expected measurements are calculated from the radial emissivity profile.

The measurements of one tangential camera, the modeled emissivity and the reconstructed measurements can be seen in figure 3.17. The emissivity profile consists of a spline function which initially is radially constant. By a χ^2 reduction, the spline function

is fitted so that the calculated line integrated brightnesses resemble the actual measurements. Also various different parameterized functions of the emissivity profile were used for the forward model, out of which a double-peaked structure always resulted in the best reconstruction.
A major result of [38] is that the relative measurement errors, especially systematic errors of the relative diode calibration, inhibit a reliable reconstruction of the emissivity profile at the edge. The systematic errors of the measurement need to be below 5% to determine reliably the profile shape of the pedestal radiation.

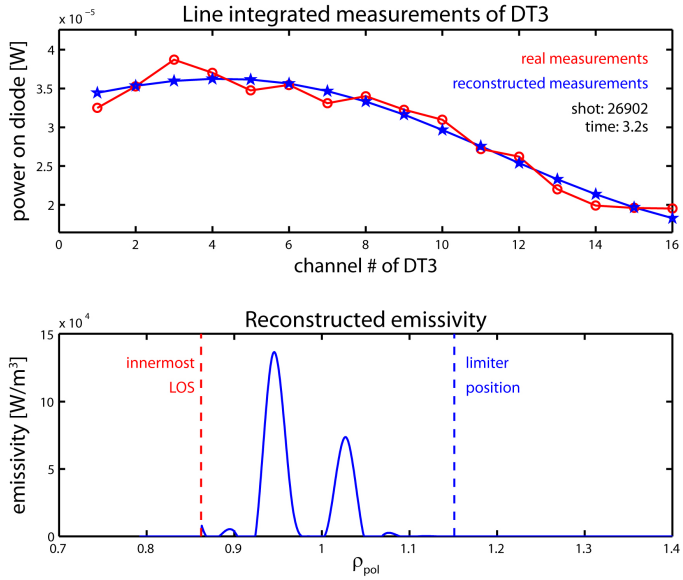

Figure 3.17.: Top: Line integrated measurement of the tangential camera in sector 3 (red) and simulated measurement out of the reconstructed emissivity (forward model). Bottom: Reconstructed local emissivity profile. Figures adapted from [38].

3.4. Further diagnostics

Several other diagnostics, apart from diode and foil based bolometry, are used for the analysis of the H-mode density limit. The following section will give a brief overview of the most important diagnostics which were used. For detailed information on the specific diagnostics, references are noted.

3.4.1. Magnetic measurements and equilibrium reconstruction

The magnetic equilibrium defines 2D poloidal geometry of the plasma. It is calculated by equilibrium codes, such as CLISTE [39], which solve the Grad-Shafranov equation

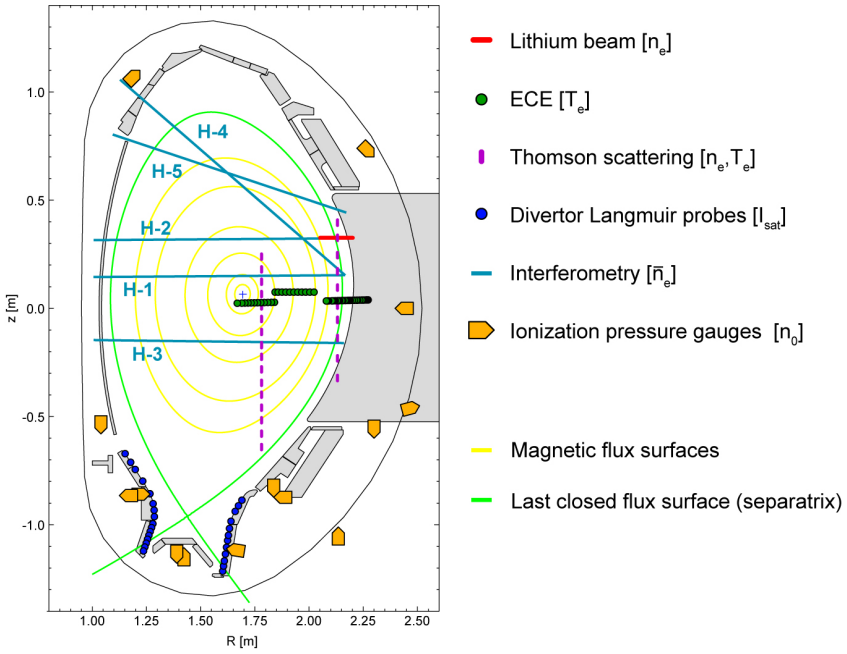

Figure 3.18.: Poloidal arrangement of the frequently used diagnostics in this thesis

using the currents of the magnetic field coils and additional plasma current distribution measurements from magnetic pick-up coils inside or outside the vacuum vessel.
The 2D equilibrium retains information about the flux surfaces (yellow lines in Fig. 3.18), which are nested surfaces of constant toroidal or poloidal magnetic flux (Ψ_{tor} or Ψ_{pol}). The pressure is constant on these surfaces and it is also assumed that most plasma parameters like temperature and density are constant on flux surfaces inside the separatrix because of the high parallel transport. Therefore, these parameters are often represented by one-dimensional profiles, plotted against the normalized flux coordinate

$$\rho = \sqrt{\frac{\Psi - \Psi_{magn.axis}}{\Psi_{separatrix} - \Psi_{magn.axis}}}. \tag{3.2}$$

This coordinate is 0 for the magnetic axis and 1 at the separatrix. Depending on the definition, either the poloidal flux ($\Psi_{pol} \Rightarrow \rho_{pol}$) or the toroidal flux ($\Psi_{tor} \Rightarrow \rho_{tor}$) is used for this normalization.

3.4.2. Electron density and temperature measurements

The electron density and temperature are very important parameters to characterize the plasma. ASDEX Upgrade is equipped with several diagnostics to measure both.

Interferometry measures the refractive index of the plasma along the path of a laser. It can retain a line integrated electron density, since the refractive index is dependent of

the electron density:

$$N = \sqrt{1 - \frac{\omega_{pe}^2}{\omega^2}} = \sqrt{1 - \frac{n_e e^2}{\epsilon_0 m_e \omega^2}} \approx 1 - \frac{1}{2}\frac{n_e e^2}{\epsilon_0 m_e \omega^2} \ , \tag{3.3}$$

where $\omega_{pe} = \sqrt{\frac{n_e e^2}{\epsilon_0 m_e}}$ is the electron plasma frequency, ω the laser frequency, n_e the electron density and m_e the electron mass.
Accordingly, the laser beam experiences a phase shift of

$$\Delta\phi = \int (N-1)\,\frac{\omega}{c} dl \approx -\frac{e^2}{2c\epsilon_0 m_e \omega} \int n_e dl \tag{3.4}$$

along its path through the plasma, which is measured by the interferometry system.
The interferometry system of ASDEX Upgrade provides the line integrated density along five horizontal (H-1 to H-5, light blue lines in Fig. 3.18) and three vertical lines (V-1 to V-3, not shown in Fig. 3.18), representing a crude spatial resolution. Generally, H-5 is referred to as edge line integrated density and H-1 as core line integrated density.
One refers often in tokamak research to the line averaged density of the plasma, given in m^{-3}. This is the line integrated density, as measured by the interferometry in m^{-2}, divided by the length of the laser path inside the separatrix. [40]

The **lithium beam** impact excitation spectroscopy (Li beam) measures the electron density with a high radial resolution at the edge of the plasma [41]. Lithium atoms are accelerated outside the plasma and injected into the plasma as neutral particles from the low field side. The atoms interact with the electrons of the plasma and emit line radiation, which is observed spectroscopically. The electron density profile can be calculated from the emissivity profile along the beam path. The position of the Li beam is indicated by the red line in figure 3.18.
The radial extension of the measurement is limited by attenuation of the Li beam by ionization. Due to the high neutral density (see Sec. 4.2), for most discharges dedicated to the study of the H-mode density limit the Li beam did not penetrate the plasma even as far as the separatrix, and, therefore, it provides valuable data only for a few discharges.

The **Thomson scattering** diagnostic offers both electron temperature and electron density measurements [42]. Intense laser pulses are launched into the plasma and the light is scattered by the free electrons. The spectrum of the scattered light has a Gaussian shape if the electrons are in thermal equilibrium. The width of the Gaussian is defined by the electron temperature and the intensity related to the electron density. The measurements are localized and not line integrated. The radial location of the laser beam and the vertical position of the observed scattering regions define the measurement locations.
The high noise of the signals often restricts the use of the diagnostic [43].

The **electron cyclotron emission (ECE)** diagnostic measures the electron temperature [44]. Ideally, the plasma is optically thick for the second harmonic of the electron cyclotron frequency. Therefore, the plasma radiates in this frequency range like a black body and the electron temperature can be derived by the Rayleigh-Jeans law. The frequency is correlated to the magnetic field strength, which is inversely proportional to the major radius, and thus defines the location of the measurement. The diagnostic can in principle measure the whole electron temperature profile from the LFS, since the magnetic field and the cyclotron frequency increase in a tokamak for smaller radii.
The diagnostic is limited for high densities by the cutoff density, above which the wave cannot propagate through the plasma any more.

$$n_{e,cutoff} = 1.94 \cdot 10^{19} \frac{1}{\mathrm{m^3 T^2}} \cdot B^2 \quad \text{(for the second harmonic X-mode).} \tag{3.5}$$

For the high densities of the HDL studies, the measurements were only possible for discharges with a high toroidal magnetic field. A further difficulty is that the plasma is not optically thick at the edge, leading to the effect of shine-through. A spurious peak of electron temperatures is observed in the SOL region, especially when steep gradients in temperature or density are present. [45]

3.4.3. Langmuir probes

Langmuir probes are installed in various positions on the plasma facing components (PFC) in ASDEX Upgrade. Depending on their setup, they can measure various parameters, such as the floating potential or the ion saturation current ($I_{i,sat}$). From these measurements and according to the probe theory, one can determine for example the electron density or temperature in front of the probe or the heat flux to the probe. [46]
Picture 3.19 indicates the positions of the fixed Langmuir probes in the outer lower divertor of ASDEX Upgrade. In this thesis mainly the measurement of $I_{i,sat}$ is used, which is in first order a measurement of the electron density

$$n_e = \frac{I_{i,sat}}{A_{probe} e c_s}, \tag{3.6}$$

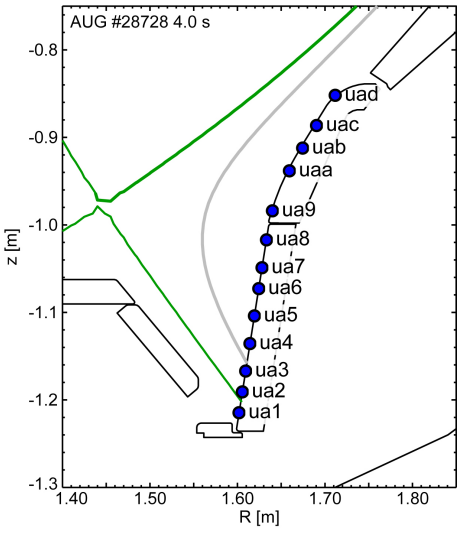

Figure 3.19.: Position and nomenclature of the Langmuir probes in the outer divertor.

with the probe area A_{probe} and sound speed c_s.
$I_{i,sat}$ is a indicator for the detachment of the divertor plasma. Approaching the detachment, $I_{i,sat}$ first increases strongly when the divertor goes into the high recycling regime

and then drops down to zero when the divertor plasma is completely detached. At this point the plasma is no longer in contact with the probe. [47]

3.4.4. Ionization gauges

The density of neutral gas in the vacuum vessel is measured by ionization pressure gauges. The direct measurement of the gauges is the neutral flux density to their aperture. The neutral gas density can be calculated with the knowledge of the neutral gas temperature. Room temperature is assumed for the neutral gas behind the PFCs. [48] Several of these ionization gauges are installed at different poloidal and toroidal locations as shown in figure 3.18.

Since the discharges dedicated for this thesis are operated at very high neutral pressure, many gauges might be saturated and data is of limited use for the analysis. Indications for the saturation of the pressure gauges are discussed in section 4.2.

3.4.5. Evaluation of the radial electric field

An essential measurement for this thesis is the determination of the radial electric field (E_r) at the edge of the plasma. Within the last years several diagnostic techniques were implemented at ASDEX Upgrade to evaluate the edge electric field.

Doppler reflectometry

Doppler reflectometry measures the velocity of electron density fluctuations created by turbulence [49]. It is based on the backscattering of an obliquely injected microwave beam at the cut-off layer due to the presence of electron density fluctuations. The velocity of the fluctuations is calculated from the Doppler shift in the spectrum of the backscattered beam. The probing beam is oriented perpendicular to the magnetic field to measure only the perpendicular velocity of the fluctuations $u_\perp$. The measured velocity consists of the intrinsic phase velocity of fluctuations (v_{ph}) and the $E \times B$ velocity of the background plasma ($v_{E\times B}$):

$$u_\perp = v_{ph} + v_{E\times B} \approx v_{E\times B} = \frac{E_r}{B} \tag{3.7}$$

In [49] it is shown that the phase velocity is negligible with respect to the $E \times B$ drift velocity. Therefore, with knowledge of the local magnetic field E_r can be calculated out of the measured perpendicular velocity of density turbulence.

Furthermore, the intensity of the Doppler shifted component gives the relative turbulence level. This is used as an indication if the plasma is in the turbulence suppressing H-mode regime or in the turbulent L-mode regime.

Charge exchange recombination spectroscopy (CXRS)

CXRS measures the temperature and density of impurity ions and their rotation velocity. At ASDEX Upgrade two independent high resolution CXRS systems observe the plasma edge, one in the toroidal and one in the poloidal direction. [50]
The edge E_r inside the separatrix can be calculated by the radial force balance equation

$$E_r = \frac{1}{n_\alpha Z_\alpha e}\frac{dp_\alpha}{dr} - v_{pol,\alpha}B_{tor} + v_{tor,\alpha}B_{pol} \tag{3.8}$$

where n_α denotes the density, Z_α the charge, p_α the pressure, $v_{pol,\alpha}$ the poloidal rotation and $v_{tor,\alpha}$ the toroidal rotation of the impurity species α, respectively. This equation holds for each ion species separately and all quantities are provided by the two edge CXRS systems. B_{pol} is the poloidal and B_{tor} the toroidal magnetic field, which are both known from the magnetic equilibrium reconstruction. [7]
To reconstruct the radial E_r profiles using the CXRS diagnostic, radial sweeps of the plasma are required. Therefore, "Raus" scans, where the outer radius of the separatrix is moved radially by about 2 cm, are included in the discharge program. This restricts the availability of the E_r evaluation to dedicated time windows with a duration of about 0.5 s within a discharge. [50]

Kinetic profiles

The radial force balance (3.8) is valid for each impurity species and also for the main ions, i.e. deuterium. In reference [7] it is shown that the main ions do not move perpendicular to the magnetic field ($v_i \times B = 0$), thus E_r can be estimated by the pressure profile of the main ions:

$$E_r \approx \frac{1}{n_i e}\frac{dp_i}{dr} = \frac{1}{n_i e}\frac{d\left(T_i \cdot n_i\right)}{dr} = \frac{1}{e}\left(\frac{dT_i}{dr} + \frac{T_i}{n_i}\frac{dn_i}{dr}\right) \tag{3.9}$$

For high densities, the collisions between the electrons and ions are frequent enough to equalize the electron and ion temperature ($T_e \approx T_i$), i.e. electrons and ions are coupled. For the typical HDL discharges it is additionally assumed that the amount of impurities in the plasma is negligible. Thus, the densities of electrons and ions are equal ($n_e \approx n_i$). Therefore, also the electron temperature and density measurements (Sec. 3.4.2) can be used to determine E_r.

Comparison of E_r diagnostics

Figure 3.20 shows the comparison of the edge radial electric field from a HDL discharge by all three discussed diagnostics. They agree in profile shape and depth of the E_r well within the uncertainties. The Doppler reflectometry data need to be shifted slightly in the radial direction in this case to match the other measurements.

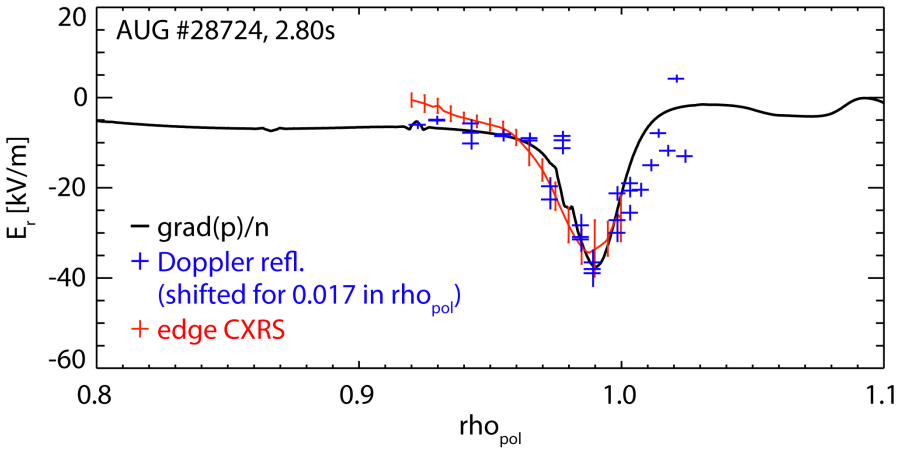

Figure 3.20.: Radial electric field determined by $\frac{1}{en_e}\frac{dp_e}{dr}$ (black), CXRS (red) and Doppler reflectometry (blue, shifted radially for 0.017 in rho_{pol} in order to match the other measurements) from AUG #28724 at 2.8 s

4. Experiments

During the experimental campaigns in full-W ASDEX Upgrade between 2011 and 2013, several dedicated gas ramp discharges for the H-mode density limit studies were made. The parameters to reach the HDL, i.e. the neutral gas pressure, were achieved by extending the standard operation of AUG by switching off the cryo-pump system.

In the following, the parameters for these experiments are explained and an overview of the conducted experiments is given. Emphasis is placed on the vast fueling of the plasma and required operation of H-modes in AUG. Finally, the general evolution of an HDL discharge is described.

4.1. Discharge parameters

For the studies of the HDL, gas ramp discharges were conducted to achieve the maximum densities necessary for the HDL and the disruptive L-mode density limit. Thus, a successful discharge ends in a disruption. The gas ramp is realized by increasing the amount of neutral gas injected in the vacuum vessel by several gas valves. A closer look on the fueling of the discharges and the achieved neutral densities is given in the subsequent section 4.2.

The default plasma current of the HDL discharges is $I_p = 0.8\,\mathrm{MA}$. The forces, which are induced into the device components by the disruption, are tolerable for this current and no mitigation mechanism has to be applied. The toroidal magnetic field is set to B_t = -2.5 T in order to assure measurements of the ECE diagnostic for the determination of the electron temperature (see Sec. 3.4.2). The toroidal magnetic field and the plasma current result in a safety factor q_{95} of about 6 for the default scenario. The averaged triangularity is in the medium range of $\delta_{av} \approx 0.23 - 0.24$. External heating with 3 neutral beam sources, i.e. an input power of $P_{heat} = 7.5\,\mathrm{MW}$, assures that the discharges are well above the L-H power threshold of about 3.3 MW (see Sec. 2.3).

This new dataset for the HDL studies in the full-W AUG consists of 29 successful discharges. Due to the disruption caused by L-mode density limit, only one H-L transition can be observed per shot. An exception is discharge AUG #29810, which contains 2 transitions, as shown in section 6.6.

The conducted experiments include a variation of the safety factor ($q_{95} = 3.5 - 6$), the plasma current (I_p = 0.4-1.0 MA), the external heating power (P_{heat} = 5-12.5 MW) and gas puffing rates in order to study their effect on the HDL. Chapter 6 discusses these parameter scans. Dedicated discharges with pellet fueling are reported in chapter

9. However, most of the discharges were repeated with similar parameters to optimize the fueling of the experiment and to obtain a better diagnostic coverage. A full list of all successfully conducted experiments and their main parameters can be found in the appendix.

4.2. High density operation of AUG, plasma fueling

The gas ramp for the discharges is realized by injecting deuterium gas into the vacuum vessel. The neutral gas enters the plasma, is ionized and in this way increases the plasma density. Transport plus ionization & recombination mechanisms balance the plasma electron density with the neutral gas available in the vacuum vessel. For gas puffing several gas valves are installed below the divertor and on the low field side of the torus. The location and the rate of the gas puffing is programmed by the discharge control system before the discharge.

The neutral pressure required for the HDL studies are up to 6 Pa in the divertor and 0.06 Pa in the main chamber. This is more than twice than in a standard H-mode discharge (about 2 Pa in the divertor and 0.004 Pa in the main chamber). Note that the compression of the neutral gas in the divertor relative to the main chamber is lower by a factor of 5 for the HDL discharges.

The fueling capabilities of the gas valves in the present setup of AUG are too low or the pumping capacity too high to achieve the required neutral pressures. Therefore, the overall pumping capacity of AUG was reduced from 114 m^3/s to 14 m^3/s by turning off the cryo-pump system [51]. Note, that for the standard operation with cryo-pump, the plasma density is proportional to the gas puffing rate, which determines the neutral pressure in the divertor. Without the cryo-pump, the equilibrium gas pressure is much higher and the pumping time constant is longer. The latter is defined as the time at which the neutral pressure stays constant with constant gas puffing rate. Thus, a constant gas puffing rate leads to an almost constantly increasing neutral density in the divertor (see e.g. green lines in Fig. 4.1) and consequently one might expect a steadily increasing plasma density.

A problem arising with the operation without cryo-pump is the impact of the poorly controlled wall fueling. Significant amounts of neutral gas stick to the surfaces inside the vacuum vessel after a discharge. This gas is released during the start-up of the following discharge and additionally fuels the plasma. Note, that the gas inventory on the wall is sufficient to fuel low density discharges without additional gas injection. The amount of gas fueling from the wall depends on the wall conditions and cannot be controlled directly. The pumping time constant without the cryo-pump is much higher and the wall fueling can meanwhile have a significant and non-reproducible effect on the neutral density.

The obtained high neutral and electron density restricts also several measurements. The

ionization gauges, which measure the neutral pressure, saturate. This is for example seen in figure 4.2. The left middle plot shows in black the neutral pressure measured by an ionization gauge in the divertor (F07). At a pressure of about 3-4 Pa, the gauge starts to saturate and the signal oscillates. The overlaid blue line is the scaled pressure measured in the pump chamber (F12), where the actual neutral pressure is much lower but proportional to the divertor pressure.

The high neutral pressure also attenuates the particle beam of the Li beam diagnostic (Sec. 3.4.2). Most of the accelerated atoms are ionized and thus stopped by the electrons in the SOL and the neutral gas before they reach the separatrix. Therefore, this diagnostic is not reliably working for the high density discharges and can only provide data in the SOL for two HDL discharges. Additionally, the electron temperature measurements of the ECE diagnostic are limited by the cut off density (see Sec. 3.4.2).

Alternatively, it was tried to reach the HDL with the cryo-pump in operation. Figure 4.1 compares the gas puffing rate and neutral density of three HDL discharges. Two were operated with the cryo-pump. In this case only the maximum gas puffing rate was sufficient to reach the HDL (blue lines). Without the cryo-pump (green lines), a much lower rate is necessary for the HDL. The corresponding fueling rates are listed in table 4.1. The operation without cryo-pump is preferable. The discharge parameters can be better controlled if the maximum gas puff is not needed.

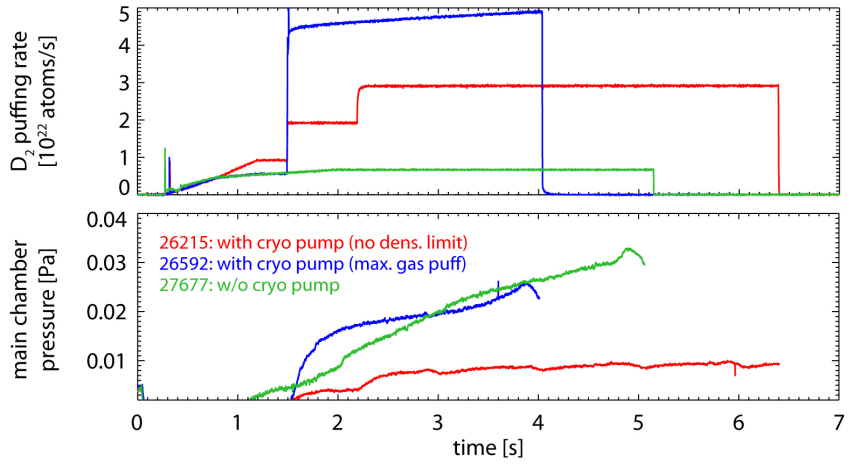

Figure 4.1.: Gas influx rate (top) and resulting main chamber pressure measured by ionization gauges (bottom) for three different HDL discharges. For discharge 26215 (red) the neutral pressure was insufficient to reach the HDL. In discharge 26592 (blue) all available gas valves were used to maximize the gas puffing rate and the (L-mode) density limit was reached at 4s. Without the cryo-pump system (green, AUG #27677), a much lower rate is necessary to reach the same neutral pressure and the H- and L-mode density limits.

	scenario	gas puffing rate $[10^{22}\,\frac{\text{atoms}}{\text{s}}]$
full-C AUG	HDL	$2.5-3$
full-W AUG	standard H-mode	$2-2.5$
	standardly available	≤ 3.0
	maximum available (all gas valves)	$5-8$
	HDL with cryo-pump	≥ 5
	HDL without cryo-pump	$0.7-1.5$

Table 4.1.: Standardly used and maximum gas puffing rates at AUG

4.3. Fueling limit

The disproportionality between the high neutral pressure and the achieved electron density in the HDL discharges is caused by the so-called fueling limit. For low densities, the plasma density is proportional to the gas puffing rate or the neutral density in the divertor, respectively. For higher densities this relation becomes non-linear and a much higher divertor pressure is needed to achieve the same increase of plasma density. The right side of figure 4.2 indicates the linear and non-linear phases.

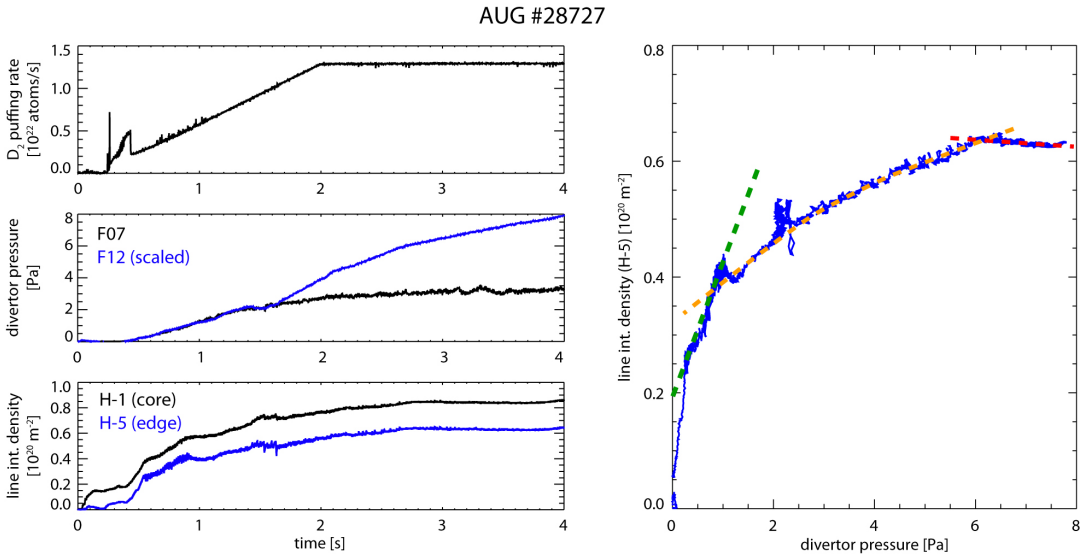

Figure 4.2.: Left: Measurements of the deuterium puffing rate, divertor neutral gas pressure (gauge F07 is saturated and overlaid by a scaled measurement of gauge F12) and line integrated electron density of AUG #28727. Right: Line integrated density plotted over the neutral pressure. The green line indicates the region where the electron density increases linearly with the neutral pressure. Approaching the fueling limit, the neutral pressure has to increase strongly for a weak increase of the plasma electron density (orange), finally, the electron density does not increase despite an increasing neutral pressure (red). However, the two phases are not always as clearly distinguished.

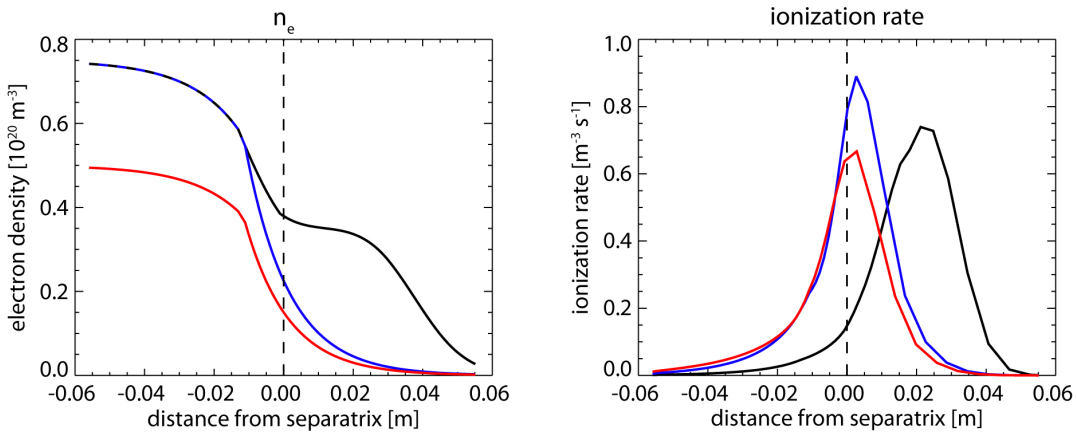

Figure 4.3.: Density profiles and the resulting ionization rate profiles calculated by the KN1D code [52]. With increasing density the ionization profile shifts outwards, reducing the effective fueling.

This fueling limit can be explained by an outward shift of the ionization profile. In figure 4.3 the ionization rate is calculated for three different electron density profiles by the KN1D code [52].

KN1D is a one-dimensional kinetic transport algorithm for neutral hydrogen and hydrogen molecules in the SOL plasma. It takes as input the density and electron and ion temperature profiles and the neutral gas pressure at the wall and calculates the five-dimensional velocity distribution function of atomic and molecular hydrogen, based on the balance of ionization, recombination and the radial and perpendicular fluxes. It assumes a slab geometry and takes into account the wall (as a source of room temperature molecules), the limiter shadow (with the connection length to the closest limiter) and the separatrix position.

The code assumes poloidal symmetry and does not account for any divertor influence. This assumption is valid if the neutral density is dominated by the recycling of the neutrals at the main chamber wall. However, two-dimensional models show that the plasma fueling is dominated by the divertor [53]. Nevertheless, KN1D calculations show the change of ionization rates and the ionization position in the main chamber, which give also an indication for the changes in the divertor.

The change from the red to the blue line shows the effect of core densities below or close to the HDL, both assuming an exponential decay from the pedestal top on. The black line is the measured density profile of an HDL discharge (AUG #28726, 2.8s).

If the electron density rises, the ionization increases in the SOL and stays constant in the confined region. Thus, the same amount of the neutrals fuel the confined plasma. Furthermore, the increased ionization in the SOL leads to a significant electron density in this region, as is observed for the HDL discharges. This has a reinforcing effect on the ionization profile, which is finally completely shifted outwards and decreases the fueling efficiency.

For the simulations in figure 4.3 a constant neutral gas pressure and constant electron temperature, i.e. changing electron pressure, were assumed. However, the same effect is visible if the pressure is kept constant or the neutral gas pressure varied. The KN1D algorithm is based on a one-dimensional flux balance and does not take into account any poloidal asymmetries. In [53] a strong poloidal variation of the fueling is reported, which cannot be reproduced by KN1D. The outer midplane fueling, as simulated by KN1D, has a non-negligible impact on the overall fueling and gives also an indication for the general behaviour at other poloidal locations. A self-consistent, two-dimensional modeling of HDL discharges by the SOLPS code package [54] was not yet successful due to instable simulations in this parameter region. Nevertheless, the results of the KN1D code indicate a strong and reinforcing effect of an increased SOL density, which might lead to the fueling limit.

The fueling limit and its possible effect on the HDL is further discussed in chapter 8.

4.4. Evolution of typical HDL discharges

Figure 4.4 shows characteristic time traces of an H-mode density limit discharge as described in the previous sections. The characteristics reported here are common to all HDL discharges, though the timing differs between the discharges, e.g. due to the conditioning of the wall.

During the discharge, the neutral gas pressure in the divertor (5th plot of Fig. 4.4) is constantly rising. Due to the fueling limit, the electron density is only weakly increasing after the discharge is fully developed (~1 s). The plasma stored energy (W_{MHD}, top plot) is monotonically decreasing. Therefore, the energy confinement decreases, since the heating power is kept constant throughout the discharge. This can also be seen in the reduction of the H-factor (bottom plot), which gives the energy confinement time with respect to the ITERH98P(y,2) scaling [55]. Fluctuations, which are most likely correlated with the detachment state [56], start to appear in a wide frequency band around 6 kHz close to the X-point and might be a sign of increased transport.

Figure 4.5 displays the evolution of the edge profiles of the electron density and temperature during the HDL discharge #28726. This is the only discharge which features a full set of profile measurements in a the time resolution of 200 ms. This discharge did not reach the L-mode or disruption but was ended by a standard ramp-down of the heating power. Figure 4.5 includes all profiles of the discharge. A subset of these profiles is reprinted in sections 5.1 - 5.4.

The density profiles are flat inside the confined region due to the high collisionality of the discharges. Only in the beginning the density profile does increase centrally, when the discharge is still building up. Later the central density does not change and a plateau with constant electron density is building up in the SOL. This plateau rises to about half of the pedestal top density and then stays roughly constant at this height.

The electron temperature profile shows in the beginning a distinct pedestal with a

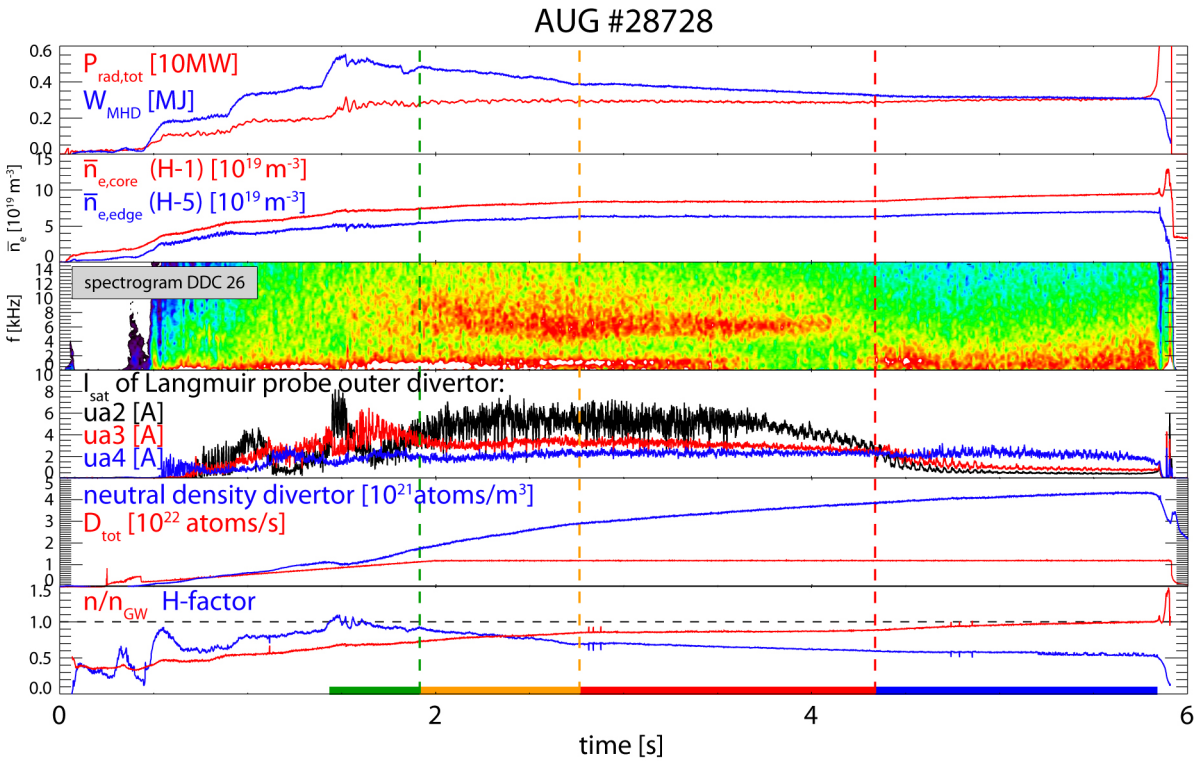

Figure 4.4.: Characteristic time traces (AUG #28728) of an HDL discharge: Plasma stored energy (W_{MHD}), total radiated power ($P_{rad,tot}$), line integrated electron density (edge *H-5*, core *H-1*), power spectrum of a diode bolometer channel observing the X-point ($DDC26$), ion saturation current in the outer lower divertor ($ua2$ below strikeline, $ua3$ around strikeline, $ua4$ above strikeline), neutral density in the lower divertor (below roof baffle), H-factor (ITERH98P(y,2) scaling) and Greenwald fraction (n/n_{GW}). The dashed lines and the bottom color bar indicate different phases of the HDL, which are further discussed in chapter 5.

pedestal top temperature of around 500 eV. The temperature is steadily decreasing throughout the discharge. In sections 5.1-5.4 the temperature evolution is shown in more detail for another discharge. First, the pedestal width of the electron temperature appears to decrease and later the pedestal gradient does decrease.

The evolution of the radial electric field (E_r) well can be seen in figure 4.6. Qualitatively, the E_r well weakens constantly. From a depth of about -35 kV/m, which is well above the H-mode threshold of -15 kV/m [8], it approaches the latter value shortly before the end of this discharge. The radial electric field is inferred from the measurements of electron density and temperature as described in section 3.4.5. The dashed lines represent poor fits and are omitted.

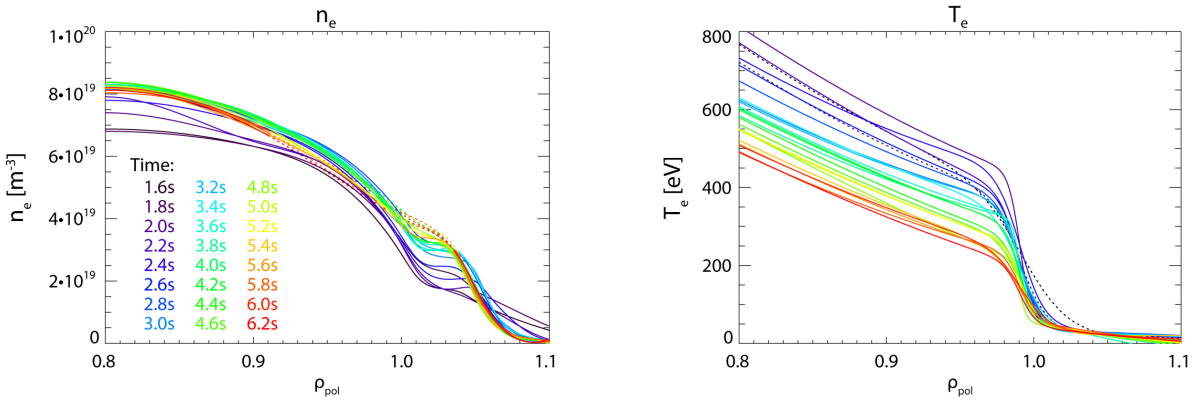

Figure 4.5.: Evolution of the electron density (left, measured by the Li beam and Thomson scattering diagnostics) and temperature profile (right, measured by the Thomson scattering diagnostics) during the HDL discharge #28726. The dashed lines indicate time points and regions without reliable data.

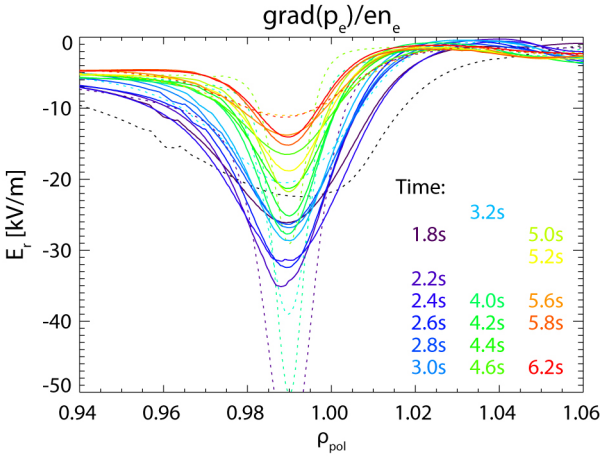

Figure 4.6.: Evolution of the radial electric field inferred by the kinetic profiles (Fig. 4.5) during the HDL discharge #28726.

5. The four phases of the H-mode density limit

The temporal evolution of the stored energy and the line integrated density exhibit four different phases as indicated by the background colors in Fig. 5.1. These phases are differentiated in the time derivative of density and stored energy and have for example an impact on the ELM behaviour or the divertor detachment. They become evident when the stored energy is plotted versus the edge line integrated density:

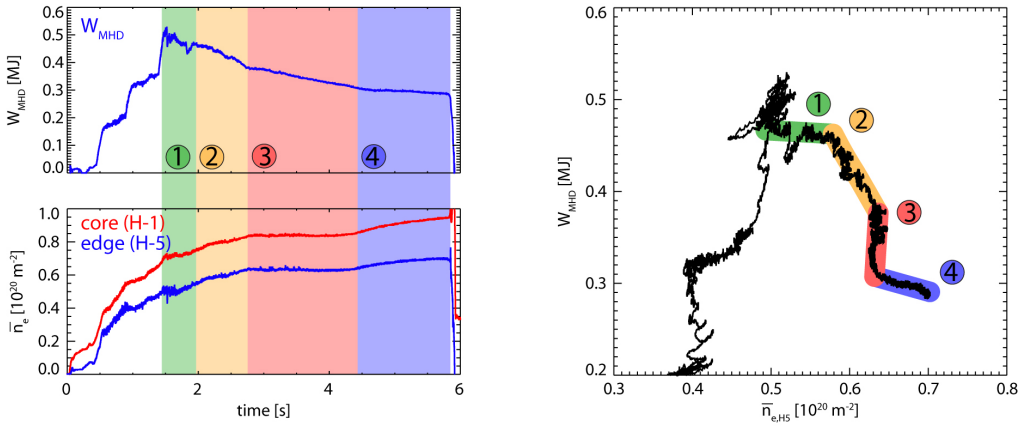

Figure 5.1.: Left: Time traces of stored energy and line integrated density of AUG #28728. Right: Stored energy plotted versus the edge line integrated density. The four distinct phases are highlighted by the same color coding as in Fig. 4.4.

The phases are characterized as 1 stable H-mode, 2 degrading H-mode, 3 breakdown of the H-mode and 4 L-mode. These phases appear in all analyzed HDL discharges. The duration of the phases varies strongly within the presented database.

The phases can also be distinguished by the pedestal top temperature. Figure 5.2 shows the same graphs as figure 5.1 for discharge #26902. Additionally, an estimate of the pedestal top temperature using the ECE measurements is plotted versus time and versus density.

The pedestal top temperature is a local measurement, in contrast to the global parameter of stored energy, which is the volume integral of the plasma pressure. As shown, both values are closely correlated. Notably, the isobaric line turns from a reciprocal function in the plot of the pedestal temperature to a horizontal line in the plot of the stored energy, as seen for the first phase in figure 5.2.

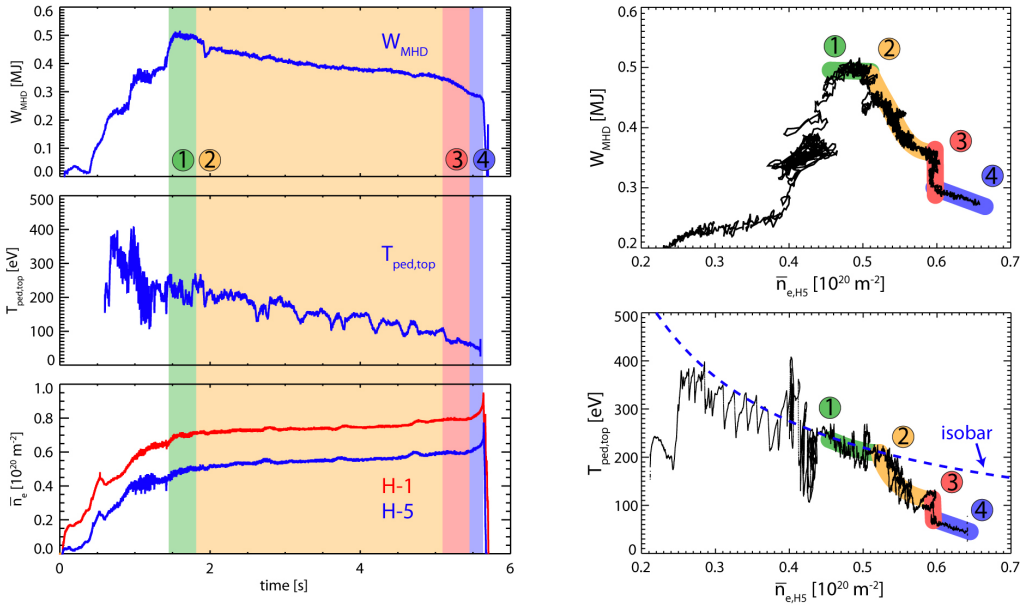

Figure 5.2.: Left: Time traces of stored energy, estimated pedestal top electron temperature (at $\rho_{pol} = 0.985$) and line integrated density of AUG #26902. Right: Stored energy (top) and estimated pedestal top temperature (bottom) plotted versus the edge line integrated density. The four phases are visible in both plots. The blue dashed line on the bottom is an isobaric line, indicating that the pedestal pressure stays about constant up to an edge density of $5.2 \cdot 10^{19}\mathrm{m}^{-2}$. The periodic variations are mainly caused by ELMs.

The observation of the four phases give a guidance to analyze the HDL in close detail. A detailed characterization of the phases, including the evolution of the kinetic profiles and further empirical observations, will be given in sections 5.1-5.4. However, the four phases are briefly discussed in order to provide an overview:

1 During the stable H-mode phase, the stored energy and the confinement stay constant, while the density is increasing in the core. The temperature decreases inversely to the density. The relationship between n_e and T_e evolves along an isobaric line towards higher densities (indicated in Fig. 5.2). This phase is called a stable H-mode, since the pressure, and thus, the confinement, stays constant while the density increases.

2 During the degrading H-mode phase, the density increases marginally and the stored energy decreases. In figure 5.2 this is seen as a movement away from the isobaric line towards lower pressure, leading to a knee in the graph. The temperature pedestal width appears to decrease, leading to reduction of the pedestal top and core temperature. This reduces the confinement and stored energy. The duration of this phase varies between the discharges in the database from 0.5 s to over 3 s.

3 The breakdown phase of the H-mode is characterized by a sharp drop of the stored energy at a constant density. The temperature pedestal vanishes, i.e. the pedestal gradient reduces, and the ELMs disappear. This phase is determined as the breakdown of

the H-mode and its density interpreted as the actual H-mode density limit. The start of this phase is used later on for several scalings of the density limit (see chapter 6). The duration of this phase varies between 0.1 s and 4 s within this set of discharges.

4 In the L-mode phase, the line averaged density increases again and the stored energy decreases only slightly. The pressure is almost constant, the temperature decreases accordingly. The abrupt change of the discharge behaviour (i.e. sharp bend in the graph) infers again a transition between two distinct plasma regimes, concluding that the transition from H- to L-mode is completed.

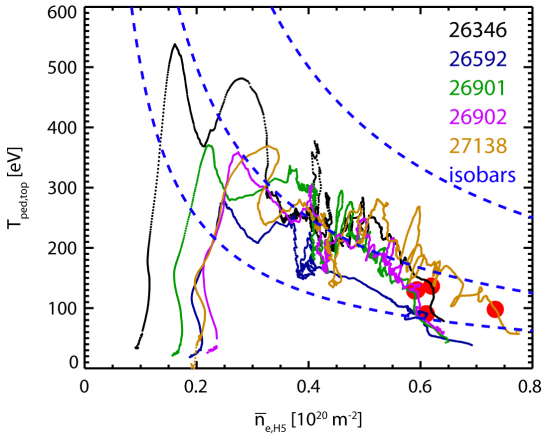

Figure 5.3.: Pedestal top temperature versus edge line integrated density for several HDL discharges. All discharges exhibit the four phases. The drop of confinement (back transition from H- to L-mode) resembles an almost vertical line. The start of this phase is indicated by a red dot for the trajectory of each discharge.

The phases are reproduced in every HDL discharge. However, in some discharges the first phase was exhibited during the ramp up or the discharge was intentionally ended before the fourth phase was reached. In figure 5.3 the pedestal top temperature is plotted versus the edge line integrated density for several discharges. Additionally, figure 5.4 illustrates the four phases in the graph of stored energy versus the density. Here, six HDL discharges at different experimental parameters are shown. For both figures, the shape of the graphs is similar for the discharges. However, the individual phases take place at varying densities, temperatures and stored energies, depending on the discharge parameters. These scalings of the HDL are analyzed in detail in chapter 6.

We conclude that each phase is a quasi-stable plasma regime. The transition between two phases always resembles a sharp bend in the graph of stored energy versus density, clearly distinguishing the phases.

We highlight additionally the finding that each of the phases recovers after trips and modulations of the heating power, as seen in figure 5.4. The stored energy drops with a reduction of the heating power but the plasma stays in a similar regime. When the full

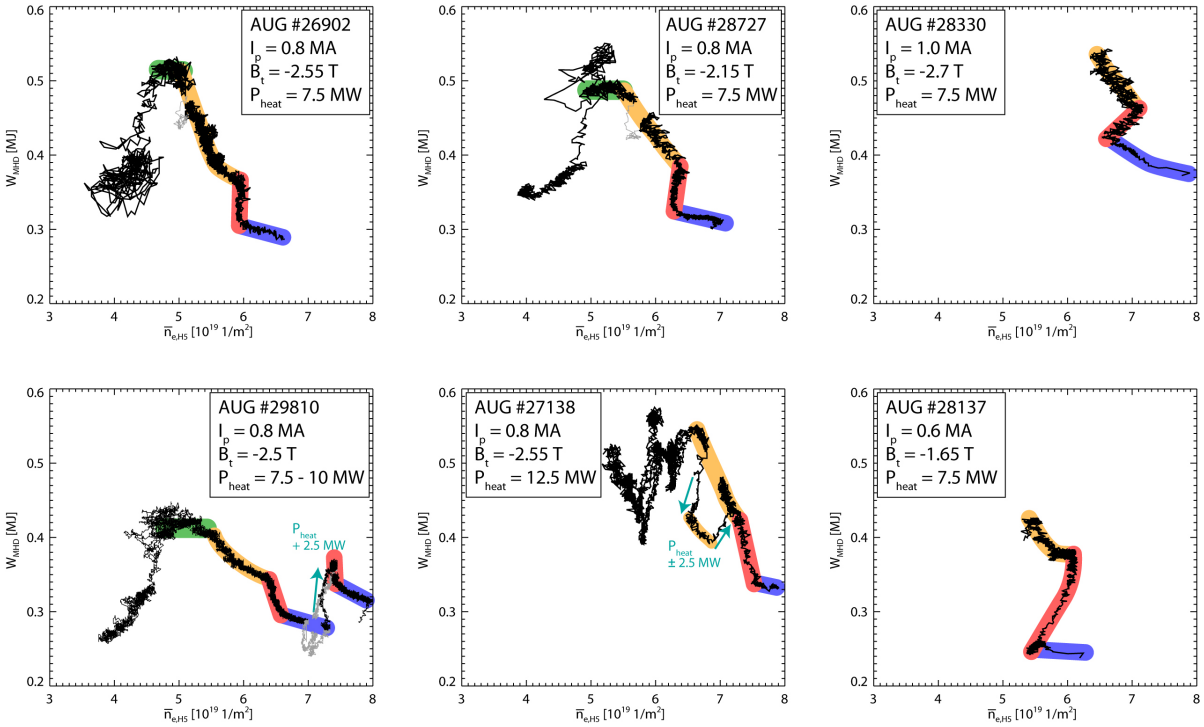

Figure 5.4.: Stored energy versus edge line integrated density for several HDL discharges. Outliers due to trips of a neutral beam source are indicated in grey. Discharge AUG #29810 includes a step in heating power and discharge AUG #27138 a modulation of the heating power. The four phases appear independent of the main discharge parameters.

heating power is restored again, the plasma goes back into the initial phase.

Furthermore, it is demonstrated (AUG #29810, bottom left of Fig. 5.4) that the third phase can be accessed directly. The H-mode does not need to be fully recovered beforehand. This confirms that the phases are discrete, quasi-stable plasma regimes.

Observations of the four phases in full-C AUG

The observations of the four phases is not specific for the operation with tungsten walls. Figure 5.5 shows the plots of stored energy over density for discharges, where the first wall material of AUG was carbon. Also here the phases are identified and they have almost the same characteristics. The degrading H-mode and the following H-mode breakdown are well reproduced, indicating the same interaction between the confinement degradation and the density evolution for full-C AUG as for full-W AUG.

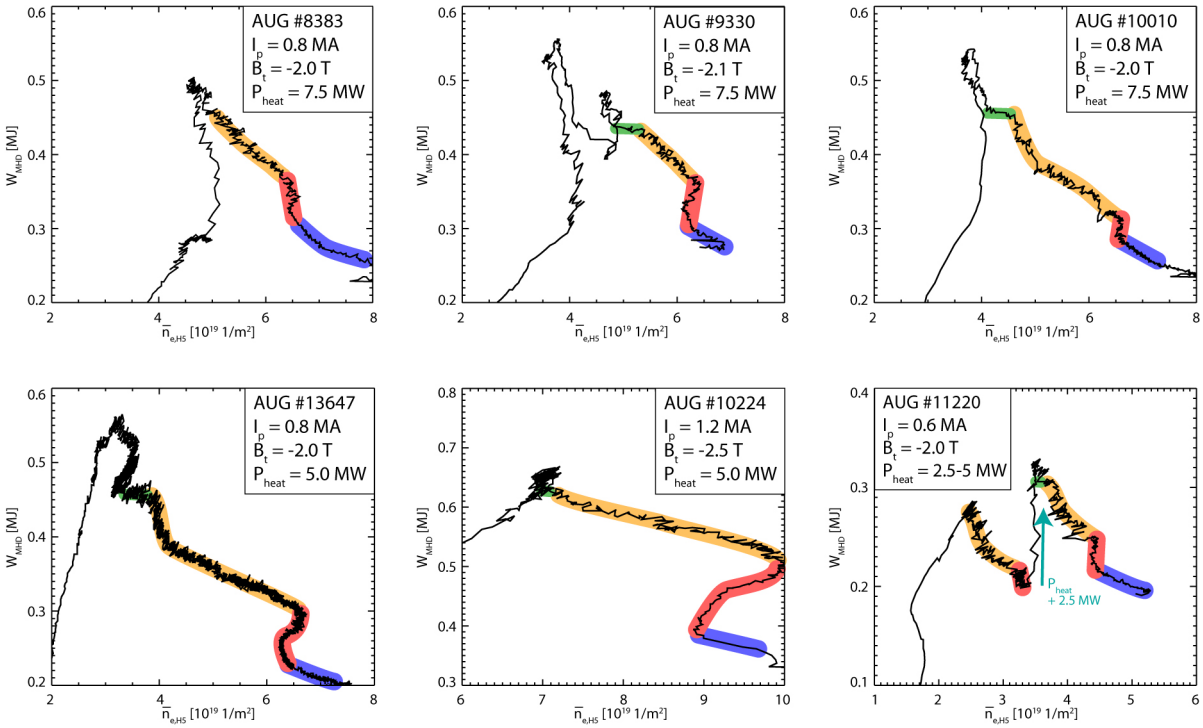

Figure 5.5.: Stored energy versus edge line integrated density from HDL discharges of full-C AUG. The same phases are identified, though the first phase might not be visible due to the discharge setup.

5.1. Stable H-mode

The first phase is characterized by a constant pressure and confinement while the density increases. Depending on the discharge, this phase might only occur during the ramp up of the heating power, thus it is not always recognized.

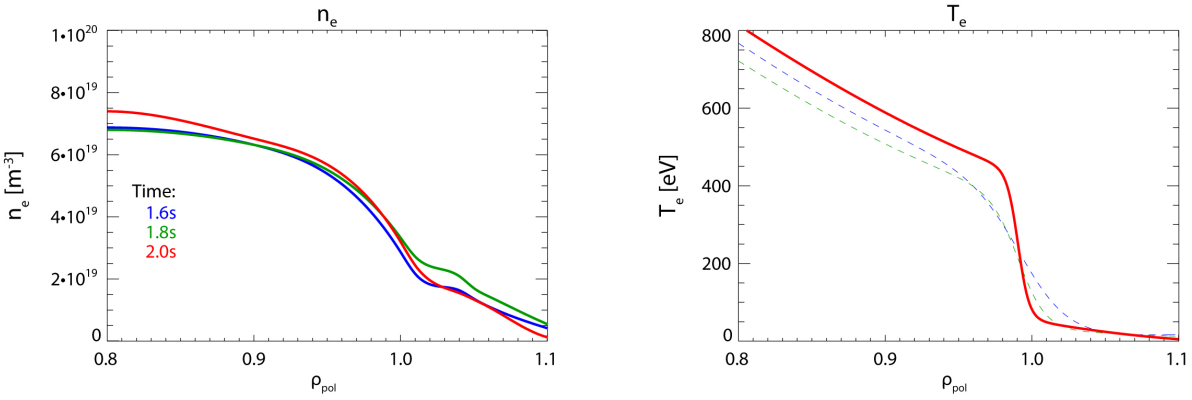

Figure 5.6.: Electron density and temperature profile during the stable H-mode phase of the HDL discharge #28726.

The temperature profile (right hand side of Fig. 5.6) shows a distinct pedestal. To keep the pressure profile constant, the temperature decreases slightly. The H-factor, which is a measure of the energy confinement time with respect to the ITERH98P(y,2) scaling [55], is between 0.9-1.05 for this phase, as expected for a regular H-mode. Since the density can still increase while the stored energy is constant (apart from ELM losses), this phase is considered to be a stable H-mode. Eventually, the fueling limit (see Sec. 4.2) is approached due to the increase of neutral density.

5.1.1. Transition from type-I to type-III ELMs

During the first phase the transition between type-I ELMs and type-III ELMs takes place. This is expected for high densities and reported for example in [57]. In figure 5.7 it is seen that the increasing density first causes the frequency of the type-I ELMs to increase and then type-III ELMs start to appear. Subsequently, the type-I ELMs become less frequent while the type-III ELMs become more frequent.

The two ELM types are distinguished by magnetic precursors, but this analysis was prohibited by high noise on the magnetic signals of the HDL discharges. Furthermore, the two ELM types can be distinguished by the dependence of the ELM frequency on the heating power, i.e. the power flux across the separatrix. The type-I ELM frequency increases and the type-III ELM frequency decreases with higher power [58].

Figure 5.7 illustrates an HDL discharge which includes a heating power modulation in order to determine the ELM types. Two different types can easily be distinguished by the measurements of the diode bolometers in the divertor. The bigger, longer lasting peaks,

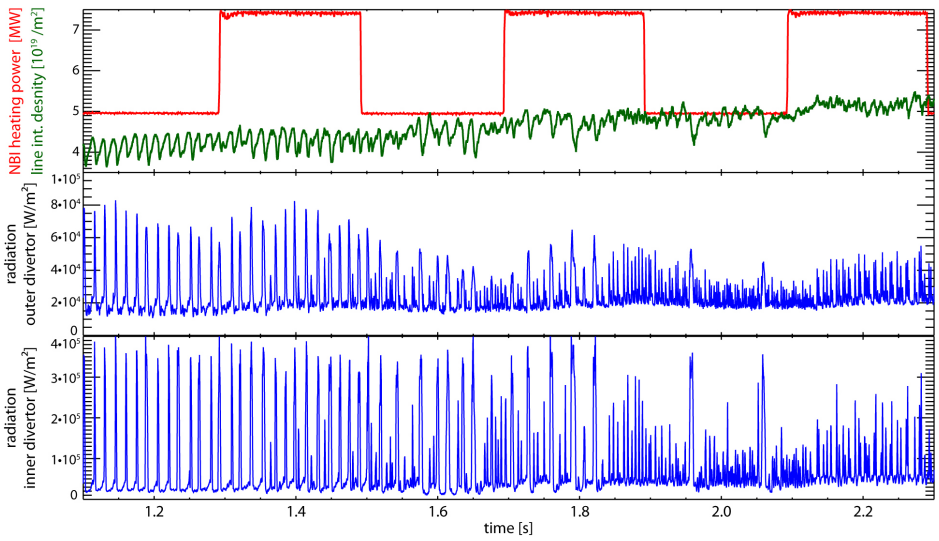

Figure 5.7.: Time traces of heating power, density and radiation at the inner and outer divertor (measured by AXUV diode bolometers) during the transition from type-I to type-III ELMs of a dedicated shot for the ELM type determination (AUG #27136).

which slowly vanish, are determined as type-I ELMs and the smaller, more frequent peaks as type-III ELMs.

5.1.2. X-point fluctuations

During the first phase, fluctuations appear in the X-point region in a broad frequency band around 6 ± 2 kHz. Their filamentary radiation is measured by the diode bolometry channels observing the X-point and is visible in the spectrogram of the signals (e.g. third plot in figure 4.4). In figure 5.8 the spectrogram and raw signal of the fluctuations of one AXUV channel is shown for HDL discharge #26902.

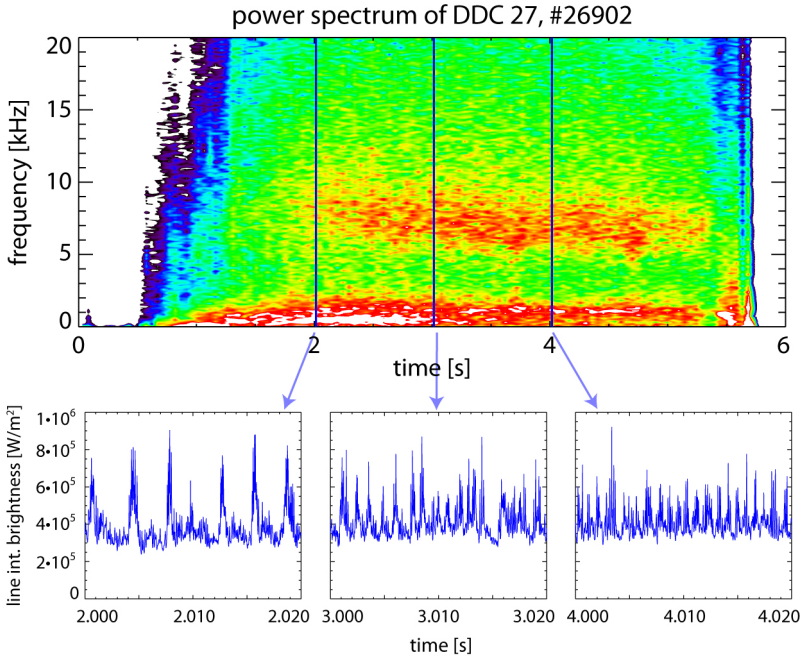

Figure 5.8.: Power spectrogram of diode bolometry channel DDC 27, observing the X-point region. The fluctuations are clearly seen in a wide frequency band around 6 kHz. The bottom plots show the evolution of the fluctuations in the diode signal. They are small filamentary peaks on top of the ELM modulation of the radiation. While the ELMs become more frequent and thus smaller, the fluctuations appear to be unchanged.

The diode bolometry is so far the only diagnostic at AUG which can measure these fluctuations. No other diagnostic has a sufficient time resolution in that region. The fluctuations are only observed around the X-point, however, a poloidal movement of the filaments can be tracked, taking advantage of the high spatial resolution of the diode bolometry. The latter analysis is presented in appendix D.

Though these fluctuations are a sign of increased transport in the SOL, they are not specific for the H-mode and therefore not a symptom of the HDL. They were first discovered

in the HDL discharges but are also observed in high density L-modes [47, 56].
In [56] (see Fig. 5.9) the occurrence of the fluctuations in L-mode is reported to correlate with the detachment state of the divertor. They are observed when the inner divertor is detached and the outer divertor is still attached. This is in line with the observations in the HDL discharges, since the fluctuations disappear as soon as the outer divertor detaches in the L-mode phase. However, in the HDL discharges, the fluctuations set in gradually, whereas they have a sudden onset in the L-mode studies (see Fig. 5.9).

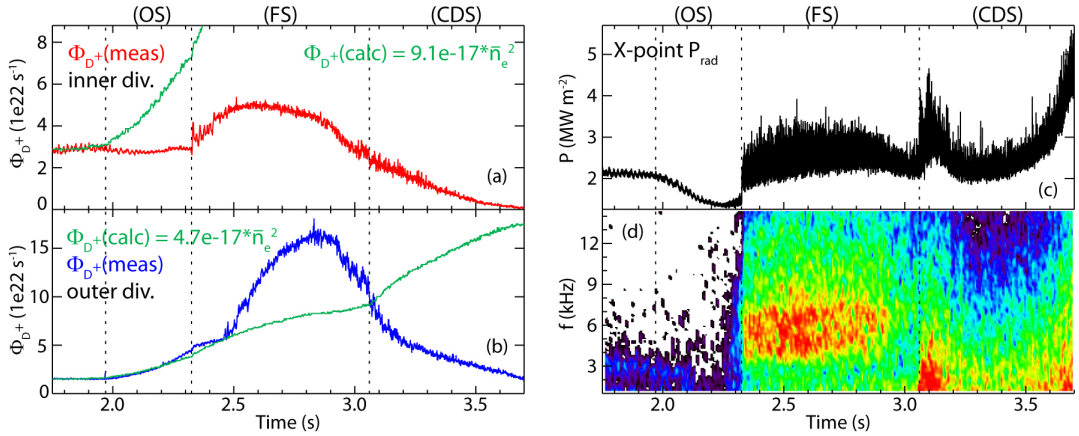

Figure 5.9.: Observation of the X-point fluctuations (d) in L-mode correlated with different detachment states: onset state (OS), fluctuating state (FS) and complete detachment state (CDS). The left hand side shows ion fluxes to the divertor in order to characterize the detachment. The right hand side shows the signal and the spectrogram of AXUV channel DDC 28. Picture adapted from [56].

The gradual onset of the fluctuations in the HDL discharges can be explained by the evolution of the detachment of the inner divertor. This first develops in between ELMs, while ELMs still re-attach the divertor due to their additional power flux. With increasing density and smaller ELMs the inner divertor is permanently detached. In this way, the fluctuations first appear in between ELMs and later on are permanently present.
The nature of these fluctuations remains so far unclear. Their radiative behaviour and location are known. In [59] a critical temperature in the divertor is reported to be necessary for the appearance of the fluctuations. Whether this filamentary radiation is caused by density or temperature fluctuations or by impurities cannot be determined with existing measurements. However, possible candidates are small, unstable MARFEs or shock fronts in the divertor.

5.2. Degrading H-mode

In the degrading H-mode phase the confinement decreases gradually. The duration of this phase varies between 0.8 s and 3.3 s.

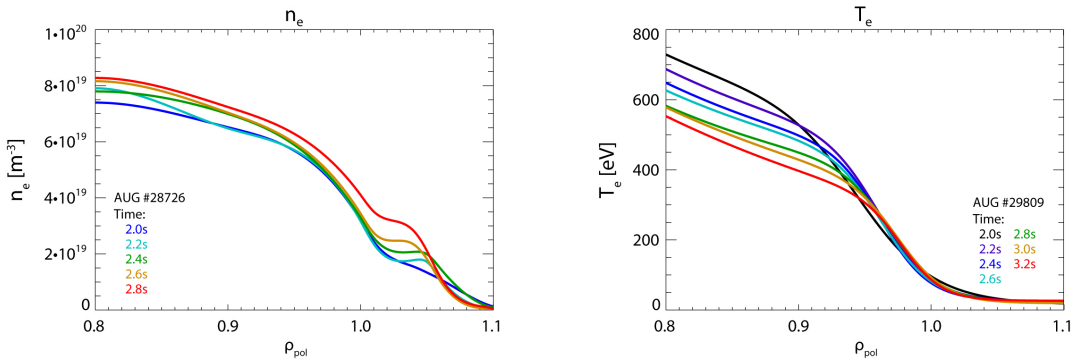

Figure 5.10.: Electron density and temperature profile during the degrading H-mode phase.

This phase is still an H-mode, since ELMs are present and the temperature profile exhibits a clear pedestal. The X-point fluctuations are ongoing.

During the second phase the line averaged density still rises, although the core electron density only marginally increases. A plateau of electron density builds up in the SOL, which is rising to about half the pedestal top density. In figure 5.12 it is seen that this plateau extends from the separatrix to the limiter shadow. The temperature pedestal width appears to decrease and thus, the pedestal top temperature declines.

In contrast to the first phase, the plasma stored energy is reducing despite a constant heating power and thus, the confinement is degrading. The reduction of the stored energy sets in abruptly. Either the existing energy transport suddenly increases or an additional energy loss channel comes up at this point. However, this effect appears to be coupled to the density increase, which in this phase occurs predominantly in the SOL. In chapter 8, two mechanisms are proposed that can lead to this increased energy loss at high densities.

5.3. Breakdown of the H-mode

The third phase is marked by the sudden stop of the increase of the line averaged density. Also the time derivative of the stored energy changes. In the plot of stored energy versus edge density this phase resembles a vertical line. It has a duration between 0.1 s and 3.5 s.

During this phase the ELMs, finally vanish. This is seen by the disappearance of the low frequency band (50-1000 Hz) in the spectrogram of figure 4.4 at about 3.7 s. Also the X-point fluctuations disappear at the end of this phase.

The steep temperature gradient in the pedestal is eroded in this phase. Notably, the line averaged density as well as the whole density profile stay almost constant. The density plateau in the SOL stays fixed slightly below half of the pedestal top density.

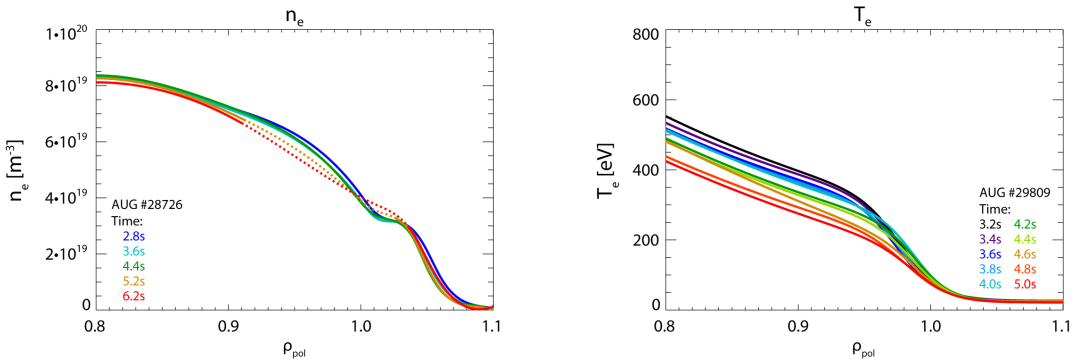

Figure 5.11.: Electron density and temperature profile during the H-mode breakdown phase.

In figure 5.12 all measurements of the edge electron density during the third phase are shown. The plateau is directly measured by the Li beam diagnostic. The Thomson scattering diagnostic also exhibits a scatter below the Li beam data. The difference between the two diagnostics is explained by the different measurement principles. The Thomson scattering diagnostic measures the average in the time the probing lasers are launched into the plasma ($\delta t \approx 10\,\mathrm{ns}$) and the Li beam diagnostic averages over the camera exposure time ($\delta t \approx 1\,\mathrm{ms}$). Therefore, the Thomson scattering diagnostic can measure single density blobs and holes in the SOL while the Li beam averages over them. Nevertheless, this would not explain that there are only few scattered points of the Thomson scattering above the Li beam measurements. The difference might also result from the large noise of the Thomson scattering data. Probe measurements in the SOL indicate that the density plateau consists of a background density and additional fluctuations. Which of these two components dominates cannot be determined from existing measurements.

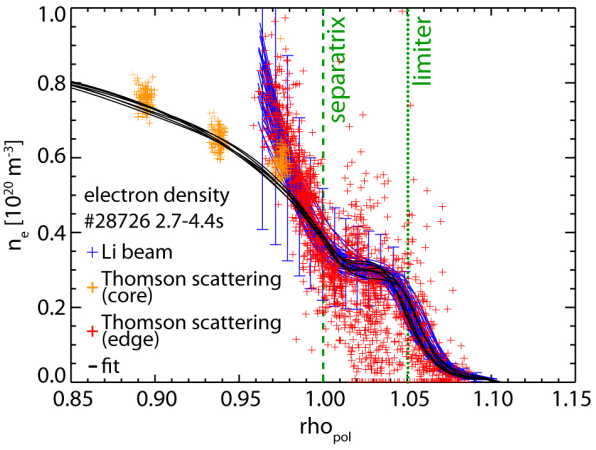

Figure 5.12.: Electron density measurements in the third phase. The density does not change and exhibits a plateau in the SOL. The green lines indicate the separatrix (dashed) and limiter (dotted) position.

In figure 5.13 one can see that the E_r well, which is a main player for the turbulence suppression in H-mode, is weakening drastically during this phase. From an E_r well depth of about -25 kV/m it reduces to a value of -15 kV/m, which is the reported threshold for the L- to H-mode transition under similar conditions at AUG [8].

Due to the existence of ELMs and the pronounced E_r well, the whole phase is identified

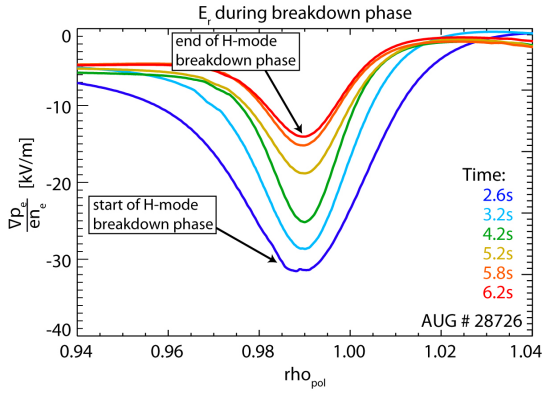

Figure 5.13.: Evolution of the radial electric field during the third phase of AUG #28726 evaluated from the kinetic measurements. The depth of the pronounced E_r well is at typical H-mode values.

as an H-mode. Since the ELMs vanish and the E_r well weakens towards the end of the phase, it resembles the back transition into the L-mode. In most cases a clear transition between the breakdown of the H-mode and the L-mode phase is seen, attesting to a change of the regime. However, in some cases the transition is smooth and H- and L-mode cannot be fully distinguished. It is also reported [15, 60], that the bifurcative behaviour between L- and H-mode disappears at high densities.

This phase is defined as the actual H-mode density limit, though it is only one part of the sequence which causes the HDL. However, this phase reveals the maximum achievable density in H-mode. The latter identification is also motivated by the constant density during this phase. The beginning of this phase is used in section 6 to study the dependencies of the HDL on various plasma parameters.

5.4. L-mode

With the beginning of the fourth phase, the density increases again. Meanwhile, the stored energy stays roughly constant. The H-factor is around 0.5-0.6, which is a typical value for L-mode confinement. Figure 5.14 shows that the temperature profile does not exhibit a significant pedestal any more and decreases slightly with increasing density. Unfortunately, there are no density profile measurements of sufficient quality available for this phase.

The L-mode phase is not actually directly a part of the HDL, however, it is important for a complete picture of the HDL discharges. Additionally, it shows that the transition from H- to L-mode is completed. The reappearing density increase reveals that the effect, which is causing the saturation of the density, is specific to the H-mode.

The measurements of the ion saturation current by the Langmuir probes in the outer divertor can be seen in figure 5.15. During the first three phases the probes experience an increase of the signal, indicating that the divertor is in the high recycling regime.

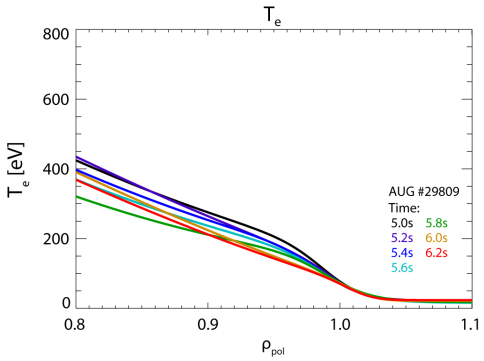

Figure 5.14.: Temperature profiles during the L-mode phase.

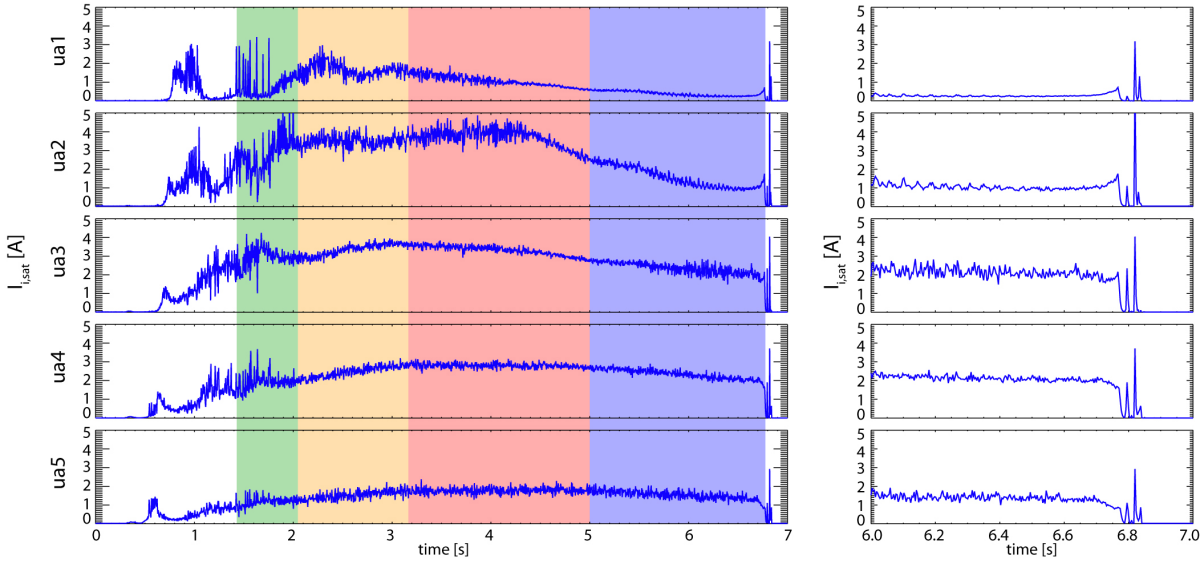

Figure 5.15.: Left: Ion saturation current measurements of discharge #29809 in the outer divertor (position of the probes is shown in Fig. 3.19). The background colors indicate the different phases as above. During the third and fourth phase the divertor goes into a partially detached state, full detachment is achieved shortly before the disruption. Right: Zoom of the same signals in the final phase of the discharge.

During the breakdown of the H-mode and the beginning of the L-mode the signals decrease slightly. The outer divertor goes into a partially detached state, i.e. the plasma is detached at the location of probe *ua*1.

During this phase, a MARFE (see Sec. 7.3) is developing in the X-point region. Figure 5.16 shows the evolution of the MARFE, which starts with a strongly fluctuating radiation localized around the X-point. These fluctuations can clearly be distinguished from the X-point fluctuations, which are present during the first three phases.

Figure 5.17 shows the MARFE radiation at the X-point and its movement upwards on the high field side seen by the AXUV diodes. When the MARFE starts to move

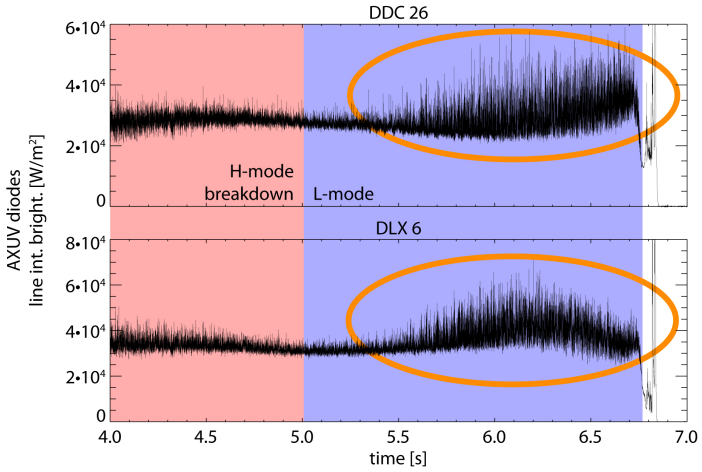

Figure 5.16.: Evolution of the MARFE seen by the AXUV diodes in the X-point region (DDC 26: vertical LOS; DLX 6: horizontal LOS) at discharge #29809. The MARFE development is characterized by strongly fluctuating radiation (orange circles). Finally, the MARFE becomes stable, moves upwards and initiates a disruption.

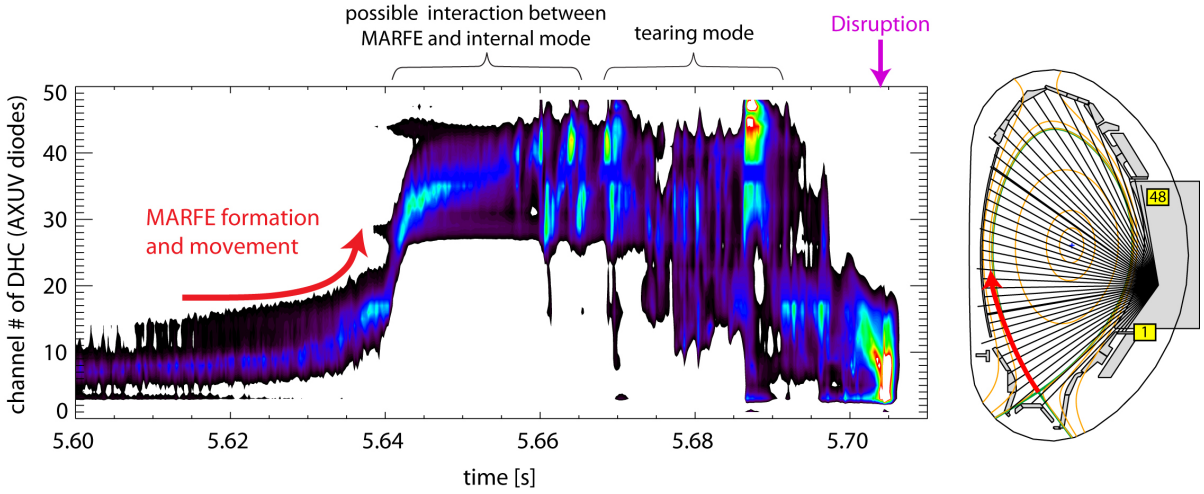

Figure 5.17.: Left: Development of a MARFE around the X-point and its upwards movement as measured by the DHC camera of the AXUV bolometry in discharge #26902 (contour plot of the measured radiation). Finally, the MARFE is initiating a disruption. Right: Position and channel number of the DHC camera and direction of the MARFE movement.

upwards, the outer divertor detaches completely (see Fig. 5.15). The movement of the MARFE coincides with the onset of an internal 2-1 tearing mode, which finally leads to the disruption. In [61] it is shown that it is possible to delay or even avoid the disruption by stabilizing the NTM by means of ECRH heating and current drive. However, this is only used to avoid the disruption and ramp down the discharge safely. The operational space cannot be extended by this measure.

5.5. Summary of the four phases

Four discrete quasi-stable plasma regimes were identified on the approach to the HDL. These phases are distinguished by their impact on the density and stored energy. The phases are classified as a stable H-mode, where the confinement is constant and the density can increase, a degrading H-mode, where the confinement deteriorates with increasing density, the breakdown of the H-mode, where the density is fixed while the edge transport barrier vanishes, and the L-mode, where the density increases again at a low, but constant, confinement.

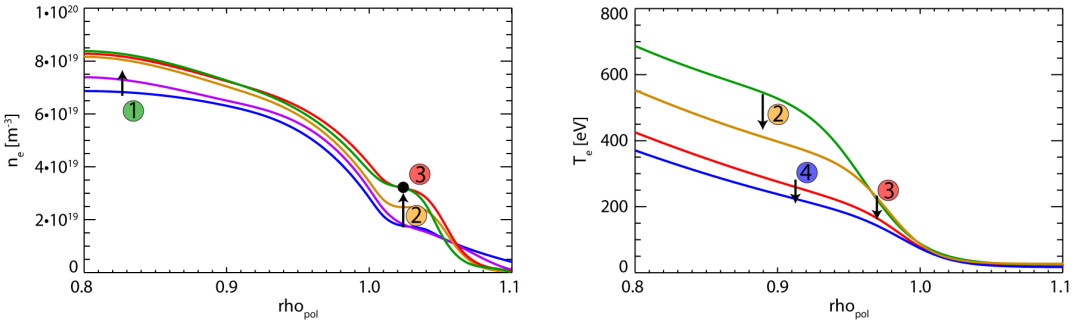

Figure 5.18.: Evolution of electron density (left, AUG #28726) and temperature profiles (right, AUG #29809). The profiles cannot be provided for all phases. The arrows and numbers indicate the radial position and the phase in which the predominant changes in the profiles occur.

The density and temperature evolution is influenced by these phases.

- In the first phase, the density increases in the center.
- During the second phase the central density appears to be fixed and a plateau of electron density is forming and increasing in the SOL. Meanwhile the temperature pedestal width decreases and lowers the pedestal top temperature.
- In the third phase, the overall density profile does not change and the temperature pedestal is eroded.
- In the last phase the line integrated density does increase again and the temperature decreases slightly.

The observation of the phases reveals, that an additional or increased energy loss channel must be present, which is seen in the decrease of stored energy in the second and third phase. This loss channel erodes the electron temperature gradient and the E_r well. Thus, the pedestal is deteriorated until the L-mode is reached. Along with this energy degradation the fueling of the plasma does change. In particular, the density increase is interrupted at the HDL until the pedestal is fully eroded. Both effects, the additional loss channel and the change of the plasma fueling, appear to be coupled to each other and their combination creates the four quasi-stable plasma regimes. In chapter 8, we will try to identify the underlying mechanisms explaining simultaneously the energy loss channel and the changed fueling characteristic.

6. Scaling of the HDL

The observations presented in the previous chapter show that the maximum H-mode density is reached in the beginning of the third phase, the breakdown of the H-mode. Since the whole electron density profile is constant during this phase, it indicates a threshold which cannot be exceeded in H-mode. Thus, this point is defined as the HDL.

The confinement reduction starts with the second phase, the degrading H-mode. Hence, it might not be reasonable to operate a future device at the HDL to achieve the highest fusion power. However, the dependencies of the HDL on various plasma parameters, such as heating power and plasma current, might reveal some of the underlying physical mechanisms of the HDL. Therefore, the HDL discharges of full-W AUG include various parameter scans, which are discussed here.

Local densities cannot be used for the scaling due to the lack of density profile measurements for all discharges. However, the interferometry measurements can be utilized. Whether the line integrated ($\overline{n}_e$) or line averaged ($\langle n_e \rangle$) measurements of the interferometry at the edge (H-5) or core (H-1) are used for the scaling is found to be of no significant importance. In figure 6.1 the linear dependence between edge and core measurements are shown. The difference of line averaged or line integrated measurements is determined by the path length through the confined plasma and is almost constant for all of the discharges. Furthermore, the similarity between the line averaged measurements using the edge channel and the core channel points out that the density profiles are flat in the core. Thus, for the HDL one can derive the linear correlations between the line

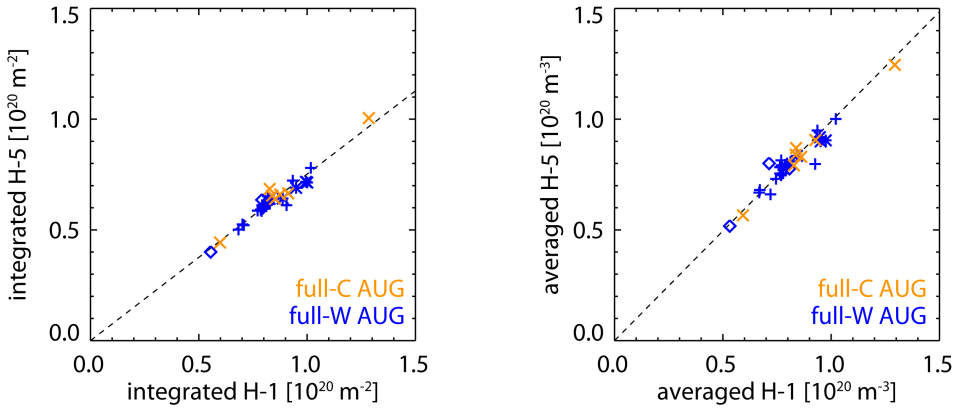

Figure 6.1.: Comparison between edge and core measurements of the interferometry, line integrated (left) and line averaged (right), at the time of the HDL.

averaged and line integrated measurements

$$\overline{n}_{e,H-1} = 1.03\,\mathrm{m} \cdot \langle n_{e,H-1} \rangle \tag{6.1}$$
$$\overline{n}_{e,H-5} = 0.78\,\mathrm{m} \cdot \langle n_{e,H-5} \rangle \tag{6.2}$$

and between the edge and core measurements

$$\overline{n}_{e,H-1} = 1.33 \cdot \overline{n}_{e,H-5} \tag{6.3}$$
$$\langle n_{e,H-1} \rangle = 1.01 \cdot \langle n_{e,H-5} \rangle\,. \tag{6.4}$$

Unless otherwise noted, the edge line integrated density $\overline{n}_{e,H-5}$ is used for the following scalings. The other interferometry measurements can be calculated with the formulas above.

6.1. Comparison to existing scalings

6.1.1. Greenwald scaling

The Greenwald limit, which was introduced in section 2.2, is observed to give an upper bound for the HDL. The Greenwald density scaling is dependent on the plasma current and the minor radius of the plasma and gives a limit for the **central line averaged density**:

$$\langle n_{e,H-1} \rangle \leq n_{GW} = \frac{I_p}{\pi a^2} \quad \left[10^{20}\mathrm{m}^{-3},\ \mathrm{MA},\ \mathrm{m}\right] \tag{6.5}$$

Figure 6.2 shows, that the Greenwald scaling indeed yields the right order of magnitude and an upper limit for the HDL. However, for higher currents the scaling differs signif-

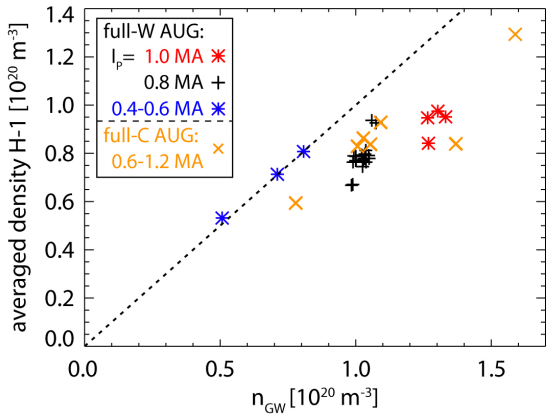

Figure 6.2.: Central line averaged electron density (H-1) of the HDL of full-W AUG and some selected HDL of full-C AUG versus the Greenwald scaling.

icantly. Similar observations can be made for the discharges with carbon walls (orange crosses). The current dependency of the HDL will be further analyzed in section 6.3.

6.1.2. Empirical HDL scaling of full-C AUG and JET-C

An empirical scaling from measurements at full-C AUG and JET-C was introduced in section 2.3 and is repeated here for convenience:

$$n_{HDL} = 48.2 \frac{q_{\perp}^{0.049\pm0.041} B_t^{0.57\pm0.08} \delta_{av}^{0.11\pm0.11}}{q_{95}^{0.86\pm0.08} R^{1.07\pm0.20}} \quad [18] \tag{6.6}$$

The given density n_{HDL} is the electron density of the pedestal top, which is in [18] identified with the **edge line averaged density**. In figure 6.3 it is observed that this empirical scaling gives also a good estimate of the HDL density in the full-W AUG.

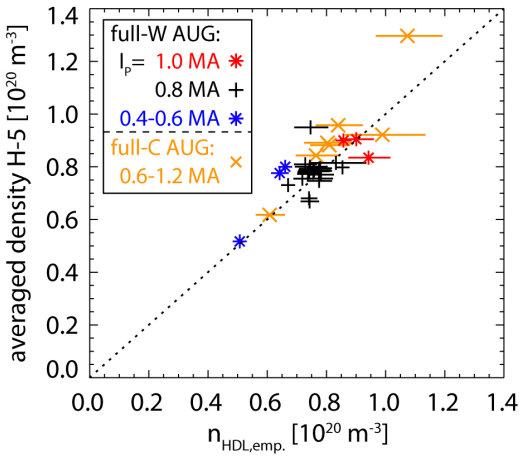

Figure 6.3.: Edge line averaged density (H-5) of the HDL of full-W AUG (black, red, blue) and some selected HDL of full-C AUG (orange) versus the empirical scaling.

6.2. Regression analysis

With the presented full-W AUG database, a regression of the **edge line averaged density** ($\overline{n}_{e,H5,regr.}$ in $10^{20}\mathrm{m}^{-3}$) is made in order to derive a power law including variations of the

- heating power ($6\,\mathrm{MW} \leq P_{heat} \leq 12.5\,\mathrm{MW}$),
- safety factor ($3.5 \leq q_{95} \leq 6$),
- plasma current ($0.6\,\mathrm{MA} \leq I_p \leq 1.0\,\mathrm{MA}$),
- toroidal magnetic field ($1.45\,\mathrm{T} \leq B_t \leq 2.7\,\mathrm{T}$) and
- triangularity ($0.23 \leq \delta \leq 0.37$).

Table 6.1 compares the empirical scaling of the carbon data (Eq. 6.6) with the actual full-W AUG dataset. Therefore, the power flux density over the separatrix $q_\perp$ is replaced by the heating power. This does not take into account the separatrix surface or the radiated power inside the confined plasma. The first is not changed within the database and the latter cannot be determined accurately enough. The major radius dependence is neglected since the actual database does not include any size variation.

$$\overline{n}_{e,H5,regr.} = C_0 \cdot P_{heat}^{A}\ B_t^{B}\ q_{95}^{C}\ \delta^{D} \tag{6.7}$$

	C_0	A ($q_\perp/P_{heat}$)	B (B_t)	C (q_{95})	D (δ)	σ
full-C AUG & JET-C [18]	~ 29	0.049 $\pm$0.041	0.57 $\pm$0.08	$-$0.86 $\pm$0.08	0.11 $\pm$0.11	0.053
full-W AUG	0.425 $\pm$0.229	0.487 $\pm$0.17	0.202 $\pm$0.17	$-$0.504 $\pm$0.16	$-$0.046 $\pm$0.26	0.030

Table 6.1.: Comparison of the regression of the full-C AUG and JET-C [18] with the regression of the actual dataset and the resulting deviation (relative RMSE).

The two datasets deviate significantly in the power dependence. The dependencies on the magnetic field and the safety factor scaling are weaker for the full-W data. To clarify these differences, the individual dependencies will be further discussed in the following sections and compared with data from full-C AUG.

The dependence on the triangularity is negligible, thus, the regression is reduced to P_{heat}, q_{95}, I_p and B_t. The latter three are linearly dependent by $q_{95} \propto \frac{B_t}{I_p}$, therefore, only two of these three parameters are used for the regression. Regressions with the three remaining, equivalent combinations of parameters are given in table 6.2.

$$\overline{n}_{e,H5,regr.} = C_0 \cdot P_{heat}^{A}\ q_{95}^{B}\ I_p^{C}\ B_t^{D} \tag{6.8}$$

full-W AUG	C_0	A (P_{heat})	B (q_{95})	C (I_p)	D (B_t)	R^2
V1	0.423 $\pm$0.166	0.466 $\pm$0.16	$-$0.309 $\pm$0.14	0.228 $\pm$0.17	- -	0.72
V2	0.451 $\pm$0.184	0.49 $\pm$0.17	$-$0.506 $\pm$0.21	- -	0.202 $\pm$0.17	0.71
V3	0.381 $\pm$0.139	0.43 $\pm$0.16	- -	0.556 $\pm$0.21	$-$0.321 $\pm$0.14	0.73

Table 6.2.: Regression constant and exponents of the parameters including the regression variances and the regression coefficient, which denotes the quality of the regression between 0 and 1, where 1 stands for a perfect regression.

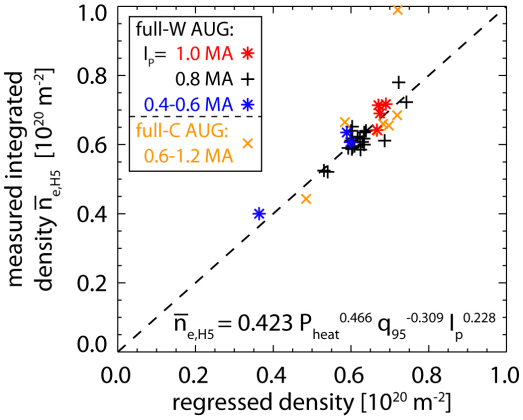

Figure 6.4.: Comparison of measured and predicted edge line averaged densities for the regression with the three significant parameters P_{heat}, q_{95} and I_p.

In figure 6.4 the measured density is compared with the regression formula. The regression reproduces the measured values quite well. It also aligns well with most of the HDL from the operation with carbon walls. A significant difference is only seen for a plasma current of 1.2 MA in full-C AUG. The individual dependencies of the full-W regression will be analyzed further in the following sections by dedicated parameter scans.

6.3. Plasma current

Due to the linear current scaling of the Greenwald limit, a likewise scaling is expected from the HDL. The regression yields a dependency of $I_p^{0.228}$ for a constant safety factor

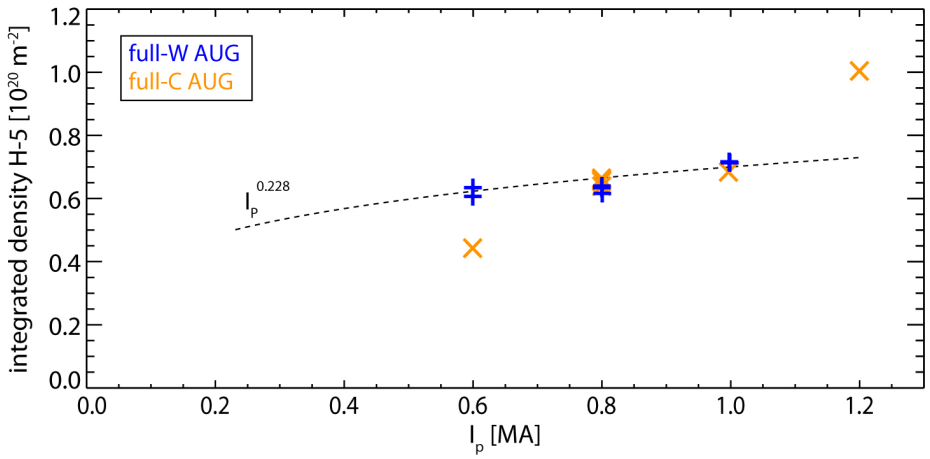

Figure 6.5.: Edge line integrated density (H-5) of the HDL versus the plasma current in full-W AUG at constant q_{95} and heating power (blue, $q_{95} \approx 5$, $P_{heat} \approx 8\,\mathrm{MW}$) and in full-C AUG (orange, $3 \leq q_{95} \leq 5.5$, see Fig. 5.5).

(i.e. a variation of B_t), significantly lower than expected. Figure 6.5 shows that the HDL densities of full-W AUG are similar for a plasma current of 0.6 MA and 0.8 MA and only slightly increased for 1.0 MA. These density values are highly reproducible and, notably, in full-C AUG similar densities were achieved for 0.8 MA and 1.0 MA. However, the data from the tungsten operation show the weak current scaling of the HDL, while the carbon discharges resemble an almost linear dependence.

The L-mode density limit in full-W AUG, which follows the HDL, does have a stronger I_p dependence than the HDL (not shown here).

Safety factor and the heating power are kept constant for the tungsten data in figure 6.5. The carbon data contains a variation of q_{95} between 3-5.5 and heating power between 5-8 MW. However, the observed variation of full-C AUG is not attributed to these changes.

The similar values for full-C and full-W AUG indicate, that for both setups similar mechanisms lead to the HDL. However, the two datasets yield a different current scaling. The linear scaling of the Greenwald limit cannot be reproduced.

6.4. Safety factor

The reported empirical scaling (Eq. 2.5) yields an almost linear dependence on the safety factor, albeit the ratio of $n_{HDL} \propto \frac{B_t^{0.57}}{q_{95}^{0.86}}$ might predominately imply a current dependency. A large variation of the safety factor was implemented in the new HDL database to validate this observation. At a constant plasma current, the q_{95} variation is realized by changing the toroidal magnetic field.

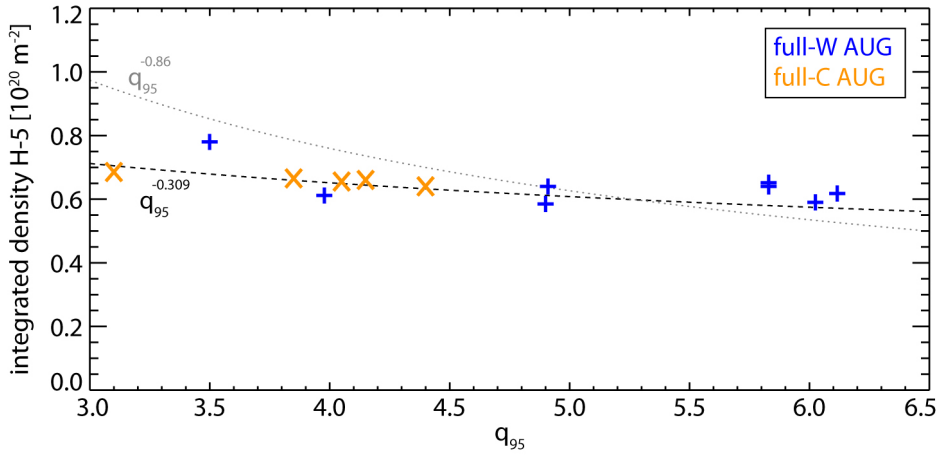

Figure 6.6.: Edge line averaged density (H-5) at the HDL versus q_{95} (safety factor at $\rho_{pol} = 0.95$) at constant heating power ($P_{NBI} = 7.5$ MW) and plasma current ($I_p = 0.8$ MA) for full-W AUG (blue) and full-C AUG (orange). The dotted line indicates the $q_{95}^{-0.86}$ dependency of the carbon scaling, the dashed line the $q_{95}^{-0.309}$ dependency out of the full-W regression.

For values of q_{95} between 4-6 (at constant heating power and plasma current), the HDL density in full-W AUG changes only marginally, as seen in figure 6.6. Only for rather low values of q_{95} around 3.5 is an increase of the density limit seen. For the carbon discharges, the HDL density does not change despite a significant q_{95} variation.
Neither of the two datasets reproduce the $q_{95}^{-0.86}$ dependence of the reported scaling. The weaker $q_{95}^{-0.309}$ dependence of the full-W regression appears to represent the carbon data well at a constant current.

6.5. Triangularity

The performance of an H-mode discharge is strongly influenced by the triangularity of the plasma [62, 63]. The triangularity is a shaping parameter, which denotes the radial shift between the X-points and the magnetic axis.
Figure 6.7 shows the magnetic equilibria of an HDL discharge at the typical medium triangularity ($\delta_{av} = 0.24$) and one HDL discharge at high triangularity ($\delta_{av} = 0.37$). A more extensive scan of triangularity was not carried out.
Figure 6.8 compares the evolution of three discharges at two different triangularities. For higher triangularities, the stable H-mode phase extends to higher densities. This is in line with the observations [62, 63], which report no influence of the triangularity on the confinement for low densities, but a significant increase with triangularity at high densities. This is represented by the changed shape of the curve and the later onset of

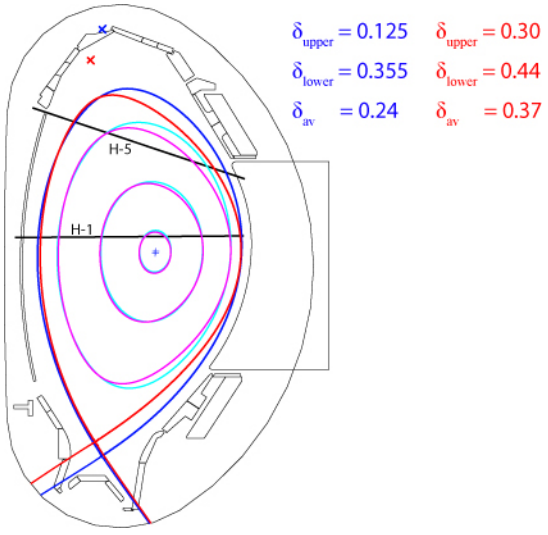

Figure 6.7.: Separatrix and magnetic flux surfaces for the standard equilibrium (blue, cyan) and the high triangularity equilibrium (red, magenta) of the HDL discharges. The position of the upper X-points is marked by the crosses, the values for the upper, lower and average triangularity are given on the top right. The interferometry LOS are indicated by the black lines.

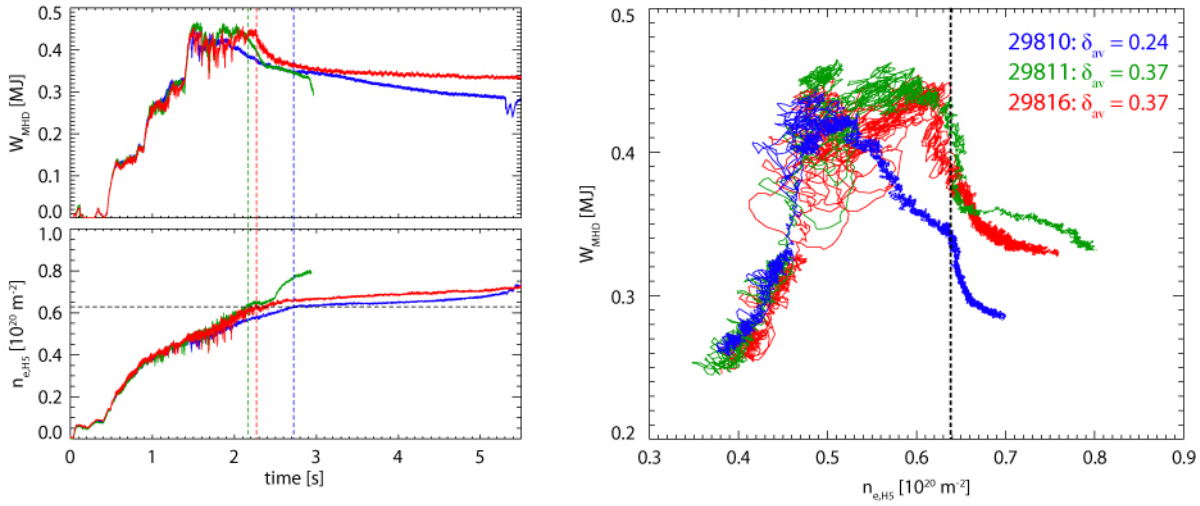

Figure 6.8.: Left: Stored energy (top) and edge line integrated density (bottom) of three discharges at two different triangularities. The time of the HDL is indicated by the vertical dashed lines. The density at the limit is the same for all three discharges (horizontal dashed line).
Right: Stored energy plotted versus the edge line integrated density. For the high triangularity discharges, the stable H-mode phase is prolonged and the degrading H-mode phase is shorter. All three discharges have the same edge density at the limit.

the second phase.

However, eventually the degrading H-mode phase sets in and leads to a significant drop of confinement with a small increase of the density. Nonetheless, the degrading H-mode phase and the breakdown phase are still distinguished. For the discharges compared in figure 6.8, the timing of the HDL does vary, but the density at which the H-mode breakdown phase takes place is the same for all three discharges (indicated by the dashed lines).

This is in contradiction with observations at the DIII-D tokamak [64]. A reduction of the pressure is seen with increasing density, similar to the degrading H-mode phase. But the density, at which this reduction sets in, is independent of the triangularity (Fig. 4 of [64]).

With the higher triangularity a lower gas puff is necessary to achieve the HDL. Thus, the triangularity might have an effect on the fueling limit. This also explains why the second phase sets in later.

ITER will be able operate at higher triangularities ($0.2 \leq \delta_{ITER} \leq 0.5$), therefore, an operation at densities close to the HDL in the stable H-mode phase might be feasible.

In conclusion, the triangularity might affect the plasma performance and the fueling of the plasma, i.e. the stable H-mode phase exists up to higher densities and a higher confinement can be reached at high densities, but it does not have an influence on the HDL density.

6.6. Heating power

The HDL is supposed to be power independent (see Fig. 2.4), similar to the Greenwald limit. In [21] it is reported that the HDL at JET with the ITER-like wall is independent of the external heating power between 8 MW and 10.5 MW. In [15], the same was shown for AUG with carbon as a first wall material. The carbon scaling revealed a negligible dependence on the power flux across the separatrix ($n_{HDL} \propto q_{\perp}^{0.049\pm0.041}$). However, the regression of the full-W data yields a significant power dependency of $P_{heat}^{0.46}$.

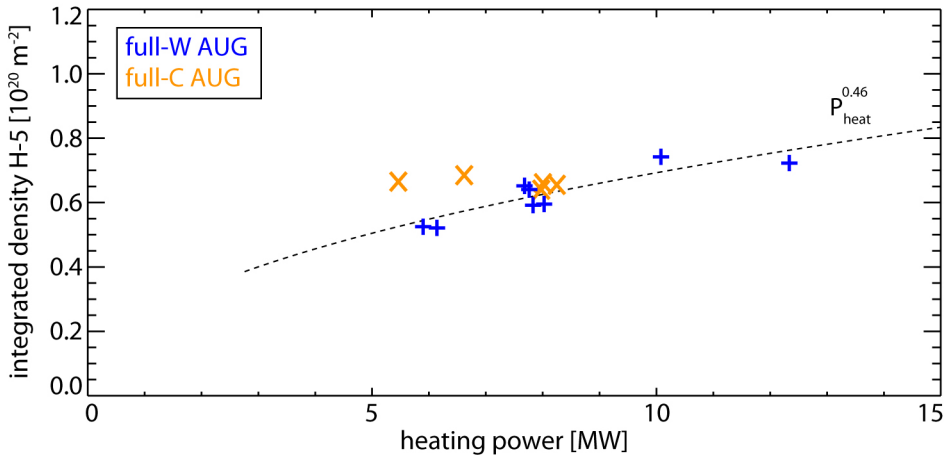

Figure 6.9.: Dependency of the line averaged edge density (H-5) at the HDL on the total heating power at $I_p = 0.8$ MA and $q_{95} \approx 6$ for full-W AUG (blue) and full-C AUG (orange). The dashed line indicates the regressed scaling ($P_{heat}^{0.46}$) which is not reproduced by the carbon data.

Figure 6.9 contains a change of NBI heating power between 5 MW and 12.5 MW (2-5 NBI sources) at constant plasma current and safety factor for full-W AUG. The achieved density increases significantly with the heating power. On the contrary, the heating power does not have an influence on the HDL density for full-C AUG.

The heating scan does not include a variation of the heating source. Only the intrinsic Ohmic heating and NBI heating were used. A discharge with RF wave heating (ECRH, ICRH) was not carried out.

The existing power dependence of the HDL in full-W AUG can be seen in discharge AUG #29810, where the heating power is increased during the L-mode phase (see Fig. 6.10). With the higher heating power the plasma goes back into H-mode (i.e. the H-mode breakdown phase) and a higher density is achieved. Afterwards, the density stays fixed until the L-mode is reached once again. Thus, this discharge includes two HDL and shows directly that the HDL is power dependent, at least for full-W AUG. It also proves that the H-mode breakdown phase is a stable regime, since it can directly be accessed without the necessity of passing through the first two phases beforehand.

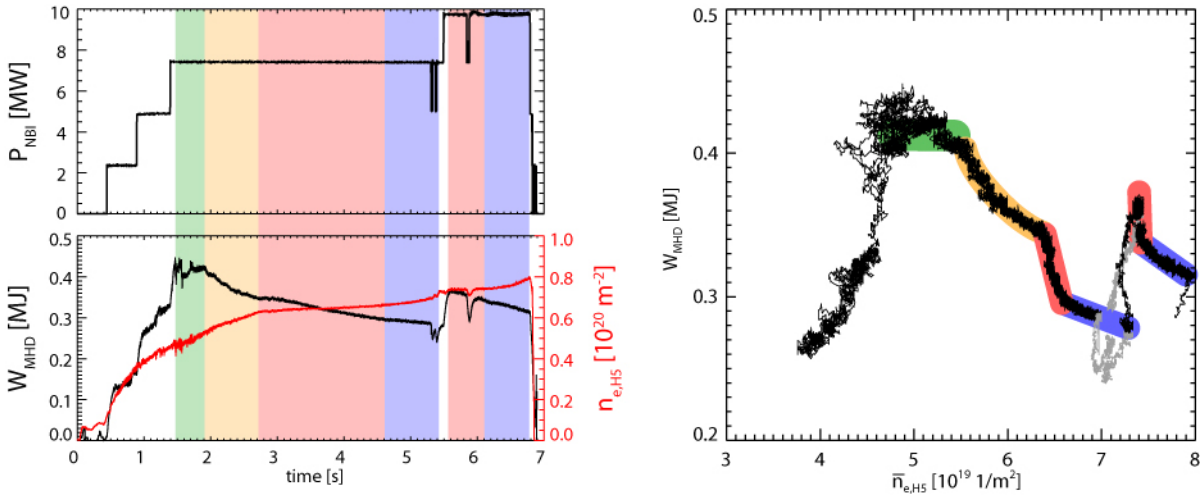

Figure 6.10.: An increase of heating power in the L-mode phase drives the discharge back into H-mode (AUG #29810). The HDL density is increased with higher heating power.

6.7. Concluding the parameter variations

The density, at which the HDL occurs is on the same order of magnitude for full-W and full-C AUG. It does not matter which density measurement is considered, since the density profiles are flat and thus all measurements are linearly correlated.

The scaling of the carbon data [18] yields the right order of magnitude for the HDL density, however, the individual dependencies of safety factor, triangularity and heating power could not be reproduced for full-W AUG. A regression analysis of the full-W database results in

$$\overline{n}_{e,H5,regr.V1} = 0.381 \; P_{heat}^{0.466} \; q_{95}^{-0.309} \; I_P^{0.228} \tag{6.9}$$

The triangularity impacts the performance of the plasma at high densities but does not influence the HDL density itself.

The carbon and tungsten data is of the same order of magnitude but deviate in the scaling of plasma current and heating power. Full-C AUG yields an almost linear current dependence, but shows no effect of the heating power. On the contrary, the HDL in full-W AUG has a significant dependence on the heating power and only weak dependencies on the parameters. Assuming the HDL is based on two mechanisms, as indicated in section 5.5, the changed scaling at similar densities indicates that at least one of these mechanisms changed for the operation with different wall materials.

7. Proposed mechanisms for the HDL

Several mechanisms were proposed by previous studies to cause the HDL. These mechanisms are revised for the new database of full-W AUG, using the improved diagnostic capabilities of the actual setup.

7.1. Complete detachment

In [18, 20, 65], the complete detachment of the outer divertor was identified to trigger the HDL in a full-C device. If the plasma is not in direct contact with the wall, an ionization and recombination front moves towards the X-point with increasing density. It is assumed that neutrals penetrate the confined region if the ionization front is close to the X-point. The neutrals would cool down the pedestal by line radiation and lead to the back transition to L-mode.

Figure 7.1 compares one discharge of full-C AUG with one of the presented dataset of full-W AUG. The complete detachment is identified by the drop of the ion saturation current measurement (bottom figures). As indicated by the dashed lines, the HDL occurs in full-C AUG about 300 ms after the full detachment of the outer divertor. It was concluded that the detachment as the general, underlying physical mechanism triggers the back transition. However, in full-W AUG, the complete detachment sets in after the HDL.

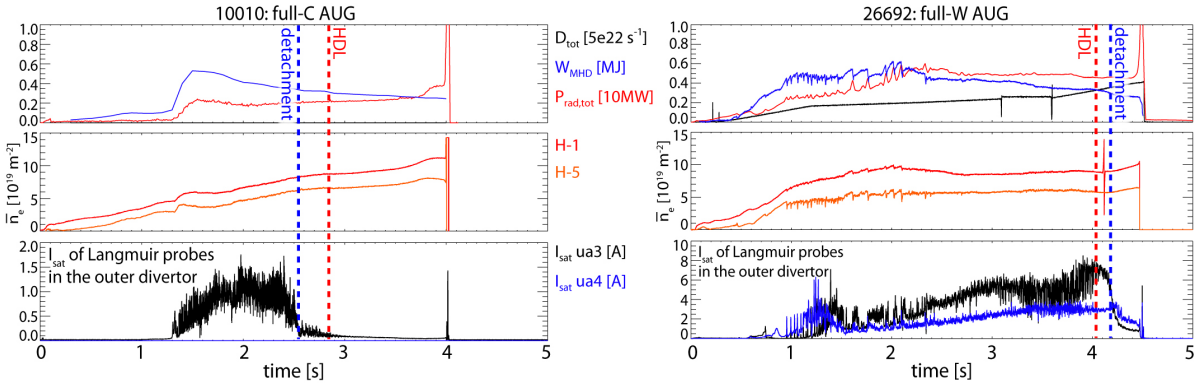

Figure 7.1.: Various measurements of HDL discharges in full-C AUG (left, AUG #10010) and full-W AUG (right, AUG #26692). The time when the HDL sets in is marked by the red dashed line, the time of the detachment (seen by the I_{sat} measurements) of the outer divertor by the blue dashed line.

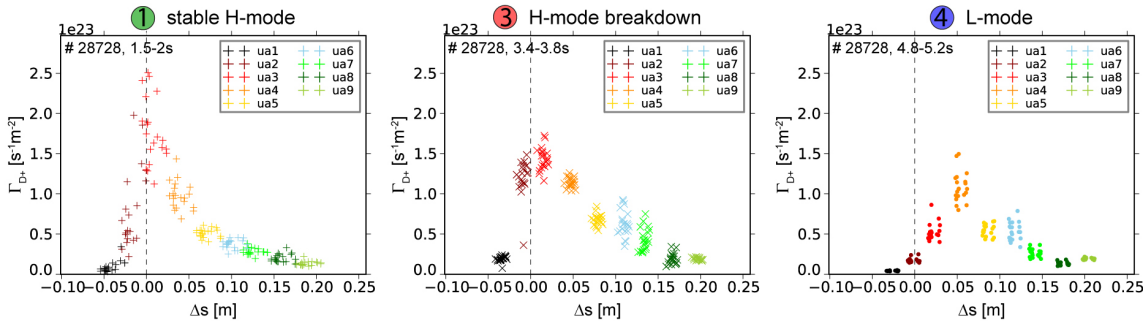

Figure 7.2.: Ion flux density on the target plates derived out of the ion saturation current density of the Langmuir probes in the outer divertor plotted versus their distance from the strikeline along the target plates (Δs) for the different HDL phases (left: stable H-mode phase; middle: breakdown phase of H-mode; right: L-mode phase).

In figure 7.2 the ion saturation profiles of the outer divertor target are shown for the different phases of the HDL in full-W AUG. The reduction of the profile peak indicates a partially detached state of the outer divertor, but not complete detachment. Even in the L-mode phase, the divertor is not completely detached. Thus, the HDL cannot be triggered by the complete detachment.

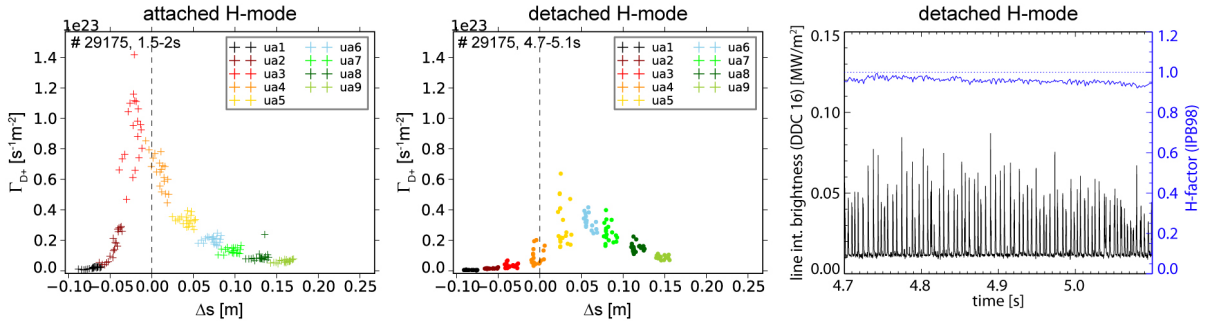

Figure 7.3.: Ion saturation current density profiles for an attached (left) and detached (middle) H-mode. Right: ELM induced radiation and an H-factor of about 1 evidently proves the existence of an H-mode during the detached phase.

Furthermore, also stable H-modes with a completely detached outer divertor are observed. Figure 7.3 shows the probe measurements of a fully detached H-mode (AUG #29175). The peak of ion saturation current is completely vanished and a measurable current remains only in the outer SOL (ua5-ua7, see Fig. 3.19). The H-factor is about 1 and ELMs are present, indicating a stable H-mode with good confinement. Thus, the complete detachment of the outer divertor is not sufficient for an HDL to occur in the present experimental setup with tungsten plasma facing components (PFCs).

The difference between the old and new dataset is attributed to the operation with different wall materials. Carbon as the wall material is, at typical particle energies,

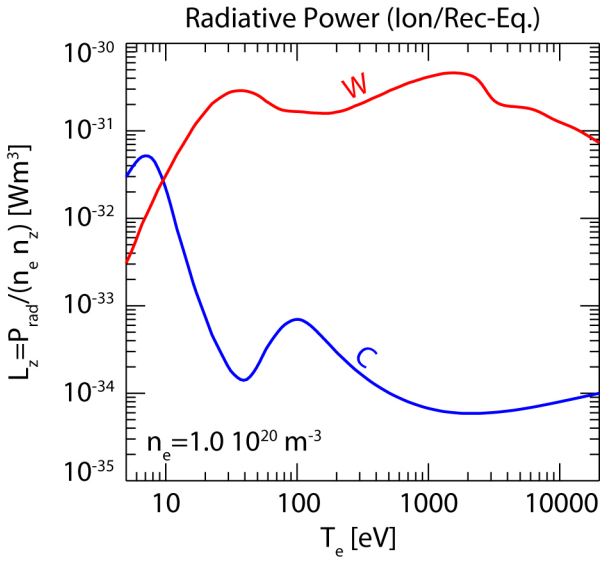

Figure 7.4.: Radiative cooling factor L_Z for tungsten [66] and carbon [67]. Carbon radiates efficiently in the SOL, tungsten in the core. Tungsten is only acceptable as a wall material if its absolute concentration in the plasma is kept orders of magnitude lower than the carbon concentration in a full-C device.

more strongly sputtered than tungsten. Therefore, the carbon concentration in full-C AUG is much higher than the tungsten concentration in full-W AUG.

Carbon radiates efficiently at the low electron temperatures of the SOL and divertor plasma. On the contrary, tungsten radiates efficiently in the core of the plasma, since it is not fully ionized there. The radiative cooling factor L_Z is shown in figure 7.4. The low tungsten concentration leads to insignificant tungsten radiation in the SOL.

Thus, the composition of the SOL plasma and its radiation characteristics changed significantly with the different wall materials. In the operation with carbon PFCs, the complete detachment occurs earlier and the parameter ranges, where the detachment and the HDL take place, overlap. For full-W AUG, these processes take place in separate parameter ranges, therefore, the *"actual"* HDL mechanism is not screened by the detachment.

7.2. Radiation losses

Additional energy losses due to radiation can cool down the confined plasma and thus cause the HDL. The above mentioned mechanism attributes this additional radiation to the full detachment, but also other effects can lead to an increased radiation. These radiation losses are most often expected around the X-point region, due to the high neutral gas pressure and the small distance between the neutral gas and the hot pedestal of the confined plasma. The foil bolometry is an optimal tool to detect any changes in the radiation pattern and several of its measurements are shown here.

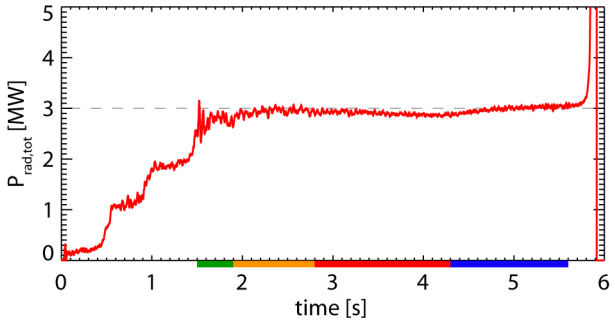

Figure 7.5.: Total radiated power during HDL discharge AUG #28728. The radiated power is almost constant for all phases (indicated on bottom).

The total radiated power does not change throughout the four phases (see Fig. 7.5).

To exclude the possibility that the total radiated power is constant but the radiation distribution changes, i.e. radiation shifts from the divertor to the confined plasma, and causes the back transition to L-mode, we present figure 7.6. This shows contour plots of the measured radiation from four bolometer cameras covering the whole poloidal cross section of the plasma. The radiation is plotted over the time and the LOS of the cameras. None of the LOS shows a significant increase of radiation in the first three phases. Furthermore, LOS, which observe the divertor, measure decreasing radiation. The latter might be an effect of the vanishing of the ELMs. In the L-mode phase an increase of radiation is seen in the LOS observing the X-point as the MARFE develops.

Figure 7.7 shows tomographic reconstructions of the radiation distribution (see Sec. 3.2.1). No increase of radiation is observed. These reconstructions also show a decreasing level of radiation around the X-point.

The X-point fluctuations (see Sec. 5.1) are the only emerging radiation. They are seen, for example, by channel 3 of camera FLX in figure 7.6. However, their radiated power decreases and the fluctuations are also observed in L-mode [56] and are, thus, not specific to the HDL.

Furthermore, the back transition to L-mode can lead to an increased radiation. In discharge AUG #28137 the drop of the stored energy takes place within 200 ms (see Fig. 7.8). Within this time, 0.1 MJ of stored energy are lost. About half of this energy is radiated by the plasma, as seen by the peak in the total radiation (green arrows).

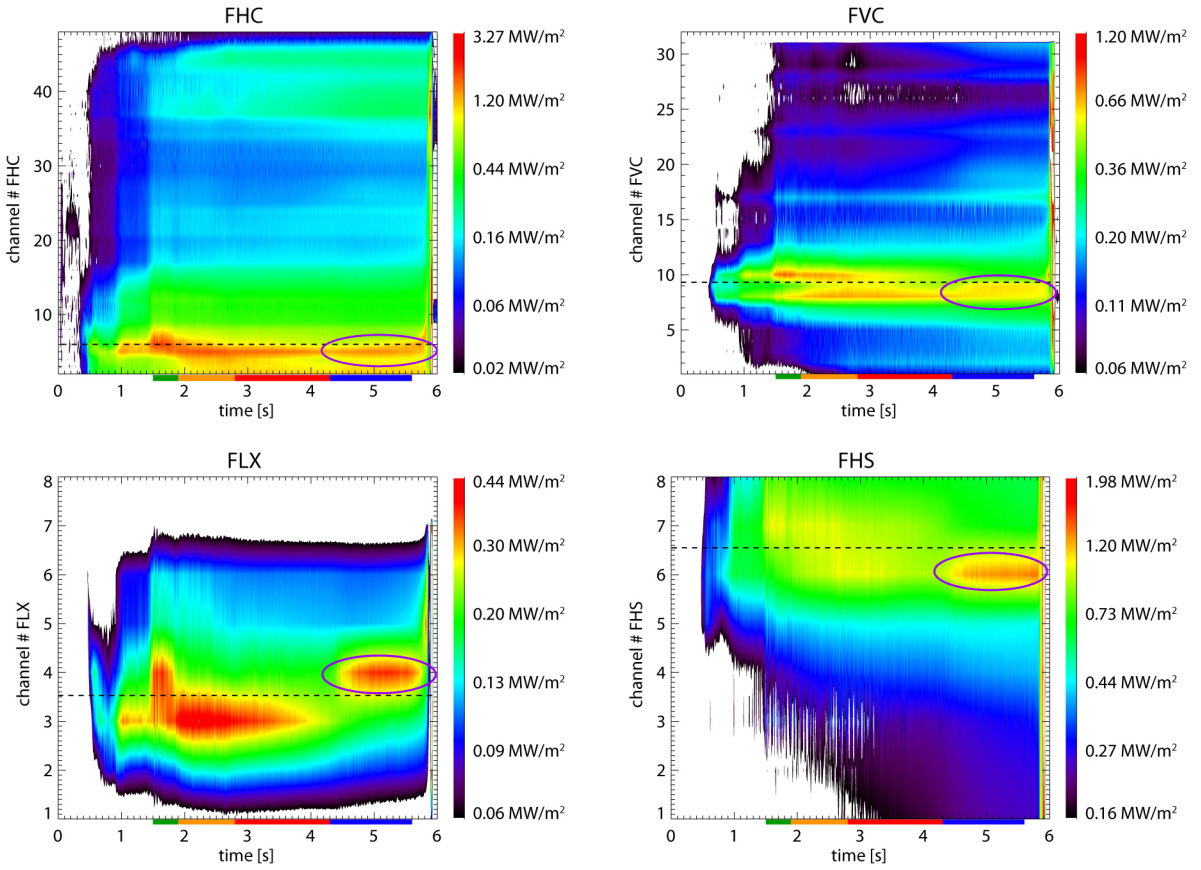

Figure 7.6.: Brightness along the LOS measured by several cameras of the foil bolometry for discharge AUG #28728. The positions of the cameras can be seen in figure 3.1. No additional radiation losses can be seen in the first three phases (indicated on the bottom of the plots). Only in the L-mode phase does the radiation increase around the X-point (dashed line), where the MARFE develops (indicated with purple circles).

This radiation is not localized. However, the radiation does not trigger the HDL but is a consequence of the lost energy.

7.3. MARFE

A MARFE (Multifaceted Asymmetric Radiation From the Edge) is a toroidally symmetric, poloidally localized radiation instability [68]. It is a SOL effect and appears for divertor experiments mostly around the X-point.

A MARFE generates a cold, dense plasma region, which radiates up to several MW of power. If a MARFE develops at the X-point, it reduces the power flux into the divertor and thus initiates detachment. If the cold, dense plasma is close or inside the confined plasma, it can cool the pedestal and lead to an HDL. Typically, it is observed that a

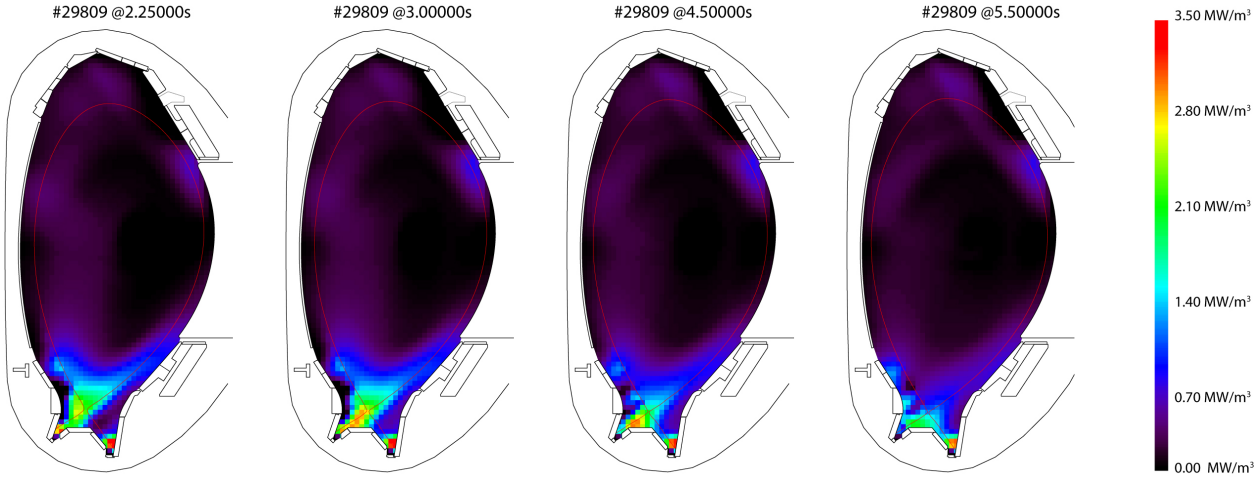

(a) stable H-mode **(b)** degrading H-mode **(c)** H-mode breakdown **(d)** L-mode

Figure 7.7.: Deconvolutions of the radiation measured by the foil bolometry for the four different phases of AUG #29809. No increase of the radiation is seen from (a) to (d).

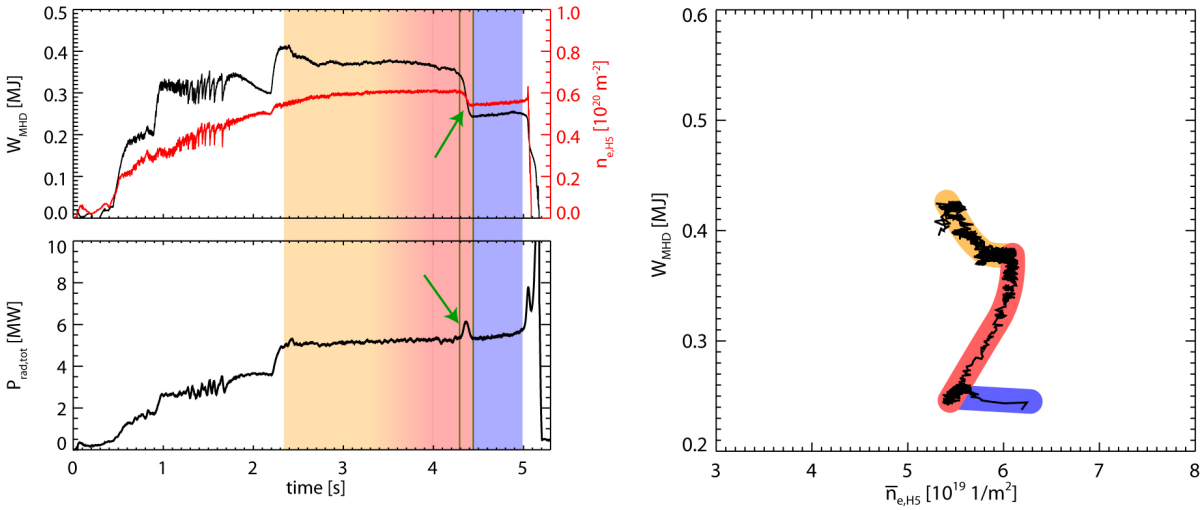

Figure 7.8.: The radiated power is increased during the fast drop of the stored energy in AUG #28137 (green arrows). The lost energy is partially radiated.

stable X-point MARFE starts to move towards the inflowing power, i.e. upwards along the high field side SOL. For the observed discharges, this movement coincides with the onset of an internal tearing mode, which leads finally to a disruption.

The MARFE instability arises if the radiated power of a volume is increasing with

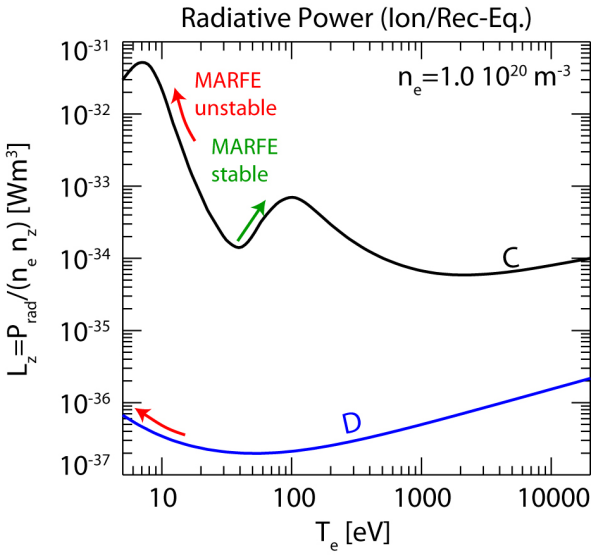

Figure 7.9.: Radiative cooling factor L_Z of carbon and deuterium [67]. The parameter ranges where MARFEs are stable or can become unstable are indicated. For pure deuterium plasmas, this only occurs at very low temperatures, where significant recombination takes place.

decreasing temperature, i.e. emissivity features a negative temperature gradient

$$\frac{\delta \epsilon_{rad}}{\delta T_e} < 0, \tag{7.1}$$

where

$$\epsilon_{rad}\,(T_e, n_e) = \sum_{\text{atom species}} n_Z\; n_e\; L_Z(T_e) \equiv \sum_{\text{atom species}} c_Z\; n_e^2\; L_Z(T_e) \tag{7.2}$$

and

$$P_{rad} = \int \epsilon_{rad}\; dV \tag{7.3}$$

with the radiative cooling factor L_Z, the density n_Z and the concentration c_Z of the atom species Z. The cooling factor of carbon and deuterium is shown in figure 7.9.

The emissivity (Eq. 7.2) is dependent on the composition of the plasma. A negative temperature gradient of the emissivity is created, for example, by a significant carbon concentration for temperatures between 100-1000 eV (see Fig. 7.9). If a region of the plasma is in the unstable temperature range, more power is radiated if the temperature decreases. If the additional radiated power is not compensated by an increased power influx, the region cools down and thus radiates more. Additionally, the density increases due to the constant pressure along a magnetic field line, which is further increasing the radiation and amplifying the cooling.

However, the development of a MARFE close to the confined region depends on the impurities in the SOL plasma. In figure 7.9 it is seen that a pure deuterium plasma is only MARFE unstable for very low temperatures. At these temperatures a significant fraction

of the deuterium atoms is not ionized and can, therefore, efficiently radiate by spectral lines. A negative gradient in the emissivity coefficient in the relevant temperature region ($\sim$ 100 eV) can only be created by a significant concentration of impurities, such as carbon, which are not fully ionized at these temperatures.

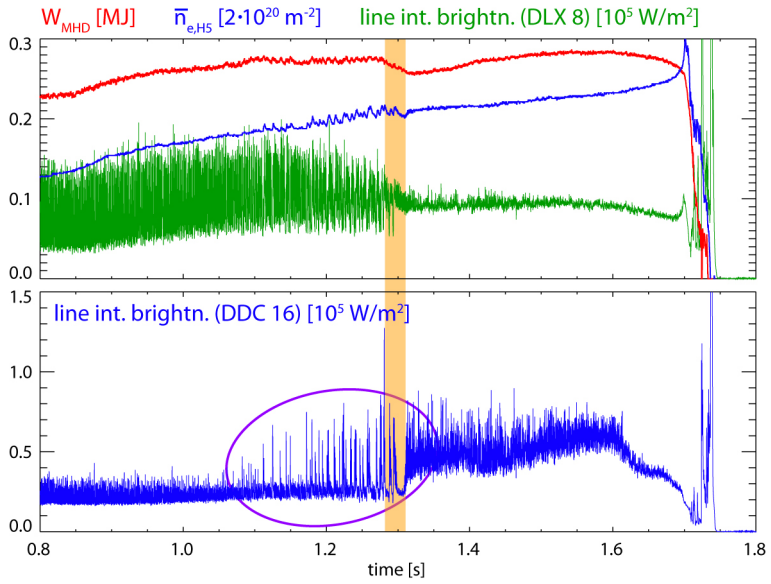

Figure 7.10.: H-L transition due to a MARFE (AUG #30117). The top plot shows stored energy, line integrated density and a diode bolometry signal of the outer divertor. The H-L transition (orange vertical line) can be seen by the reduction of stored energy and the vanishing of the ELMs (oscillations on diode bolometer signal). The bottom plot shows a diode bolometer signal observing the region slightly above the X-point. The development of the MARFE can be seen as fluctuations on the signal. In L-mode the MARFE is stable and thus the signal constantly increased.

Figure 7.10 illustrates a discharge, which exhibits an H-L transition due to a MARFE. This can be triggered for example by a high impurity concentration in the plasma. This increases the influence of the impurity on the emissivity coefficient (see Eq. 7.2) and can create MARFE unstable temperature ranges. The developing MARFE is cooling the plasma at the X-point and leads to the back transition to L-mode.

However, for the dedicated HDL discharges the impurity concentration is rather low due to the high neutral gas pressure. A deuterium MARFE is developing after the transition to L-mode (see Fig. 5.16), where the divertor detaches and significant recombination of deuterium takes place. In any case, another effect has to trigger the HDL before reaching the L-mode phase.

7.4. Power below the L-H threshold

For the transition from L- to H-mode, a minimum heating power is required. This L-H power threshold (P_{L-H}) was already introduced in section 2.3. The threshold is given for the loss power defined as

$$P_{loss} = P_{heat} + P_{ohmic} - dW_{MHD}/dt \tag{7.4}$$

where P_{heat} includes all external heating powers, P_{ohmic} is the ohmic heating power and dW_{MHD}/dt is the change of the plasma stored energy. Prompt losses of the heating are excluded.

For medium to high densities, the threshold scales with the central line averaged density ($\overline{n}_e$ in $10^{20}\mathrm{m}^{-3}$), the magnetic field at the geometric axis (B_T in T) and the separatrix surface area (S in m^2):

$$P_{L-H}[\mathrm{MW}] = 0.0488e^{\pm 0.057}\ \overline{n}_e^{0.717\pm 0.035}\ B_T^{0.803\pm 0.032}\ S^{0.941\pm 0.019} \quad [69] \tag{7.5}$$

This scaling is derived from various different tokamaks. The physics of the L-H transition is, however, not yet fully revealed. It is assumed [19], that the power flux over the separatrix, i.e. the loss power minus the radiated power inside the confined region, is the actual parameter for the L-H transition. However, the radiated power inside the separatrix cannot be determined accurately enough and thus is not taken into account for the scaling.

Note that this scaling is deduced from experiments with carbon PFCs. A reduction of the power threshold by about 25% is observed for the operation of AUG with tungsten PFCs [19] and JET with tungsten and beryllium PFCs [70].

A transition from H- to L-mode takes place if P_{loss} is below the threshold (disregarding the hysteresis, which exists at medium densities). This is typically observed by a reduction of the heating power. Also the HDL could be caused by a reduction of the power flux across the separatrix. Thus, the HDL would be a usual H-L transition caused by a power reduction.

Figure 7.11 compares the power influx to the divertor (P_{div}, orange) with the scaling of equation 7.5 (P_{L-H}, red). P_{div} is calculated out of the divertor radiation $P_{rad,div}$, which is determined by tomographic reconstructions of the bolometry measurements(see Sec. 3.2.1), and the power flux onto the target plates P_{target} measured by the thermography. P_{div} is a lower bound of the loss power and the power flowing across the separatrix.

Already the power influx in the divertor is well above the L-H threshold in the first three phases, therefore, the power threshold is not responsible for the degrading H-mode or the H-mode breakdown. However, at the start of the L-mode phase the power is below the threshold. It might well be that the L-H power threshold is determining the final transition from the breakdown phase of the H-mode to the L-mode.

In figure 7.11 it can also be seen, that an increase of the heating power raises P_{div} above the L-H threshold. This leads again to a transition into H-mode, i.e. the third phase (see

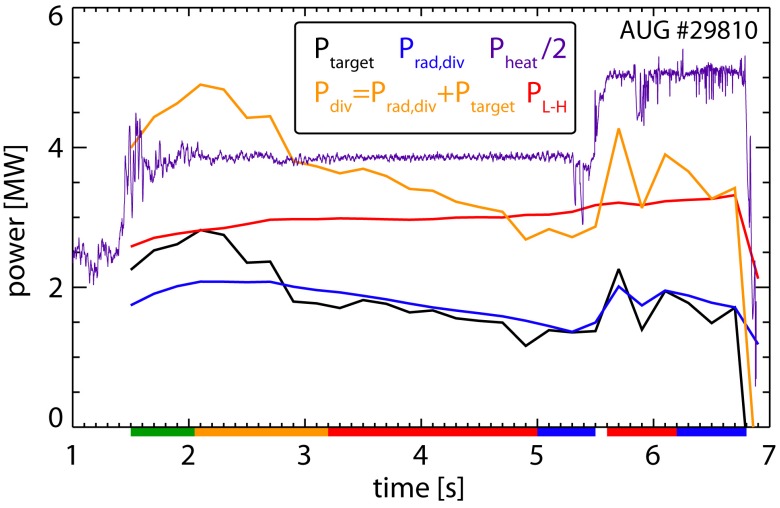

Figure 7.11.: L-H power threshold (P_{L-H}), power deposition on the divertor target plates measured by thermography (P_{target}), radiated power in the divertor volume ($P_{rad,div}$), scaled total heating power (P_{heat}) and the power influx in the divertor (P_{div}) plotted versus the time. The four phases are indicated by the colors along the bottom. Note, that the error bars on the measurements are in the range of 1 MW.

also Fig. 6.10). When P_{div} is once again close to the threshold, the plasma goes back into L-mode. This indicates, that the L-H threshold might determine the transition between the last two phases in both directions.

7.5. Reduction of the radial electric field

In reference [8] a threshold of the depth of the radial electric field (E_r) well of 15 kV/m is reported for the L- to H-mode transition in discharges with $I_p = 0.8$ MA and $B_t = 2.3$ T. It is worth checking if a similar threshold is present at the back transition at the HDL for similar values of I_p and B_t.

In figure 7.12 the E_r profiles at the start of the H-mode breakdown phase are shown for four discharges at 0.8 MA and 2.2 T. The E_r well depth varies between 24-37 kV/m, well above the reported threshold. No specific value can be assigned for the depth of the E_r well at the start of the HDL.

Figure 7.13 shows the evolution of the E_r well during the breakdown phase, derived from the kinetic profiles. From its initial value well above the threshold, it is eroded to values of around 15 kV/m shortly before the discharge is in the L-mode phase. Unfortunately, there are no data for the L-mode phase available. Additionally, the profile evolution shown in figure 7.13 lacks validation from the direct measurements of E_r. Nevertheless, it indicates that the E_r well reduces during the breakdown phase close to values of the reported L-H threshold.

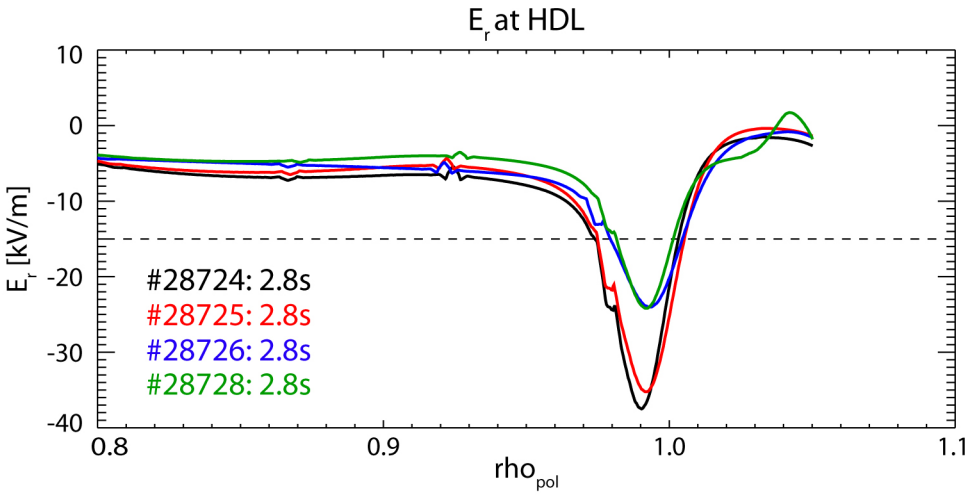

Figure 7.12.: E_r profile for four HDL discharges evaluated from the kinetic profiles. The dashed line indicates the threshold of 15 kV/m. The evaluations for discharges AUG #28724, 28726 and 28728 are validated by CXRS or Doppler reflectometry measurements (see Sec. 3.4.5).

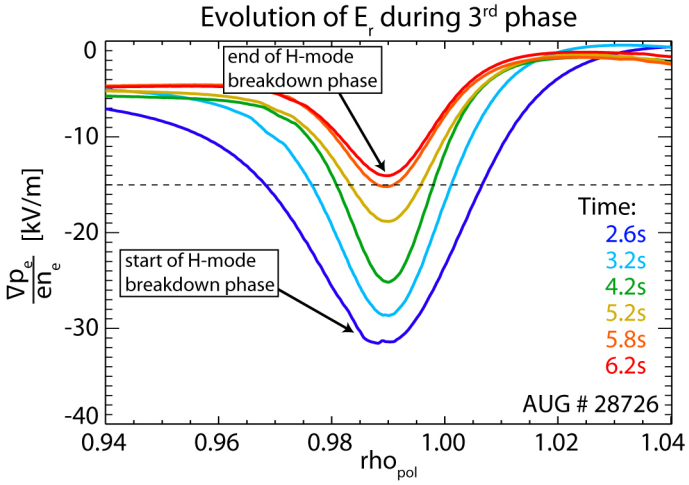

Figure 7.13.: Evolution of the E_r well evaluated from the kinetic profiles during the third phase in AUG #28726.

In conclusion, the E_r well depth does not trigger the HDL, but might be responsible for the final transition into L-mode. The E_r threshold might be interpreted as the local parameter which is described by the global L-H power threshold.

7.6. ELMs

In references [20, 13], ELMs are discussed to trigger the HDL. ELMs erode the strong gradients of density and temperature at the edge of the plasma in sub-millisecond timescales. The recovery of the pedestal to its initial value can take more than 5 ms [71]. Typical ELM frequencies are around 100 Hz for AUG, implying an ELM cycle time of about 10 ms. If an ELM would erode the gradients before they are fully recovered, the pedestal could successively be reduced.

ELMs are pressure and current driven instabilities, thus, an ELM is usually triggered after the pressure gradient is fully recovered. However, if the ELMs are triggered by another mechanism, the ELM cycle time (τ_{cycle}) could be smaller than the recovery time of the pedestal (τ_{ped}). In the HDL discharges, the frequency of the type III ELMs continuously increases due to the increasing density, and one might reach a condition of $\tau_{ped} > \tau_{cycle}$.

Figure 7.14 shows two AXUV diode signals as ELM indicators. The ELMs change from type I to type III during the first phase, the stable H-mode. Afterwards the ELM frequency rises as seen in the spectrogram. The ELM size, which can be measured by the relative energy loss or by the observed radiated power (top plot), decreases. Finally, the ELMs vanish at around 3.7 s.

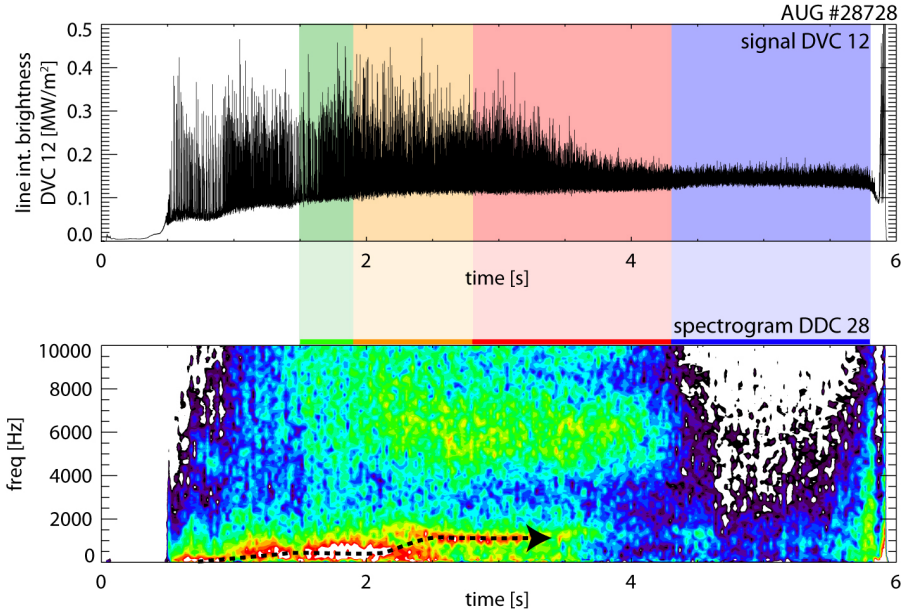

Figure 7.14.: AXUV signal (DVC 12, top) and spectrogram of an AXUV signal (DDC 28, bottom) of HDL discharge #28728. ELMs are seen as spikes in the signal or as low frequency band (∼50-1000 Hz) in the spectrogram. The signal around 4-8 kHz are the X-point fluctuations (Sec. 5.1.2). The ELMs vanish at around 3.7 s, the degradation continues until 4.3 s.

However, the degradation of the confinement (third phase) goes on after the ELMs vanished. This is also observed for several other HDL discharges. Thus, there must be another effect causing the degradation. It cannot be excluded, that the onset of the HDL is related to the ELMs, but it is apparent that there is an additional energy loss channel apart from ELMs.

7.7. Charge exchange collisions

At the high neutral density of the HDL discharges, the neutral particles can lead to increased energy losses. Hot ions are neutralized inside the confined region by charge exchange collisions. These fast neutrals are not bound to the magnetic field and can carry their energy across the separatrix and deposit it directly on the wall.

ASDEX Upgrade is equipped with two neutral particle analyzer systems (NPA, [72]), which measure the energy resolved flux of deuterium and hydrogen atoms out of the plasma. The NPA, which measures neutrals with energies originating from the pedestal region, is currently not in operation. However, the NPA, which detects neutrals from further inside the confined plasma, i.e. regions with temperatures above 700 eV, measures no significant increase of the neutral flux.

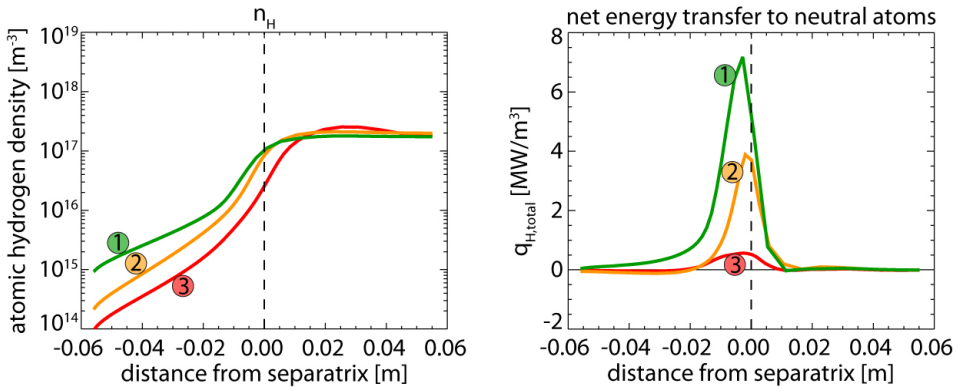

Figure 7.15.: Neutral atom density (left) and net energy transfer to the neutrals (right) calculated by the KN1D code from the electron density and temperature profiles shown in Fig. 8.1.

The net energy, which is transfered to the neutral atoms by elastic and charge exchange collisions, is calculated by the KN1D code [52]. The right hand side of figure 7.15 shows this transfered energy for three different density profiles, which are explained in detail in section 8.1. They correspond to the beginning of the first, second and third phase, respectively. The left hand side of figure 7.15 shows the atomic neutral density out of the KN1D calculations.

In the third phase the energy loss is ongoing and supposed to be at its maximum. However, the net energy transfer to the neutrals is significantly reduced in this phase.

The energy transfered to the neutrals decreases due to the low neutral atom density around the pedestal. Most of the neutrals are ionized further outwards, where the temperatures are lower and thus less energy is transfered by charge exchange reactions. Thus, the charge exchange collisions are found not to be responsible for the increased energy losses.

However, ionization, fueling and neutral gas density are highly poloidally asymmetric. The latter, for example, is a factor of 100 higher in the divertor than in the main chamber. The one-dimensional model KN1D cannot resolve the divertor or any other poloidal asymmetries. Thus, charge exchange losses might occur close or inside of the divertor and are not reproduced by the code. A two-dimensional model, like SOLPS, takes also the divertor into account. However, the modeling of an HDL discharge with this code package has so far not been successful due to instable simulations in this parameter region.

8. Interpretation and discussion of the four phases

The observation of the four phases is essential to understand the process of the H-mode density limit. In chapter 5, characteristics of the four phases are shown. These four phases can be explained by the combination of two effects that interfere differently in each phase. On the one hand, there is a nonlinear density evolution, which leads to a temporary stagnation of the density increase, and on the other hand, there is an increased or additional energy loss channel.

1 In the stable H-mode phase, either of the two effects is active. The density increases and the confinement is constant.

2 In the degrading H-mode phase, the nonlinear density evolution sets in, while the density in the scrape-off layer (SOL) increases further. Also, a degradation of the confinement is suddenly initiated. This is interpreted as the onset of an additional energy loss channel.

3 At the breakdown of the H-mode, the effect of the nonlinear density evolution prohibits any further density increase. Meanwhile, the energy loss increases, continuously eroding the pedestal.

4 When the L-mode is reached, both effects cease and the line averaged densities increase at a constant energy confinement at typical L-mode levels. The final transition to L-mode might be triggered by a threshold of the radial electric field well (Sec. 7.5) or the L-H power threshold (Sec. 7.4), which are presumably related.

Though we differentiate between the nonlinear density evolution and the additional energy loss channel, both effects are coupled. Together they take effect at the beginning of the second phase and both stop when the L-mode is reached. This coupling leads to the sharp bends in the graph of stored energy versus line integrated density.

In this chapter, we show experimental evidence of these two effects and propose possible causal mechanisms. It will be discussed whether the effects are coupled or are caused by the same process. Finally, this theory is examined with respect to observations made in full-C AUG.

8.1. Nonlinear density evolution

The electron density increase first saturates in the core of the plasma and, thus, a density plateau builds up in the SOL. The plateau increases up to about half of the pedestal

top density and then also saturates. It cannot be determined definitively whether the density plateau is dominated by an average over high density fluctuations or by an increased steady background density.

In section 4.2, the fueling limit is introduced as a mechanism which decouples the electron density from the neutral gas density for high densities. We suggest that this effect is caused by an outward shift of the ionization profile. The increase of density in the L-mode phase implies, however, that the fueling limit presented here is specific only to the H-mode.

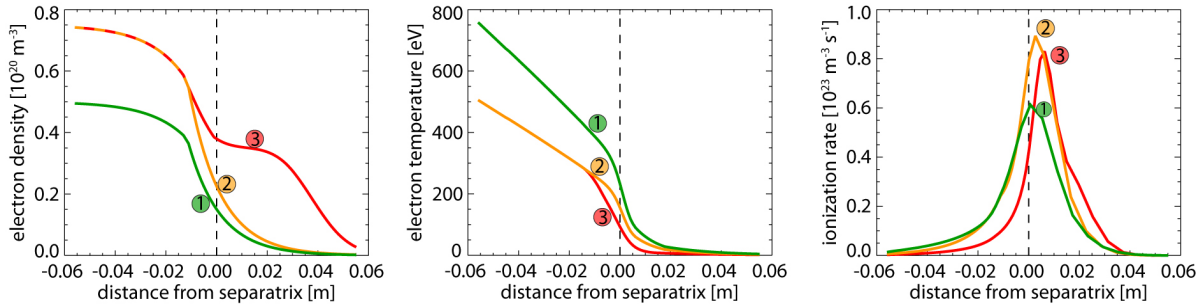

Figure 8.1.: Electron density (left) and electron temperature (middle) profiles used to calculate the local ionization rate (right) with the KN1D code. The electron pressure profile is in all three cases the same.

In figure 8.1, the ionization rate is calculated for three density profiles by the one-dimensional neutral transport algorithm KN1D [52]. ③ The red density profile is measured at the beginning of the H-mode breakdown phase. The other two profiles are derived from the latter. ② For the orange density profile an exponential decay from the pedestal top outwards is assumed, exemplifying the behaviour typically seen in the beginning of the degrading H-mode phase. This profile is used in order to identify the effect of the SOL density plateau on the neutral particles. ① The green density profile is overall reduced and is typical for the profiles measured at the beginning of the stable H-mode phase. The same electron pressure profile is assumed for all three cases and the neutral gas pressure at the wall (distance to separatrix = 0.055 m) is kept constant. Similar observations can be made, if the same temperature profile is assumed for all three cases.

With increasing density (① to ②), the volume integrated ionization rate increases in the SOL by 30%. The ionization rate inside the confined region is similar. With the SOL density plateau ③, the ionization profile is almost completely shifted into the SOL. The integrated ionization rate is roughly constant outside of the separatrix, but decreases by 50% inside. This indicates that the core fueling is significantly reduced in the presence of the SOL density plateau.

The density profile of ② is a hypothetical case since the increased ionization rate in the SOL would lead directly to an increased density in this region. The shift of the ionization profile is a self-amplifying process. The observed phases are stable regimes in a quasi steady-state mode. The outward shift of the ionization, the SOL density and the

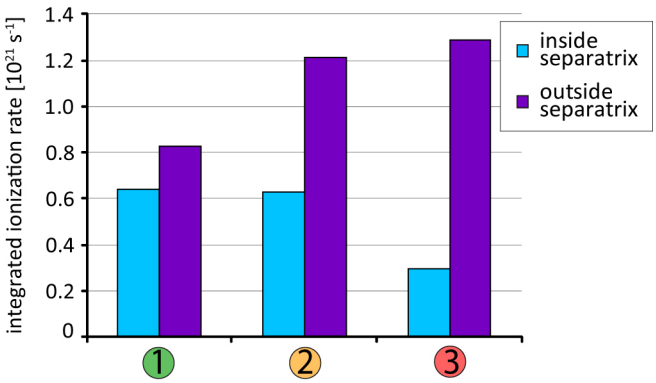

Figure 8.2.: Volume integrated ionization rate inside and outside of the separatrix, assuming poloidal and toroidal symmetry, for the cases calculated in Fig. 8.1.

effective fueling are constantly balanced. This process cannot be fully reconstructed by the simple model used here.

Caveats of this analysis are the one-dimensional model and the lack of detailed measurements of the electron density and temperature in the SOL plasma under HDL conditions. Two dimensional modeling by the SOLPS code package [54] shows for different plasma conditions a strong poloidal asymmetry of the fueling [53], which cannot be reproduced by KN1D. Nevertheless, the KN1D calculations indicate that the fueling and the location of the ionization are very sensitive in the density range where the HDL occurs, particularly in the presence of the SOL density plateau.

8.2. Increased energy losses

The second effect creating the four phases is the energy confinement reduction. This increased or additional energy loss channel becomes evident in the power balance of the plasma, when the total heating power is compared to the total loss power, which is the radiation plus the power deposition on the divertor target plates.

In figure 8.3, the power balance of the HDL discharge AUG #29810 is shown. The NBI losses in the SOL due to ionization outside the separatrix are up to 0.8 MW and are not shown here. At about 2 s, the total loss power, which consists of the radiated power and the power deposited on the divertor target plates, is around 90% of the heating power. About 10% of the heating power is expected to be deposited on the main chamber wall [11, 73], e.g. by ELMs, and is not measured. Thus, heating power and output power are roughly balanced. As the density is increasing towards the HDL, the loss power decreases at a constant heating power. At about 4.7 s, the power balance shows a discrepancy of 2.5 MW. This power is neither measured by the bolometers nor by the thermography observing the divertor target plates. The missing power must be deposited on the main chamber wall and, thus, is not included in the power balance.

The radiated power in the divertor and the power deposited on the target plates both

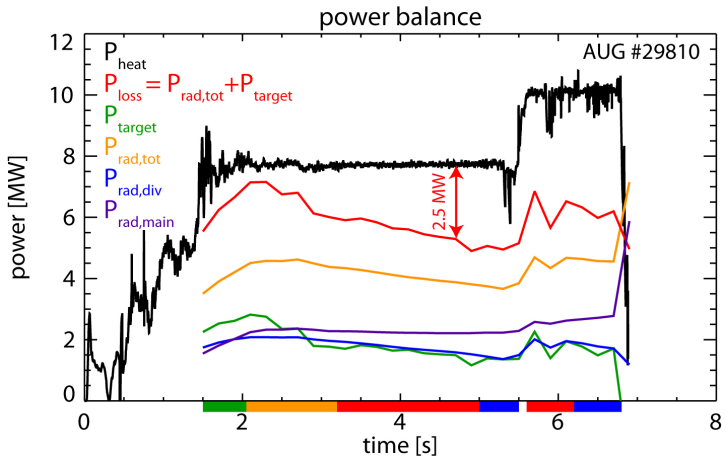

Figure 8.3.: Power balance of an HDL discharge (AUG #29810): Total heating power (P_{heat}, black) and total loss power (P_{loss}, red). The latter consists of the power deposition on divertor target plates (P_{target}, green) and the total radiated power ($P_{rad,tot}$, orange). The total radiated power can be divided into divertor radiated power ($P_{rad,div}$, blue) and main chamber radiated power ($P_{rad,main}$, purple). The radiated power is calculated from tomographic reconstructions. The four phases are indicated by the colorbar on the bottom. In the beginning 90% of the heating power is measured by either bolometry or thermography. Around 4.7 s, the power balance is off by about 2.5 MW.

decrease, but the radiated power in the main chamber stays constant, indicating that the core plasma does not change. Thus, the additional loss channel must be present at the edge of the plasma and must deposit the power directly on the main chamber walls.

In chapter 7 several mechanisms that were proposed to cause the HDL were refuted for the present dataset of full-W AUG. Most of these mechanisms were explanations of additional energy losses at high densities. We propose here another mechanism which might lead to the additional energy losses.

8.2.1. Filamentary transport

An increased radial energy transport can be caused by filaments in the SOL, so-called blobs [74]. Energy and particles are ejected from the confined plasma and form filaments in the SOL, which exhibit higher densities and temperatures than the surrounding plasma. These filaments are assumed to be generated at the outer midplane, where the unfavourable magnetic field curvature drives effectively instabilities. The ejected energy is then both conductively transported parallel to the magnetic field lines and propagating convectively with the filament radially outwards. The ratio of these two competing mechanisms determines if the energy transported by filaments is mainly transported to the divertor (parallel transport) or to the main chamber wall (radial transport). In cases with low densities and high temperatures, however, the conductive term dominates and

most of the energy flows into the divertor.

Inside the filament, the electrons and ions experience a charge separation by the diamagnetic drift in the inhomogeneous magnetic field. This creates an electric field, which on the one hand accelerates the filaments radially outwards by the $E \times B$ drift and on the other drives a compensating current in the filament parallel to the magnetic field lines. In [75] it is shown that the radial velocity and size of the filaments depend on the parallel closure condition of this current. For low densities, the current is closed by the divertor target plates through the plasma sheath. This condition changes drastically if the divertor goes into a partially detached state. The filament current has to be closed by an increased plasma resistivity, resulting in a higher electric field in the filament. Thus, the radial velocity increases strongly and the radial transport time to the main chamber wall becomes shorter than the parallel transport time scale to the divertor.

Such a change of the filamentary transport regime is observed in [76] at edge line averaged densities of $\langle n_{e,H-5} \rangle \approx 2.5 \cdot 10^{19}\,\mathrm{m}^{-3}$ for L-mode discharges in full-W AUG ($I_p = 0.8\,\mathrm{MA}$, $B_t = 2.5\,\mathrm{T}$, $P_{heat} = 0.8\,\mathrm{MW}$), when the divertor starts to detach. The HDL discharges are operated at same field and current but have a higher heating power (7.5 MW) and a higher density ($8 \cdot 10^{19}\,\mathrm{m}^{-3}$). The high radial SOL transport regime in L-mode described in [76] is accompanied by an increased density in the SOL, similar to the observed density plateau of the HDL discharges. The change of the regime coincides with the partial detachment of the outer divertor, which is also observed in the HDL discharges, though the density plateau in L-mode is by a factor of 3-4 lower than in the HDL discharges. An increase of radial filamentary transport at high densities is also measured at the Alcator C-Mod tokamak and proposed to be related to the L-mode density limit [77].

The SOL fluctuations could, so far, not be measured for the HDL discharges at AUG for technical reasons. The reciprocating probe cannot withstand the imposed heat loads when inserted into a plasma heated with several MW of power. A clear indication of the SOL filamentary transport in the HDL discharges was not found in the magnetic, Doppler reflectometry, AXUV or ECE-imaging [78] measurements. However, the X-point fluctuations shown in section 5.1.2 might be an indication of such a filamentary transport. The edge Thomson scattering measurements in figure 5.12 show a scatter in the electron density, which is around and below the SOL density plateau measured by the Li beam diagnostic. As discussed in section 5.2 this can be caused by filaments. In section 7.1 it is shown that the divertor is not completely detached but in a partially detached state, which is supposed to trigger of the fast radial filament propagation regime. In [77] it is predicted that this regime affects the power distribution between the divertor and main chamber, as it leads to increased losses to the main chamber wall, as observed in the HDL discharges.

ITER might operate in a similar regime. If also at ITER the fluctuations deposit 40% of the heating power, i.e. around 50 MW, on the main chamber walls, this would lead to an increase of power flux onto the blankets. These power fluxes might be quite localized at the outer midplane. A linear interpolation from the observations at AUG would lead

to an additional power deposition on the outer midplane structures of about 0.15 $\frac{\mathrm{MW}}{\mathrm{m}^2}$ localized on a poloidal spreading of about 5 m. This is below the design parameter of 1 $\frac{\mathrm{MW}}{\mathrm{m}^2}$. However, these values depend strongly on the geometry and the condition of the SOL plasma.

The observations mentioned above appear to be of the same origin. However, this change of the radial transport due to filaments does not directly explain the energy and confinement losses of the plasma. The increased radial transport can explain the deviation in the power balance, but why the filaments leave the plasma and enter the SOL in first place is still unknown. It is plausible to assume that a higher radial transport in the SOL leads also to a higher transport over the separatrix, but this is not yet shown. Nonetheless, in reference [79] an increase of the electron density and temperature fluctuations is reported for an increase of the edge line averaged density from $2 \cdot 10^{19}\,\mathrm{m}^{-3}$ to $6 \cdot 10^{19}\,\mathrm{m}^{-3}$, leading to an increased perpendicular heat diffusivity at the separatrix. Instabilities, which eject the energy out of the confined plasma, are usually driven by strong gradients. During the evolution of the HDL, the edge gradients of density and temperature relax rather than steepen. Thus, one does not expect additional instabilities to arise. The drive of the additional occurrence of instabilities in HDL discharges calls for further, more detailed investigations.

8.3. The coupling of the density evolution and the energy loss

To explain the evolution of the HDL according to the four phases, the nonlinear density evolution and the additional energy loss channel have to be coupled. Both set in at the same time, with the beginning of the degrading H-mode phase, and both end as soon as the L-mode is reached. The process which leads to the coupling is not yet revealed. We propose possible mechanisms which can lead to the coupling at these two points.

The onset of the fueling limit at the beginning of the degrading H-mode phase leads to an increased electron density in the SOL. This increased density triggers most probably the additional energy loss channel. The increased SOL density leads for example to an even further increased density in the divertor ($n_{e,div} = n^3_{e,midplane}$, [80]), which can trigger the detachment process. As shown above, this causes the regime of increased radial transport by filaments.

With the end of the breakdown phase, both effects end simultaneously. The pedestal is completely eroded. In sections 7.5 it is shown that the threshold of the $\mathrm{E_r}$ well depth might determine the transition to the L-mode. The sheared flow at the edge might not be sufficient any more to suppress turbulence. The additional loss channel might therefore be identified as the absence of the turbulence suppression, which is sustaining the H-mode confinement.

That the erosion of the pedestal also has an impact on the fueling is shown in figure 8.4. The ionization profile is calculated by the KN1D code with the same density profile for

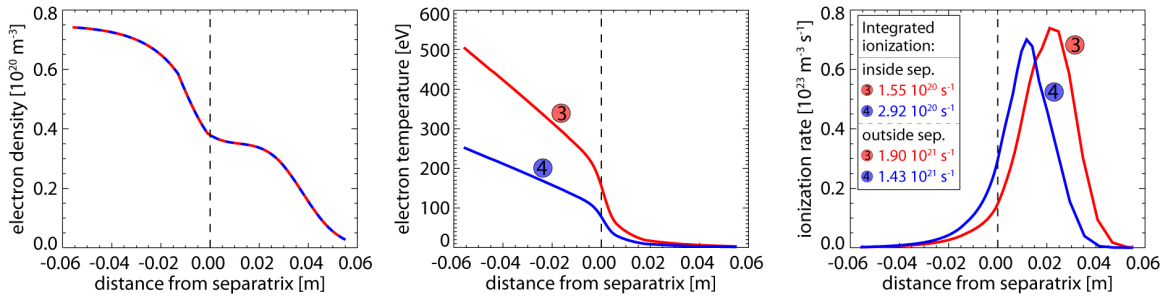

Figure 8.4.: Ionization rate (right) calculated with the KN1D code for a constant electron density (left) at two different electron temperatures (middle), corresponding to the beginning of the breakdown of the H-mode (red) and the L-mode phase (blue). The reduction of the temperature to L-mode like values increases the fueling inside the separatrix.

two different temperature profiles, corresponding to the beginning 3 and end 4 of the H-mode breakdown phase and the L-mode phase. By the reduction of the temperature, the ionization reduces by 25% outside the separatrix but increases by almost a factor of two inside the confined region. This can restore an effective fueling of the plasma. However, the shift of the ionization results from a continuous temperature reduction, thus one would expect a gradual change.

8.4. Comparison between full-C and full-W AUG

The four phases are also observed in full-C AUG, as presented in figure 5.5.

Nevertheless, in [18, 20, 65] the full detachment of the outer divertor is identified as the cause of the HDL. This is not necessarily a contradiction. In section 7.1 it is explained that the ionization front, which is moving towards the X-point due to the detachment, can create additional energy losses in the divertor. Thus, one might have a similar combination of the nonlinear density evolution and additional energy loss channel, which is creating the four phases. The density evolution might also be determined by the fueling limit, but the energy loss channel is caused by the detachment. Carbon as a wall material facilitates the detachment (see Sec. 7.1) and thus, such a loss channel might be dominant in full-C AUG whereas in full-W AUG the divertor detachment does not cause the HDL.

The fueling limit might, to first order, determine the density of the HDL since it is expected to be involved in the HDL in both full-C AUG and full-W AUG and the HDL occurs at about the same densities, as shown in chapter 6. Nevertheless, the parameter dependencies of the HDL density, i.e. the current and power dependence, changed with the wall material. This influence might result from the changed energy loss channel. The density of the full detachment shows almost no power dependence for carbon walls [15] whereas the onset of the detachment increases roughly with the square root of the heating power for tungsten walls [47].

The coupling of the fueling limit and the energy loss channel is straightforward in the case of the detachment. The electron density in the divertor is even further increased by the higher electron density in the SOL and the detachment is triggered. However, it is not known if the detachment also causes the degrading H-mode phase in full-C AUG due to the insufficient diagnosed divertor plasma.

8.5. Proposal for refined studies

The findings presented in this chapter do not rule out other additional mechanisms for the HDL, however, they do offer a new explanation for the observed evolution of the HDL. The combination of the fueling limit and the increased radial transport by filaments and their coupling could not be proven definitively. We suggest further steps in order to pinpoint the energy loss channel, the cause of the nonlinear density evolution and their coupling.

- Detailed measurements of the edge density are necessary to determine, if the edge density plateau is dominated by an average over the fluctuations or the steady background density.
- Fluctuation measurements with the reciprocating probe or fixed probes on the main chamber limiters are required to identify the regime of fast radial filament propagation in L- and H-mode. This has to be correlated with the four phases of the HDL and with divertor detachment measurements.
- A self-consistent, two-dimensional modeling of the HDL discharges, e.g. by the SOLPS code package, is necessary to verify the conclusions we draw out of the KN1D calculations. The charge exchange losses can then be assessed for the divertor region. The modeling can possibly also clarify the coupling of the two mechanisms.
- Measurements of the neutral particle flux originating from the pedestal region are needed to rule out the charge exchange losses in the main chamber and, thus, confirm the KN1D results.
- The high radial transport in the SOL is explained by radially fast propagating filaments. Further studies need to focus on the increased convective energy transport from the confined region into the SOL, i.e. whether it is caused by the increased radial SOL transport or itself causes the latter.
- In order to obtain further predictions of the HDL for ITER and DEMO it is necessary to compare the findings with other tokamaks. At JET with the ITER-like wall, two discharges were carried out so far in order to study the HDL with a metallic wall [21]. These, and possible further HDL discharges, need to be investigated with respect to the analysis presented here.
- An extension of the full-W AUG database with discharges at higher plasma currents is necessary to verify the weak current dependency of the HDL. If the HDL scaling deviates strongly from the Greenwald scaling for higher currents, it would have a major impact on the design of future tokamaks, such as ITER and DEMO.

9. Exceeding the H-mode density limit with centrally elevated density profiles

The Greenwald limit and the HDL are most likely determined by edge parameters. However, for present tokamaks, the density profiles of gas puffed discharges are inherently flat at high densities. This is caused by a correlation of the collisionality and the density peaking, which is discussed below. For flat profiles, the edge, core and line averaged density are inherently related to each other (see Eqs. 6.1-6.4). Thus, the density limits are correlated with the line averaged density. With centrally elevated density profiles, it is possible to disentangle these densities.

9.1. How to achieve centrally elevated profiles

In the analyzed data for full-W AUG, the plasma has a high collisionality, which is given by

$$\nu_{eff} \equiv 0.1 Z_{eff} \langle n_e \rangle R / \langle T_e \rangle^2 > 1 \quad [81], \tag{9.1}$$

where ν_{eff} is the effective collisionality, Z_{eff} the effective charge, $\langle n_e \rangle$ and $\langle T_e \rangle$ are the volume averaged values of electron density and temperature in $10^{19}\mathrm{m}^{-3}$ and keV, respectively, and R the major radius in m. Typically, the plasma is, at these collisionalities, in a regime where the core transport is dominated by ion temperature gradient modes (ITGs), which flatten the central density profile [14]. Future fusion devices, such as ITER or DEMO, will operate at a much lower collisionality ($\nu_{eff,ITER} \approx 0.2$) for similar densities. At these collisionalities, depending on the temperature profiles, the core turbulence is dominated by trapped electron modes (TEM) or in the transition between TEM to ITG, where a turbulent particle pinch leads to a peaking of the density profile [81].

For this reason, at present tokamaks such as AUG, a centrally elevated density at high densities can only be achieved by external means. Therefore, central fueling is necessary. This can be realized by the injection of frozen deuterium pellets into the plasma [82]. These pellets are injected into the plasma from the high field side with a velocity of up to 560 m/s and a repetition frequency of up to 70 Hz. The actual setup provides a maximum number of 96 pellets per discharge, each consisting of about $3.7 \cdot 10^{20}$ atoms. These pellets are depleted mainly inside the separatrix.

9.2. Experiments

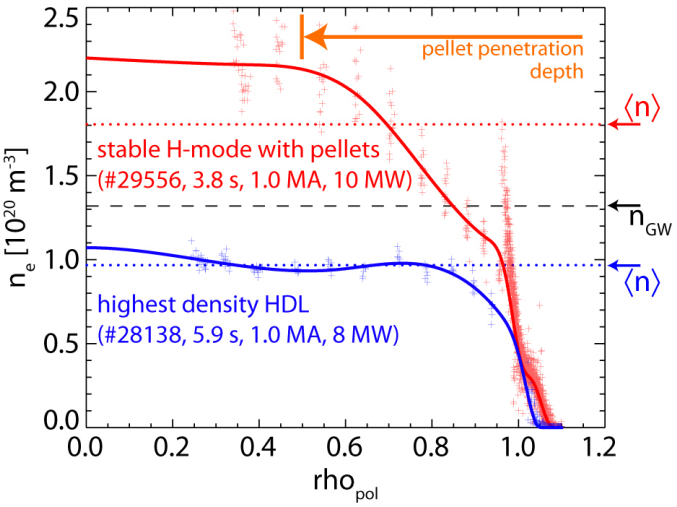

Figure 9.1.: Density profiles of the HDL discharge with the highest density and a pellet fueled H-mode discharge. The line averaged densities (H-1, dotted) and Greenwald density (dashed) are indicated. Note, that the plasma current of the two discharges differs.

In figure 9.1 the density profile of a gas puffed HDL discharge and a pellet fueled H-mode are compared. The gas puffed discharge exhibits a flat density profile and the line averaged density stays below the Greenwald density. With the pellet fueling, a centrally elevated density profile is achieved and the line averaged density exceeds the Greenwald density significantly, keeping the edge density well below n_{GW}. The density gradient in the core is restricted to the radial range of the pellet particle source.

The energy confinement time τ_E, which is defined by the ratio of the plasma stored energy and the heating power, stays constant for the pellet fueled discharge with and without pellets. The centrally increased density does not have an effect on the confinement. Note that the ITERH98P(y,2) scaling [55], which derives the H_{98} factor, contains a density dependence of $n_e^{-0.41}$ but does not include data at these high densities. In [82] it is shown that this density dependence is misleading for high densities, thus the comparison of the H-factor of the discharges is omitted here.

It was also attempted to achieve centrally elevated density profiles by pellet fueling in HDL discharges. However, the operation without cryo-pump combined with the use of pellets made the control of the neutral density not feasible. A back transition to L-mode is immediately triggered by the first few pellets. An investigation of the HDL with centrally elevated density profiles requires a higher number of pellets per discharge and is foreseen for future studies.

Several experiments show that the Greenwald limit is edge determined (e.g. JT-60 [83], DIII-D [84], Tore Supra [85]). Also, H-modes with centrally elevated density profiles

achieved Greenwald fractions above 1 (Fig. 9.1 or [82, 84]), while keeping a moderate confinement. In conclusion, the H-mode limit and the Greenwald limit are determined by edge parameters.

Future tokamak fusion devices will operate with lower collisionality and, therefore, exhibit intrinsically peaked density profiles [81]. Consequently, it is possible that these tokamaks operate in a stable H-mode regime at Greenwald fractions above 1.

10. Summary

The high confinement mode (H-mode) is the foreseen operational scenario for ITER and other future tokamaks. An H-mode plasma exhibits a region with increased gradients of electron and ion temperature and density at the edge, the so-called pedestal. The pedestal forms a turbulence suppressing edge transport barrier (ETB) and increases the energy and particle confinement of the plasma by about a factor of 2 with respect to the low confinement mode (L-mode).

It is desirable to maximize the central density of future fusion power plants in order to maximize the fusion power production. However, with increasing density, a back transition from the H-mode to the L-mode is observed. This H-mode density limit (HDL) occurs at line averaged densities on the order of, but below, the Greenwald density, which is an empirical limit for tokamak operation in L-mode.

Previous studies in tokamaks with carbon as the first wall material identified the full detachment of the divertor as the cause of the H-mode density limit. In the work presented here, the HDL is revisited at the ASDEX Upgrade tokamak, where the carbon wall was replaced by a full tungsten wall. The change of the wall material has a strong impact on the impurity content and the radiation characteristics of the edge plasma and, hence, also on the detachment process.

The bolometry, which measures the radiated power distribution of the plasma, is an indispensable diagnostic for these studies. Therefore, the absolutely calibrated foil bolometry and the fast AXUV diode bolometry and their analysis methods were extended, improved and further characterized during this thesis work.

At ASDEX Upgrade the H-mode density limit is achieved by so-called density ramp discharges. The neutral gas pressure in the experiment chamber is increased, and thus, also the plasma density increases, until the HDL is reached. The neutral gas pressure required for the HDL is achieved by reducing the pumping capacity of the vacuum chamber. This represents a non-standard operation of the experiment, which restricts the density control of the discharges and the measurement capability of several diagnostics.

In these gas ramp discharges, four distinct phases can be identified in the approach towards the HDL: a stable H-mode, a degrading H-mode, the breakdown of the H-mode and, finally, an L-mode. These four phases are quasi-stable, distinct plasma regimes, which are reproduced in all of the analyzed discharges, including previous AUG operational campaigns, for which the wall material was carbon. The phases are distinguished by their impact on the plasma stored energy and line averaged density. The evolution of the electron density and temperature profiles differ significantly in each of these phases.

- In the stable H-mode phase, the density increases and the stored energy is constant.

Density and temperature evolve along an isobaric line, the plasma pressure is constant.

- In the degrading H-mode phase, the electron density in the core saturates. A plateau of electron density evolves outside of the separatrix in the scrape-off layer (SOL). Meanwhile, an additional energy loss channel comes up, which decreases the stored energy and reduces the plasma pressure.
- In the breakdown of the H-mode, the plateau of density in the SOL also saturates at about half the pedestal top density, hence the overall radial electron density profile stays fixed. The temperature pedestal is fully eroded within this phase and thus leads to the final regime. This phase is defined as the actual HDL, since it exhibits the highest densities in H-mode.
- When the L-mode is reached, the stored energy stays constant and the density starts again to increase. Finally, the L-mode density limit is reached, which initiates a disruption.

Several mechansims which were proposed to cause the HDL are ruled out for the current set of ASDEX Upgrade experiments. In addition to all of the radiative energy loss mechanisms considered, also the complete detachment is proven not to be the cause of the HDL in the operation with tungsten walls. MARFEs, which are radiation instabilities, were also excluded as a possible cause of the HDL. However, they can lead to an H-L back transition in plasmas with significant impurity content.

Fluctuations around the X-point, which were first observed in the discharges dedicated to the HDL studies, might be a sign of increased transport at high densities. However, these fluctuations are not specific to the H-mode and are most likely correlated with the state of divertor detachment.

Measurements indicate that a threshold of the radial electric field well depth or of the power flux into the divertor, which aim to describe empirically the onset of the H-mode either locally or globally, determines the final transition back to L-mode. However, both quantities are significantly above the empirical threshold at the onset of the HDL.

We identify two effects. When combined, they create the four phases and lead to the HDL. On one side, there is a nonlinear density evolution, the so-called fueling limit. We propose that this is caused by a radial outward shift of the ionization profile. On the other side, an additional energy loss channel comes up. This is apparent in the power balance of the discharges. Approaching the HDL, up to 40% (instead of the typical 10%) of the heating power is deposited on the main chamber walls. The radial propagation of filaments in the SOL can create such radial convective losses. Their radial velocity depends on the boundary condition of the filament, i.e. the closing of the current loop inside the filament on the divertor target plates. This radically changes with the onset of partial detachment of the divertor and leads to an increase of the radial transport. This change of the SOL transport regime is also observed in L-mode discharges in ASDEX Upgrade and Alcator C-Mod.

The two mechanisms have to be coupled to each other in order to create the four observed phases. Most likely the increased density in the SOL leads to the coupling.

These findings do not rule out other additional mechanisms for the HDL, however, the reported effects offer a new explanation for the observed evolution of the HDL.

The four phases are also observed in the operation with carbon as the first wall material at ASDEX Upgrade. The comparison to the operation with tungsten walls reveals that the energy loss channel is most likely replaced by the full detachment of the divertor, which can also lead to energy losses at the pedestal. In the operation with carbon walls the complete detachment sets in earlier than in tungsten, possibly due to carbon radiation. This means that the energy loss due to the full detachment occurs before the energy loss channel, which is dominant in tungsten. The changed energy loss channel is also reflected in the parameter dependencies.

For the operation with carbon walls, no power dependence but a significant current dependence of the HDL density is observed. Although for both wall materials the density of the HDL is similar, the density with the tungsten wall depends only weakly on the plasma current and the safety factor, but is significantly increased with a higher heating power. This is attributed to the parameter dependencies of the changed energy loss mechanisms, i.e. of the complete detachment in the case of a carbon wall and the partial detachment in the case of a tungsten wall.

The shape of the plasma, i.e. the triangularity, has no influence on the density of the HDL. However, the transition from the stable H-mode to the degrading H-mode takes place at a higher density for a higher triangularity. Therefore, a higher performance is achieved with higher triangularity at relatively high densities. With higher triangularity also less neutral gas is necessary to achieve the same line averaged electron density, thus, the triangularity has a significant effect on the plasma fueling.

Finally, it is shown that the HDL and also the L-mode density limit are determined by edge parameters. Centrally elevated density profiles in H-modes are achieved with pellet fueling. The line averaged density of these discharges exceeds the Greenwald density by up to a factor of 2. The edge density, however, stays at typical values, and the H-modes have a moderate confinement. Future tokamaks will operate at lower collisionalities, which will lead to an intrinsic density peaking. Consequently, it is possible that these tokamaks will operate in a stable H-mode regime above the Greenwald limit.

10.1. Outlook

In order to pinpoint the two mechanisms which lead to the HDL, further experiments and analysis are suggested. Detailed measurements of the SOL plasma are needed in order to distinguish between the background density and the filaments in this region, to characterize the high density transport regime and, possibly, relate these findings to the four observed phases.

It has to be identified, whether the increased transport in the SOL creates the additional losses over the separatrix or whether it is a consequence of the latter. The convective losses lead to an increased power deposition on the main chamber wall, as it is seen in the power balance of the discharges. A more detailed study of the filaments is necessary in order to estimate if the power flux exceeds the material limits of the main chamber wall. This can possibly be done with probes in the main chamber limiter structures.

An important step in understanding the HDL can be achieved by a self-consistent, two-dimensional modeling of the HDL discharges, e.g. by the SOLPS code package. This might ascertain the mechanism of the fueling limit and clarify the role of charge exchange collisions.

For the extrapolation to future tokamaks, such as ITER, the analysis presented here needs first to be extended to JET, which requires a more extensive set of discharges than presently exists. This analysis needs to confirm if the combination of the same two effects leads to the HDL at JET. The current and size scaling of the individual effects (fueling limit and energy loss mechanism) need to be known rather than the overall scaling of the HDL in order to make any reasonable predictions for future machines.

However, it is shown, that a higher performance is achieved for high triangularity discharges, as they will be possible at ITER. Furthermore, ITER and other future tokamaks like DEMO will operate most likely with peaked density profiles and, thus, be able to exceed the Greenwald limit with a reasonable H-mode confinement.

Acknowledgements

I would like to thank everybody who helped and contributed to this work, supported and accompanied me during the last three years.

First of all, I would like to thank my academic supervisor Hartmut Zohm, who was always interested in my work and triggered the right ideas with his suggestions. Furthermore, I would like to thank very much my supervisors Thomas Eich and Arne Kallenbach, who made a powerful team for the supervision of my thesis, who supporting me with my questions, believing in my work and establishing me in the fusion community.

This work would not have been possible without the excellent support of the ASDEX Upgrade team. Special thanks goes to Josef Schweinzer, who was always open for discussions, helped me a lot in understanding the topic of the HDL and steered my studies into the right directions.

A big help for me as a humble physicist were the discussions with the divertor gang, Felix Reimold, Steffen Potzel, Marco Wischmeier, and with Daniel Carralero, Peter Lang and Elisabeth Wolfrum, who all contributed a significant part to this thesis. Also Ralph Dux, Thomas Pütterich, Louis Giannone, Hans Meister and Christoph Fuchs were always open for discussions and supported me from the physical and the technical side.

My deepest gratitude to Rachael McDermott, not only for her enduring patience in correcting everything I write in the most beautiful German English.

All our work would not be possible without the technicians and their daily endeavour to deal with our crazy ideas. Special thanks goes to Heinz Wolf, with whom it is a pleasure to work with and who always supports me from the technical side and the history of bolometry. I like to thank Wolfgang Zeidner for his sacrificing work and mental support. Many thanks to Michi Ebner, who makes almost everything possible, and to all the Gefäß-Mannschaft, Gabi Fröhlich, Flo Springer, Hans Henning and Günter Maier, and Klaus Sauerer, who always helped with any technical problem, private or work related. I thank Ludwig Kammerloher and the rest of the electronics group for their support and lessons in soldering. Thanks to the computer group, especially Helmut Blank and Andreas Lohs, for all their programming.

Thanks also to Gabi Dörsch and Anja Bauer, who are always there to help and cheer me up.

Many thanks for the friendship, all the support and the very nice last three years to Andreas Burckhart, Elli Viezzer, Rachael McDermott, my roomie Athina Kappatou, Felix Reimold, Steffen Potzel, Ben Geiger, Sina Fietz, Farbi Sommer, Marco Cavedon, Mike Dunne, Willy Willensdorfer, Thomas Pütterich, Bernhard Sieglin, Christian Vorpahl, Gregor Birkenmeier, Valentino Foit, Pietro Vincenzi, Tim Happel, Livia Casali, Hauke

Doerk, Philipp Schneider, Florian Penzel, Luis Guimarãis, Jurrian Boom, Diarmuid Curran, Sylvia Rathgeber, Leena Aho-Mantila, Tilman Lunt, Marco Sertoli, Bernhard Nold and Tobias Hartmann.

I thank Lisa for the deep friendship, all her help and support and all the nice discussions, dinners and breakfasts we had. I thank Tobi for a little bit of Swabian atmosphere at Alte Heide and not at least for my apartment. I thank Isabel for testing all the Munich restaurants with me and seeing all the movies and enjoying so many evenings together. I am grateful to all the Stuttgart people, not at least Daniel and Jessie, Patrick and Tine, Klaus and Rahel, Boris and Diana, Alex and Martina, Stefan and Sonja, Bobi and Wiltrud, Uli and Uli. I hope we will all stay in touch.

I thank Nico, Simon, Patrick, Meli, Magda and Anna for the long lasting friendships.

I most like to thank my parents and my family, who always believe in me, care for me, supported me all along the way and always welcome me at home.

Appendices

A. List of discharges for HDL studies

shot (full-W AUG)	time s	$\langle n_{e,H-1} \rangle$ m^{-3}	$\overline{n}_{e,H-5}$ m^{-2}	I_p MA	B_t T	q_{95}	P_{heat} MW	δ
26227	1.77	0.67	0.53	0.79	-2.53	5.87	**6.1**	0.24
26228	1.77	0.67	0.52	0.79	-2.53	5.85	**5.9**	0.24
26346	3.60	0.81	0.63	0.80	-2.51	**6.12**	8.0	0.23
26592	3.25	0.77	0.61	0.80	-2.53	6.03	7.8	0.23
26692	3.81	0.93	0.61	0.80	-1.70	**3.98**	7.9	0.24
26694	3.68	1.02	0.78	0.80	-1.45	**3.50**	8.1	0.23
26901	5.14	0.78	0.60	0.80	-2.51	**6.02**	7.6	0.24
26902	5.19	0.79	0.60	0.80	-2.51	6.01	**8.0**	0.24
27136	4.70	0.80	0.63	0.80	-2.47	5.96	8.4	0.24
27138	5.08	0.94	0.73	0.80	-2.47	6.06	**12.3**	0.24
27677	4.44	0.76	0.59	0.80	-2.44	5.96	**7.8**	0.24
27678	3.76	0.75	0.57	0.80	-2.44	5.93	7.8	0.23
28137	4.30	0.81	0.60	**0.60**	-1.60	5.03	7.9	0.26
28138	7.10	0.97	0.71	**1.00**	-2.67	4.95	8.3	0.24
28140	7.10	0.95	0.63	1.00	-2.67	4.95	7.9	0.25
28330	2.84	0.95	0.72	**1.00**	-2.66	5.04	7.9	0.24
28331	2.32	0.84	0.65	1.00	-2.66	5.00	7.7	0.24
28724	2.82	0.77	0.58	0.80	-2.16	**4.90**	7.4	0.26
28725	2.86	0.78	0.60	0.80	-2.16	4.92	7.5	0.26
28726	2.83	0.79	0.62	**0.80**	-2.16	4.92	7.6	0.25
28727	2.75	0.79	0.64	**0.80**	-2.15	**4.91**	7.8	0.24
28728	2.78	0.79	0.64	**0.80**	-2.16	4.93	7.7	0.24
28729	2.72	0.79	0.64	0.80	-2.16	4.93	7.7	0.24
29809	3.25	0.77	0.63	0.80	-2.51	**5.83**	**7.7**	0.25
29810	2.75	0.76	0.63	0.80	-2.52	**5.83**	7.6	**0.25**
29811	2.16	0.82	0.64	0.80	-2.51	5.61	7.9	**0.36**
29812	4.45	0.71	0.63	**0.60**	-1.63	5.18	7.8	0.26
29816	2.25	0.77	0.63	0.80	-2.52	5.50	7.8	**0.36**

Table A.1.: HDL discharges in full-W AUG, the bold written values indicate if the discharges were used in the scaling of the specific parameter (see Sec. 6)

shot (full-C AUG)	time s	$\langle n_{e,H-1} \rangle$ m^{-3}	$\overline{n}_{e,H-5}$ m^{-2}	I_p MA	B_t T	q_{95}	P_{heat} MW
7892	1.85	0.84	0.69	**1.00**	-2.03	**3.10**	**6.6**
8383	2.27	0.84	0.66	**0.80**	-2.02	**4.05**	**8.2**
9330	3.10	0.83	0.64	**0.80**	-2.12	**4.40**	**8.0**
10010	2.80	0.86	0.66	**0.80**	-2.02	**4.15**	**8.0**
10224	3.05	1.29	0.99	**1.20**	-2.53	3.40	6.6
11220	2.80	0.59	0.45	**0.60**	-1.97	5.45	5.3
13647	4.33	0.93	0.67	**0.80**	-1.98	**3.85**	**5.5**

Table A.2.: HDL discharges in full-C AUG used in this thesis, the bold written values indicate if the discharges were used in the scaling of the specific parameter (see Sec. 6)

B. Diagnostic setup of the AXUV diodes

To measure absolutely calibrated values of radiation losses, no optics are allowed between the detector and the light source (the plasma). Therefore, the cameras are installed directly in the vacuum vessel with a pinhole geometry. Each camera is equipped with one or more 16-channel AXUV arrays of the type AXUV16ELG by International Radiation Detectors Incorporated (IRD,Inc.) [34].

The actual layout consists of six pinhole cameras, which are observing the poloidal cross-section of the experiment from different positions (Fig. 3.13) and two cameras with parallel lines of sight (LOS), observing the edge plasma with a high spatial resolution (Fig. 3.16).

Five of the poloidal cameras are installed in sector 5 of AUG to cover one complete cross-section and allowing tomographic reconstruction of the poloidal radiation distribution. The camera D13 is situated in sector 13, toroidally 180° apart from the other cameras, with a similar geometry as the vertical camera in sector 5 (DVC) for toroidal asymmetry studies (e.g. [35]).

B.1. Diode characteristics

The diode bolometry aims to measure the total radiation using AXUV semiconductors from IRD [34]. Photons penetrate the diodes and create electron-hole pairs in the active region (n-p junction). The resulting photocurrent should be proportional to the incident radiation power. [31, 32]

The diodes offer a time resolution of less than 500 ns [33] while the actual setup has a time resolution of 5 µs.

The AXUV diodes are optimized to measure also VUV photons (2-200 eV), since usual diodes are not sensitive for these energies. However, they still have a reduced sensitivity in the VUV range. Despite this lack of sensitivity the diode response is linear for photon energies between 1 eV and 8 keV. Therefore, the diodes are suited for bolometric measurements. The wavelength dependent responsivity can be seen in Fig. B.1.

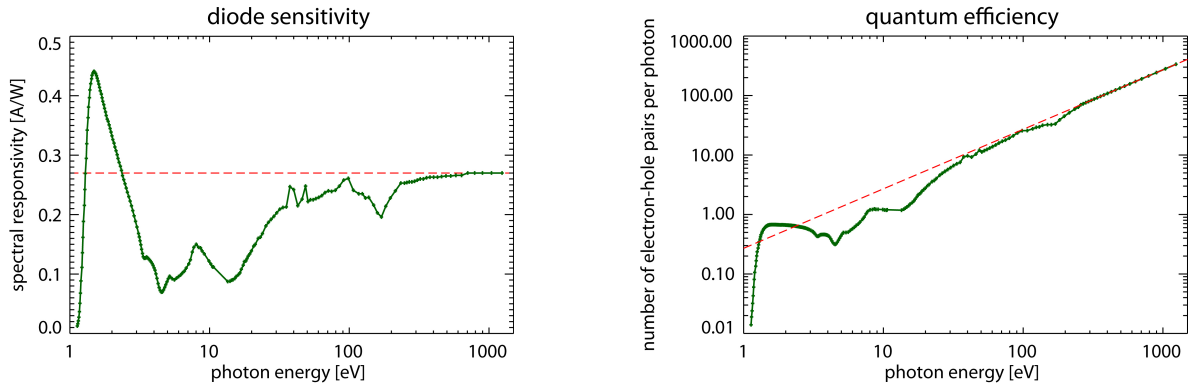

(a) **(b)**

Figure B.1.: Responsivity function (left) and quantum efficiency (right) of AXUV diodes (green, manufacturers specifications [34]) and the adopted calibration for measurements (red line), as discussed in Sec. C

B.2. Measurement and data acquisition

The electronic hardware of the diagnostic is based on the SIO system [36]. The diode bolometry was the first diagnostic to be fully implemented with this system and acts as functional prototype for future diagnostics.

Figure B.2 shows the data acquisition architecture of the diagnostic. The radiation emitted along one LOS is converted by the diode into a photocurrent. This current is fed through a shielded double-core cable to the measuring board (SIO PIPE3-ADC or SIO PIPE5-ADC). Each diode requires its own board. These boards consist of a transimpedance amplifier, two operational amplifiers, a 4^{th} order Bessel low-pass filter (200 kHz) and a 14-bit analog-to-digital converter (ADC).

The maximum sampling rate of this setup is 2 MHz, but the system is operated with 500 kHz, according to the 200 kHz hardware low-pass filter on the measuring boards.

The amplification of each channel can be remotely adjusted in between discharges, giving the system a high dynamic range. The highest current measurable by the boards is 15 mA and with the highest gain settings, signals as low as 50 nA can still be resolved. This covers a spectrum of more than 5 orders of magnitude.

The noise of the electronics is very low, mostly as low as the bit noise of the ADC. The main noise source for the measurement is pick up of other signals into the shielded cable that runs from the diodes to the electronics.

16 boards, enough for one diode array, can be mounted per rack. All of the measuring boards in a rack are serially read out by a pipe control and fiber link card, which communicates via fiber optics with the SIO-card. The SIO-card controls the system and acquires the data, which is then stored in the ASDEX Upgrade shot file system. The diode bolometry has dedicated computers to collect and store the data.

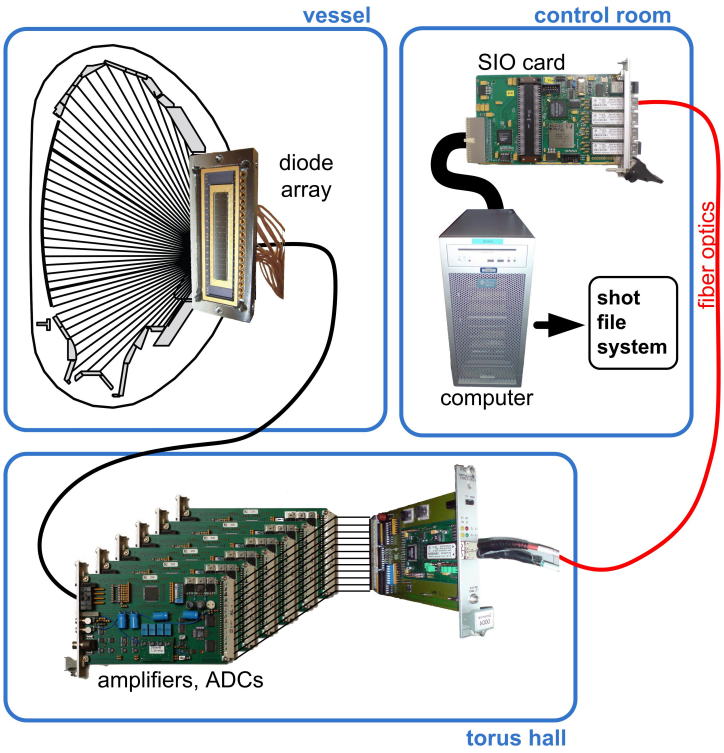

Figure B.2.: Schematic of the data acquisition system of the AXUV diode bolometry

C. Degeneration of AXUV diodes

A calibration for the diodes is needed in order to calculate the radiation power out of the measured current. The sensitivity function of the diodes is known (Fig. B.1), but wavelength dependent. A wavelength dependent calibration is not possible since the measured signal is integrated over all photon energies and the energy composition of the radiation is not known. Therefore, an overall calibration factor (quantum efficiency) of

$$QE = 0.27 \, \frac{\mathrm{A}}{\mathrm{W}} \tag{C.1}$$

is appointed to the diodes (indicated by the red line in Fig. B.1). This calibration does not account for the lower VUV sensitivity ($\sim$ 2-200 eV), therefore the measurement will underestimate this radiation.

The deviation between a diode measurement and the corresponding measurement of the absolutely calibrated foil bolometry (see Sec. 3.2) can be maximum a factor of 3 for this calibration.

Figure C.1 shows a profile of the measurements of the horizontal diode bolometry camera (DHC) and the corresponding foil camera (FHC). The diode measurements are scaled by a factor of 3.2 to match the foil measurements for LOS through the core region. Correction factors up to 20 are necessary to match the measurements in the upper and lower divertor, where mainly VUV radiation is present. This is more than can be expected from the initially lowered VUV sensitivity and indicates, that the sensitivity of the diodes is lowered. The diodes must have undergone a degradation.

The environment of a tokamak experiment contains several hazards for semiconductors such as intense VUV radiation, neutrons and hard X-rays. With respect to the use in VUV (EUV) lithography, sensitivity degeneration of different diode types due to VUV irradiation is already reported [37]. Nevertheless, these measurements cannot reconstruct the environment and radiation characteristics of a tokamak plasma.

C.1. Time scale of the degradation

All cameras were equipped with new diodes for the ASDEX Upgrade experimental campaign starting in November 2010. The change of the diode signal relatively to the foil bolometry was observed in detail.

The ratios of LOS doublets of diode and foil bolometry are plotted against the total incident radiation energy in figure 3.14. Starting from a ratio of around 0.9, which

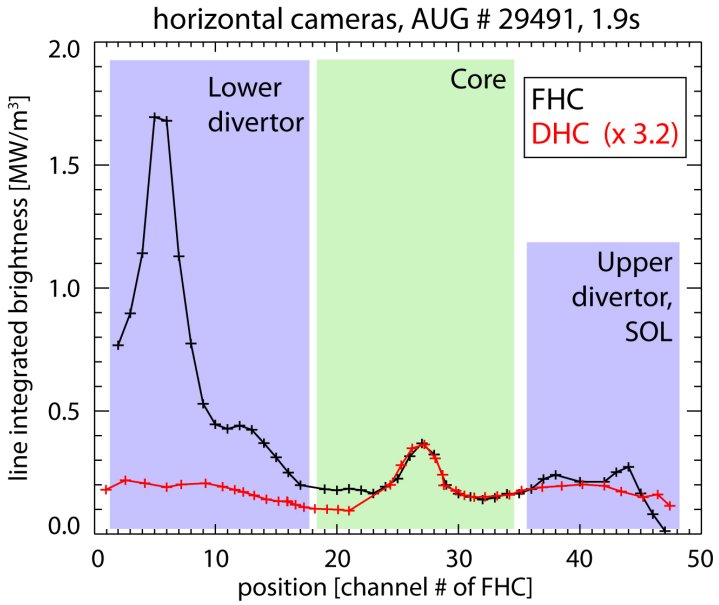

Figure C.1.: Comparison of the profiles measured by the FHC foil camera (black) and the DHC diode camera (red, scaled by a factor of 3.2). Correction factors over 3 are necessary for the lower and upper divertor regions. This indicates, that the given sensitivity (Fig. B.1) is not valid any more.

is expected from the initial calibration (see Fig. B.1), the diode sensitivity decreases strongly within 50 seconds of plasma operation, corresponding to the first 9 successful discharges of that experimental campaign. After around 300 seconds of plasma operation the sensitivity remains constant and the observed diode signals are a factor 2.5 lower than the foil measurements. The diode sensitivity does not change significantly for the next 1000 discharges ($\sim 3000\,\mathrm{s}$ of plasma operation) after this first degeneration.

This indicates a saturating behaviour of the degeneration of the AXUV diodes. A similar behaviour of other diode type is reported in [37].

Since the degradation just takes place within the first plasma discharges, the storage and installation of the diodes and the baking of the vacuum vessel can be excluded as degeneration causes. Neutron damage can be neglected since the neutron rates are very low ($< 10^{12}\,\frac{\mathrm{neutrons}}{\mathrm{s}}$) for these first discharges. High energetic photons ($E_{ph} \gg 100\,\mathrm{eV}$) can also be excluded, since also diodes degenerated, which were only exposed to lower photon energies.

This suggests that radiation, especially VUV radiation, is the cause of the degeneration. VUV radiation is absorbed in the passive top layer of the diode and the photo current is created by surface effects. The observation of figure 3.14 indicates, that the top surface depletes rapidly due to the VUV radiation and cannot recover. As soon as the surface is fully depleted, the sensitivity would not change significantly, resulting in the saturating degeneration as observed. The effect of the improved VUV sensitivity of the AXUV

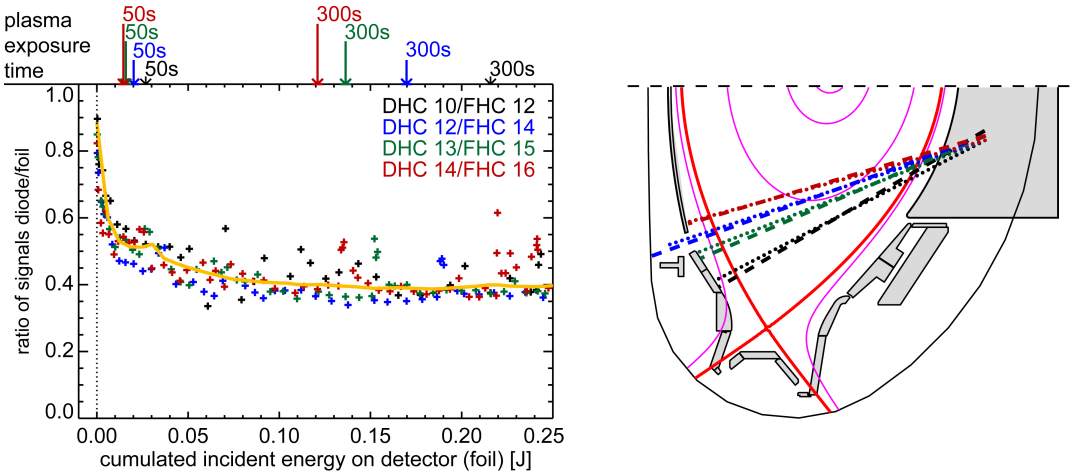

Figure C.2.: Left side: Discharge-averaged ratio of the diode and the foil measured signal of 4 LOS doublets plotted over the integrated incident radiation power. Right side: Poloidal cross-section of ASDEX Upgrade indicating the positions of the observed LOS of foil (dashed) and diode (dotted) bolometry

diodes would be canceled and the spectral sensitivity would change.

The fast degeneration of the diodes is observed for all diode channels and it is mainly dependent on the total incident radiation. If this is an effect of the overall radiation or only VUV radiation cannot be determined from the measured data, since the degradation takes place on a very short time scale.

C.2. Sensitivity after degradation

The previous section showed that diodes undergo a strong degeneration. Since the sensitivity seems to stay constant after a short while, one can recalibrate the diode signals using the degenerated sensitivity in order to retrieve useful data.

Several diodes, which were installed for one campaign (>1600 discharges, 4800 seconds plasma operation) at different positions in the vacuum vessel, have been calibrated by the Physikalisch-Technische Bundesanstalt (PTB) in Berlin. The spectral responsivity of the used diodes was measured at the synchrotron BESSY for photon energies between 50 eV and 1600 eV [86, 87]. A calibration for VUV light with photon energies below 50 eV was not possible.

In figure 3.15 the initial responsivity (blue line) is compared to the measurement selected degraded diodes. Most of the diodes show the same degenerated responsivity even though they were installed at diverse positions in the torus and were observing various regions. These diodes show the same sensitivity even though they were exposed to different fluxes of neutrons and photons and different photon energies. This is explained by the saturating degeneration.

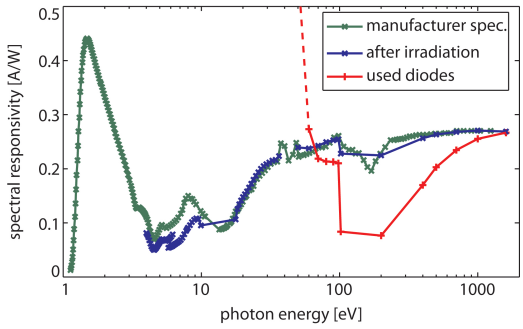

Figure C.3.: Diode responsivity measurements of the PTB: Averaged degenerated responsivity (red), initial responsivity (green, [34]) and responsivity after irradiation with 70-100 eV photons. A more detailed picture can be seen in 3.15

The diodes from one array (dashed lines in Fig. 3.15) were strongly damaged and therefore the increased dark current and its fluctuations did not allow detailed measurements.

While the responsivity to high energy photons (>500 eV) and photons of 70-100 eV is only weakly decreasing, there is a strong degradation between 100 eV and about 300 eV. The increase of responsivity below 70 eV is a spurious signal explained by the large error bars of the measurements at low photon energies.

The measurements at the PTB included an irradiation of new diodes with photons of an energy of 70-100 eV to estimate the contribution of this energy range to the degradation. This irradiation had an overall power deposition of 0.9 $\frac{\mathrm{J}}{\mathrm{mm}^2}$, much higher than the total power deposition during one campaign at ASDEX Upgrade.

Figure C.3 compares the responsivity of a new (green), irradiated (blue) and previously installed diode (red). The sensitivity of the controlled irradiated diode did not change significantly above 10 eV and lowered slightly between 4-10 eV. In comparison to the measurements of the installed diodes, the observed damage cannot be caused by the photon energies of the irradiation.

There are several indications that the sensitivity in the VUV range is strongly reduced, even though it was not measurable. The controlled irradiated diodes show a reduction in this range, therefore one can assume that the more strongly degenerated diodes, which were previously installed, are affected severely. In addition, the comparison to foil bolometers (see Sec. 3.2) show a stronger deviation for LOS which have a higher contribution of VUV light.

Overall, there is a strong decrease of sensitivity for VUV radiation (~3-15 eV) and for photons between about 100-300 eV. The sensitivity for visible light, 30-100 eV and above 300 eV is only marginally affected. The diodes remain sensitive for these three radiation bands. The observed degradation is neither caused by neutrons nor by photons of 70-100 eV or above several hundred eV. It appears that the main harm for the diodes is radiation in the VUV range, however, photon energies of about 100-500 eV cannot definitively be excluded.

D. Poloidal tracking of X-point fluctuations

The X-point fluctuations (Sec. 5.1.2) consist of radiating filaments. These filaments can be followed by correlating neighboring channels of AXUV cameras within short time windows and thus, the time shift for maximum correlation can be found.

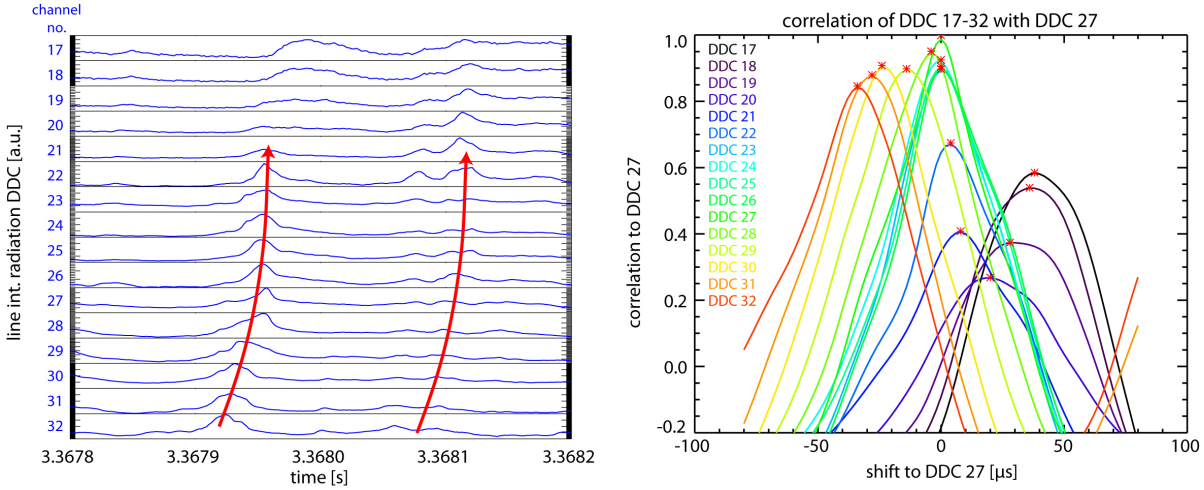

Figure D.1.: Movement of the filaments seen with the camera DDC looking from bottom through the X-point region. The red arrows mark the movement of two of the filaments. On the right side the correlations of the whole array with one of its array is shown. The maximum of this correlation is set as filament delay which is plotted in figure D.2

By using correlations of several cameras observing the X-point region, the movement of the filaments can be distinguished as shown in figure D.2. The DLX and DHC camera show that the filaments are moving away from the X-point, however, the DDC camera shows a contradictory movement. In order to resolve this, a more detailed analysis is necessary.

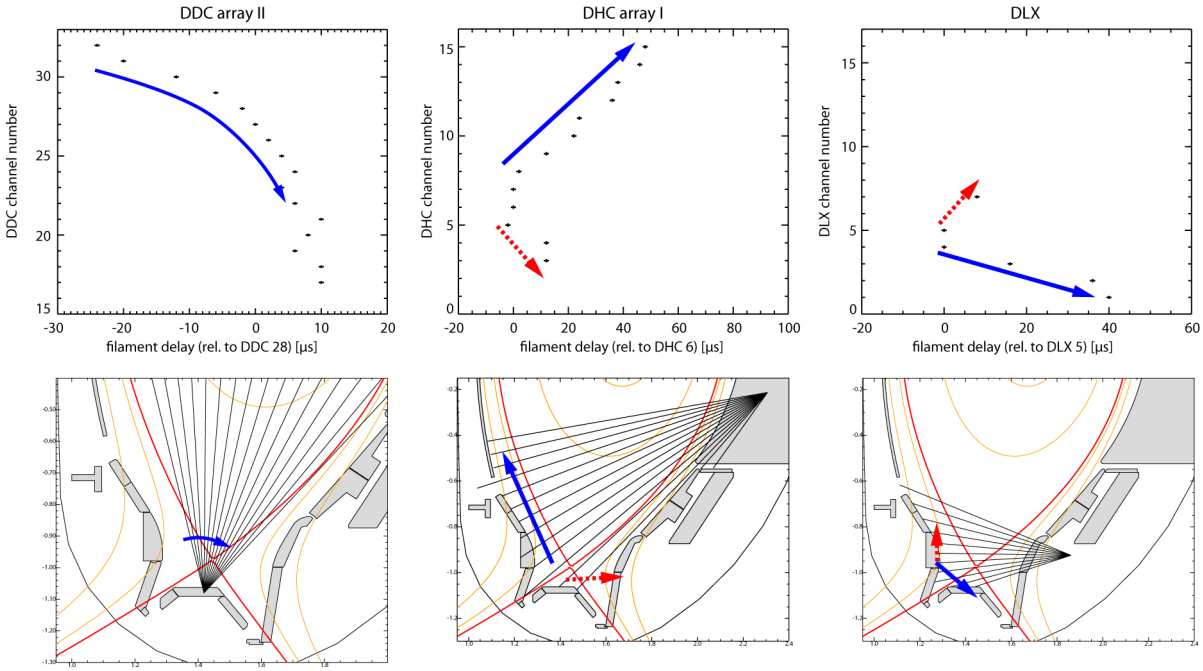

Figure D.2.: Movement of the filaments detected by correlation of AXUV channels within single cameras. The cameras DHC and DLX show a movement away from the X-point, the camera DDC a movement towards the X-point.

E. Bibliography

[1] Association EURATOM-CEA Commissariat à l'Energie Atomique. http://www-fusionmagnetique.cea.fr.

[2] F. Wagner, G. Becker, K. Behringer, D. Campbell, et al. Regime of improved confinement and high beta in neutral-beam-heated divertor discharges of the ASDEX tokamak. *Phys. Rev. Lett.*, 49(19):1408–1412, Nov 1982.

[3] M. Greenwald, J.L. Terry, S.M. Wolfe, S. Ejima, et al. A new look at density limits in tokamaks. *Nuclear Fusion*, 28(12):2199, 1988.

[4] V. Mertens, K. Borrass, J. Gafert, M. Laux, J. Schweinzer, and ASDEX Upgrade Team. Operational limits of ASDEX Upgrade H-mode discharges in the new closed divertor-II configuration. *Nuclear Fusion*, 40(11):1839, 2000.

[5] H. Matsumoto, T. Ogawa, H. Tamai, K. Odajima, et al. H-mode phenomena during ICRF heating on JFT-2M. *Nuclear Fusion*, 27(7):1181, 1987.

[6] U Stroth, P Manz, and M Ramisch. On the interaction of turbulence and flows in toroidal plasmas. *Plasma Physics and Controlled Fusion*, 53(2):024006, 2011.

[7] E. Viezzer, T. Pütterich, G.D. Conway, R. Dux, et al. High-accuracy characterization of the edge radial electric field at ASDEX Upgrade. *Nuclear Fusion*, 53(5):053005, 2013.

[8] P. Sauter, T. Pütterich, F. Ryter, E. Viezzer, et al. L- to H-mode transitions at low density in ASDEX Upgrade. *Nuclear Fusion*, 52(1):012001, 2012.

[9] T. Happel, G. D. Conway, P. Hennequin, C. Honor´e, et al. The optimized steerable W-band Doppler reflectometer on ASDEX Upgrade: possibilities and issues. In *Proc. 11th International Reflectometry Workshop*, 2013.

[10] A Herrmann. Overview on stationary and transient divertor heat loads. *Plasma Physics and Controlled Fusion*, 44(6):883, 2002.

[11] A Herrmann, T Eich, V Rohde, C J Fuchs, J Neuhauser, and ASDEX Upgrade team. Power deposition outside the divertor in ASDEX Upgrade. *Plasma Physics and Controlled Fusion*, 46(6):971, 2004.

[12] T. Pütterich, R. Dux, M.A. Janzer, and R.M. McDermott. ELM flushing and impurity transport in the H-mode edge barrier in ASDEX upgrade. *Journal of Nuclear Materials*, 415(1, Supplement):S334 – S339, 2011. Proceedings of the 19th International Conference on Plasma-Surface Interactions in Controlled Fusion.

[13] Martin Greenwald. Density limits in toroidal plasmas. *Plasma Physics and Controlled Fusion*, 44(8):R27, 2002.

[14] C. Angioni, R. M. McDermott, F. J. Casson, E. Fable, et al. Intrinsic toroidal

rotation, density peaking, and turbulence regimes in the core of tokamak plasmas. *Phys. Rev. Lett.*, 107:215003, Nov 2011.

[15] V. Mertens, M. Kaufmann, J. Neuhauser, J. Schweinzer, et al. High density operation close to greenwald limit and H-mode limit in ASDEX Upgrade. *Nuclear Fusion*, 37(11):1607, 1997.

[16] F Ryter, M Alexander, J C Fuchs, O Gruber, et al. H-Mode operating regimes and confinement in ASDEX-Upgrade. *Physica Scripta*, 51(5):643, 1995.

[17] F Ryter, K Buchl, C Fuchs, O Gehre, et al. H-mode results in ASDEX Upgrade. *Plasma Physics and Controlled Fusion*, 36(7A):A99, 1994.

[18] K. Borrass, A. Loarte, C.F. Maggi, V. Mertens, et al. Recent H-mode density limit studies at JET. *Nuclear Fusion*, 44(7):752, 2004.

[19] F. Ryter, S.K. Rathgeber, L. Barrera Orte, M. Bernert, et al. Survey of the H-mode power threshold and transition physics studies in ASDEX Upgrade. submitted to Nuclear Fusion, 2013.

[20] K. Borrass, R. Schneider, and R. Farengo. A scrape-off layer based model for hugill-greenwald type density limits. *Nuclear Fusion*, 37(4):523, 1997.

[21] A. Huber, S. Brezinsek, M. Groth, P.C. de Vries, et al. Impact of the ITER-like wall on divertor detachment and on the density limit in the JET tokamak. *Journal of Nuclear Materials*, 438, Supplement(0):S139 – S147, 2013. Proceedings of the 20th International Conference on Plasma-Surface Interactions in Controlled Fusion Devices.

[22] L. Giannone, D. Queen, F. Hellman, and J. C. Fuchs. Prototype of a radiation hard resistive bolometer for ITER. *Plasma Physics and Controlled Fusion*, 47(12):2123, 2005.

[23] H. Meister, T. Eich, N. Endstrasser, L. Giannone, et al. Optimization of a bolometer detector for ITER based on Pt absorber on SiN membrane. *Review of Scientific Instruments*, 81(10):10E132, 2010.

[24] K. F. Mast, J. C. Vallet, C. Andelfinger, P. Betzler, H. Kraus, and G. Schramm. A low noise highly integrated bolometer array for absolute measurement of VUV and soft X radiation. *Review of Scientific Instruments*, 62(3):744–750, 1991.

[25] L. Giannone, K. Mast, and M. Schubert. Derivation of bolometer equations relevant to operation in fusion experiments. *Review of Scientific Instruments*, 73(9):3205–3214, 2002.

[26] Christoph Fuchs, K. F. Mast, A. Herrmann, K. Lackner, and ASDEX Upgrade Team. Twodimensional reconstruction of the radiation power density in ASDEX upgrade. *Europhysics Conference Abstracts (Proc. of the 21th EPS Conference on Controlled Fusion and Plasma Physics, Montpellier, 1994*, 18B:1308–1311, 1994.

[27] D. Zhang, R. Burhenn, R. Koenig, L. Giannone, et al. Design criteria of the bolometer diagnostic for steady-state operation of the W7-X stellarator. *Review of Scientific Instruments*, 81(10):10E134, 2010.

[28] D. Wagner, F. Leuterer, A. Manini, F. Monaco, et al. The new multifrequency

electron cyclotron resonance heating system for ASDEX Upgrade. *Fusion Science and Technology*, 52(2):313–320, 2007. Technical Paper / Electron Cyclotron Wave Physics, Technology, and Applications.

[29] Bernhard Reiter. *Radiative Response on Massive Noble Gas Injection For Runaway Suppression in Disruptive Plasmas*. PhD thesis, LMU München, 2010.

[30] Matthias Bernert. Bolometry with diodes at the tokamak ASDEX Upgrade. Master's thesis, TU München, 2010.

[31] R. Korde, J.S. Cable, and L.R. Canfield. One gigarad passivating nitrided oxides for 100% internal quantum efficiency silicon photodiodes. *Nuclear Science, IEEE Transactions on*, 40(6):1655–1659, Dec 1993.

[32] E. M. Gullikson, R. Korde, L. R. Canfield, and R. E. Vest. Stable silicon photodiodes for absolute intensity measurements in the VUV and soft X-ray regions. *Journal of Electron Spectroscopy and Related Phenomena*, 80:313 – 316, 1996. Proceedings of the 11th International Conference on Vacuum Ultraviolet Radiation Physics.

[33] Raj Korde. *Manual: AXUV/SXUV/UVG*. International Radiation Detectors, Inc., 2010.

[34] International Radiation Detectors, Inc. 2527 West 237th Street Unit A, Torrance, CA 90505-5243, [online] http://www.ird-inc.com.

[35] G. Pautasso, Y. Zhang, B. Reiter, L. Giannone, et al. Contribution of ASDEX upgrade to disruption studies for ITER. *Nuclear Fusion*, 51(10):103009, 2011.

[36] K. Behler, H. Blank, A. Buhler, R. Cole, et al. Real-time standard diagnostic for ASDEX Upgrade. *Fusion Engineering and Design*, 85(3 - 4):313 – 320, 2010. Proceedings of the 7th IAEA Technical Meeting on Control, Data Acquisition, and Remote Participation for Fusion Research.

[37] P Kuschnerus, H Rabus, M Richter, F Scholze, L Werner, and G Ulm. Characterization of photodiodes as transfer detector standards in the 120 nm to 600 nm spectral range. *Metrologia*, 35(4):355–362, 1998.

[38] P Vincenzi. Edge plasma emissivity profile reconstruction by forward modelling of diode bolometer signals at ASDEX Upgrade. Master's thesis, University of Padova, Department of Physics and Astronomy "G. Galilei", 2012.

[39] W Schneider, P.J McCarthy, K Lackner, O Gruber, et al. ASDEX Upgrade MHD equilibria reconstruction on distributed workstations. *Fusion Engineering and Design*, 48(1-2):127 – 134, 2000.

[40] A. Mlynek, G. Schramm, H. Eixenberger, G. Sips, et al. Design of a digital multi-radian phase detector and its application in fusion plasma interferometry. *Review of Scientific Instruments*, 81(3):033507, 2010.

[41] K McCormick, S Fiedler, G Kocsis, J Schweinzer, and S Zoletnik. Edge density measurements with a fast Li beam probe in tokamak and stellarator experiments. *Fusion Engineering and Design*, 34-35(0):125 – 134, 1997. Fusion Plasma Diagnostics.

[42] H. Murmann, S. Götsch, H. Röhr, H. Salzmann, and K. H. Steuer. The thomson

scattering systems of the ASDEX Upgrade tokamak. *Review of Scientific Instruments*, 63(10):4941–4943, 1992.

[43] B Kurzan, M Jakobi, H Murmann, and ASDEX Upgrade Team. Signal processing of thomson scattering data in a noisy environment in ASDEX Upgrade. *Plasma Physics and Controlled Fusion*, 46(1):299, 2004.

[44] H J Hartfuss, T Geist, and M Hirsch. Heterodyne methods in millimetre wave plasma diagnostics with applications to ECE, interferometry and reflectometry. *Plasma Physics and Controlled Fusion*, 39(11):1693, 1997.

[45] S K Rathgeber, L Barrera, T Eich, R Fischer, et al. Estimation of edge electron temperature profiles via forward modelling of the electron cyclotron radiation transport at ASDEX Upgrade. *Plasma Physics and Controlled Fusion*, 55(2):025004, 2013.

[46] G F Matthews. Tokamak plasma diagnosis by electrical probes. *Plasma Physics and Controlled Fusion*, 36(10):1595, 1994.

[47] S. Potzel. *Experimental classification of divertor detachment*. PhD thesis, Universität Bayreuth, Fakultät für Mathematik, Physik und Informatik, 2012.

[48] P. Sauter. Development of a monte-carlo code to understand the ASDEX pressure gauge performance. Master's thesis, LMU München, 2008.

[49] T. Happel. *Doppler Reflectometry in the TJ-II Stellarator: Design of an Optimized Doppler Reflectometer and its Application to Turbulence and Radial Electric Field Studies*. PhD thesis, Universidad Carlos III de Madrid, Departamento de Física, 2010.

[50] E. Viezzer, T. Pütterich, R. Dux, R. M. McDermott, and the ASDEX Upgrade Team. High-resolution charge exchange measurements at ASDEX Upgrade. *Review of Scientific Instruments*, 83(10):103501, 2012.

[51] B. Streibl, S. Deschka, O. Gruber, B. Jüttner, et al. In-vessel cryo pump for ASDEX Upgrade divertor II. In C. Varandas and F. Serra, editors, *Fusion Technology 1996*, pages 427 – 430. Elsevier, Oxford, 1997.

[52] Brian LaBombard. KN1D: A 1-D space, 2-D velocity, kinetic transport algorithm for atomic and molecular hydrogen in an ionizing plasma. Technical Report PSFC/RR-01-3, PSFC Report, MIT, Boston, USA, 2001.

[53] M Groth, G D Porter, T D Rognlien, S Wiesen, et al. Poloidal distribution of recycling sources and core plasma fueling in DIII-D, ASDEX Upgrade and JET L-mode plasmas. *Plasma Physics and Controlled Fusion*, 53(12):124017, 2011.

[54] R. Schneider, X. Bonnin, K. Borrass, D. P. Coster, et al. Plasma edge physics with B2-Eirene. *Contributions to Plasma Physics*, 46(1-2):3–191, 2006.

[55] ITER Physics Expert Group on Confinement, Transport, ITER Physics Expert Group on Confinement Modelling, Database, and ITER Physics Basis Editors. Chapter 2: Plasma confinement and transport. *Nuclear Fusion*, 39(12):2175, 1999.

[56] S. Potzel, M. Wischmeier, M. Bernert, R. Dux, H.W. Müller, and A. Scarabosio. Characterization of the fluctuating detachment state in ASDEX upgrade. *Journal of Nuclear Materials*, 438, Supplement(0):S285 – S290, 2013. Proceedings of the

20th International Conference on Plasma-Surface Interactions in Controlled Fusion Devices.

[57] W Suttrop, V Mertens, H Murmann, J Neuhauser, J Schweinzer, and ASDEX-Upgrade Team. Operational limits for high edge density H-mode tokamak operation. *Journal of Nuclear Materials*, 266-269(0):118 – 123, 1999.

[58] H Zohm. Edge localized modes (ELMs). *Plasma Physics and Controlled Fusion*, 38(2):105, 1996.

[59] S. Potzel, M. Wischmeier, M. Bernert, R. Dux, et al. On the fluctuating detachment state at ASDEX Upgrade. *Europhysics Conference Abstracts (Proc. of the 40th EPS Conference on Controlled Fusion and Plasma Physics, Helsinki, 2013*, 37:P1.133, 2013.

[60] A Kallenbach, R Dux, H-S Bosch, K Büchl, et al. Radiative boundary discharges with impurity injection and the H - L transition in ASDEX Upgrade. *Plasma Physics and Controlled Fusion*, 38(12):2097, 1996.

[61] B. Esposito, G. Granucci, M. Maraschek, S. Nowak, et al. Disruption avoidance by means of electron cyclotron waves. *Plasma Physics and Controlled Fusion*, 53(12):124035, 2011.

[62] J. Stober, O. Gruber, V. Mertens, F. Ryter, et al. Dependence of confinement and transport on triangularity in ASDEX upgrade. *Europhysics Conference Abstracts (Proc. of the 26th EPS Conference on Controlled Fusion and Plasma Physics, Maastricht, 1999*, 23J:1401–1404, 1999.

[63] G. Saibene, L.D. Horton, R. Sartori, B. Balet, et al. The influence of isotope mass, edge magnetic shear and input power on high density ELMy H modes in JET. *Nuclear Fusion*, 39(9):1133, 1999.

[64] T H Osborne, J R Ferron, R J Groebner, L L Lao, et al. The effect of plasma shape on H-mode pedestal characteristics on DIII-D. *Plasma Physics and Controlled Fusion*, 42(5A):A175, 2000.

[65] K. Borrass, J. Lingertat, and R. Schneider. A scrape-off layer based density limit for JET ELMy H-modes. *Contributions to Plasma Physics*, 38(1-2):130–135, 1998.

[66] T. Pütterich, R. Neu, R. Dux, A.D. Whiteford, et al. Calculation and experimental test of the cooling factor of tungsten. *Nuclear Fusion*, 50(2):025012, 2010.

[67] H. P. Summers. *ADAS User Manual 2.6*. The ADAS Project, 2004.

[68] B. Lipschultz, B. LaBombard, E.S. Marmar, M.M. Pickrell, et al. Marfe: an edge plasma phenomenon. *Nuclear Fusion*, 24(8):977, 1984.

[69] Y R Martin, T Takizuka, and the ITPA CDBM H-mode Threshold Database Working Group. Power requirement for accessing the H-mode in ITER. *Journal of Physics: Conference Series*, 123(1):012033, 2008.

[70] C.F. Maggi, G. Calabro, E. Delabie, M. Groth, et al. The H-mode threshold in JET with the ITER-like wall. *Europhysics Conference Abstracts (Proc. of the 39th EPS Conference on Controlled Fusion and Plasma Physics, Stockholm, 2012*, 36F:O3.108, 2012.

[71] A Burckhart, E Wolfrum, R Fischer, K Lackner, H Zohm, and the ASDEX Upgrade Team. Inter-ELM behaviour of the electron density and temperature pedestal in ASDEX Upgrade. *Plasma Physics and Controlled Fusion*, 52(10):105010, 2010.

[72] R. Bartiromo, G. Bracco, M. Brusati, G. Grosso, et al. Design and calibration of the JET neutral particle analyzer. *Review of Scientific Instruments*, 58(5):788–795, 1987.

[73] T. Eich, A. Herrmann, G. Pautasso, P. Andrew, et al. Power deposition onto plasma facing components in poloidal divertor tokamaks during type-i ELMs and disruptions. *Journal of Nuclear Materials*, 337 - 339(0):669 – 676, 2005. PSI-16.

[74] D. A. D'Ippolito, J. R. Myra, and S. J. Zweben. Convective transport by intermittent blob-filaments: Comparison of theory and experiment. *Physics of Plasmas*, 18(6):060501, 2011.

[75] J. R. Myra, D. A. Russell, and D. A. D'Ippolito. Collisionality and magnetic geometry effects on tokamak edge turbulent transport. i. a two-region model with application to blobs. *Physics of Plasmas*, 13(11):112502, 2006.

[76] D. Carralero, G. Birkenmeier, H.W. Müller, P. Manz, et al. Influence of resistivity on filamentary transport in the SOL of ASDEX Upgrade. *Europhysics Conference Abstracts (Proc. of the 40th EPS Conference on Controlled Fusion and Plasma Physics, Helsinki, 2013*, 37:O4.108, 2013.

[77] B. LaBombard, R. L. Boivin, M. Greenwald, J. Hughes, et al. Particle transport in the scrape-off layer and its relationship to discharge density limit in Alcator C-Mod. *Physics of Plasmas*, 8(5):2107–2117, 2001.

[78] I. G. J. Classen, J. E. Boom, W. Suttrop, E. Schmid, et al. 2D electron cyclotron emission imaging at ASDEX Upgrade (invited). *Review of Scientific Instruments*, 81(10):10D929, 2010.

[79] B Kurzan, C Fuchs, A Scarabosio, B D Scott, and ASDEX Upgrade Team. Scale lengths of inter-ELM fluctuations in the pedestal of ASDEX Upgrade. *Plasma Physics and Controlled Fusion*, 51(6):065009, 2009.

[80] Peter C Stangeby. *The Plasma Boundary of Magnetic Fusion Devices*. Institute of Physics Publishing, Bristol and Philadelphia, 2000.

[81] C Angioni, E Fable, M Greenwald, M Maslov, et al. Particle transport in tokamak plasmas, theory and experiment. *Plasma Physics and Controlled Fusion*, 51(12):124017, 2009.

[82] P.T. Lang, W. Suttrop, E. Belonohy, M. Bernert, et al. High-density H-mode operation by pellet injection and ELM mitigation with the new active in-vessel saddle coils in ASDEX Upgrade. *Nuclear Fusion*, 52(2):023017, 2012.

[83] Y. Kamada, N. Hosogane, R. Yoshino, T. Hirayama, and T. Tsunematsu. Study of the density limit with pellet fuelling in JT-60. *Nuclear Fusion*, 31(10):1827, 1991.

[84] M.A. Mahdavi, T.H. Osborne, A.W. Leonard, M.S. Chu, et al. High performance h mode plasmas at densities above the greenwald limit. *Nuclear Fusion*, 42(1):52, 2002.

[85] N. Commaux, A. Géraud, B. Pégourié, F. Clairet, et al. Pellet fuelling experiments above the Greenwald density in Tore Supra. *Europhysics Conference Abstracts (Proc. of the 33rd EPS Conference on Controlled Fusion and Plasma Physics, Rome, 2006*, 30I:P–5.105, 2006.

[86] A Gottwald, U Kroth, M Krumrey, M Richter, F Scholze, and G Ulm. The PTB high-accuracy spectral responsivity scale in the VUV and X-ray range. *Metrologia*, 43(2):S125, 2006.

[87] Frank Scholze, Hans Rabus, and Gerhard Ulm. Spectral responsivity of silicon photodiodes: high-accuracy measurement and improved self-calibration in the soft X-ray spectral range. In Oswald H. W. Siegmund and Mark A. Gummin, editors, *EUV, X-Ray, and Gamma-Ray Instrumentation for Astronomy VII*, volume 2808, pages 534–543. SPIE, 1996.